

**UCGE Reports
Number 20259**

Department of Geomatics Engineering

**Alternative Methodologies for the Quality Control of
LiDAR Systems**

(URL: <http://www.geomatics.ucalgary.ca/research/publications/GradTheses.html>)

by

Mohannad M. Al-Durgham

September 2007



UNIVERSITY OF CALGARY

Alternative Methodologies for the Quality Control of LiDAR Systems

by

Mohannad M. Al-Durgham

A THESIS

SUBMITTED TO THE FACULTY OF GRADUATE STUDIES
IN PARTIAL FULFILMENT OF THE REQUIREMENTS FOR THE
DEGREE OF MASTER OF SCIENCE

DEPARTMENT OF GEOMATICS ENGINEERING

CALGARY, ALBERTA

SEPTEMBER, 2007

© Mohannad M. Al-Durgham 2007

Abstract

The ever improving capabilities of GNSS/INS direct geo-referencing technology is having a positive impact on the widespread adoption of LiDAR systems for the acquisition of dense and accurate surface models over extended areas. Unlike with photogrammetric techniques, derived footprints from a LiDAR system are not based on redundant measurements, which are manipulated in an adjustment procedure. Consequently, there are no associated measures (e.g., variance component of unit weight and variance-covariance matrices of the derived parameters) that can be used to evaluate the quality of the final product. In this regard, a LiDAR system is usually viewed as a black box that lacks a well defined set of quality control procedures. This research introduces alternative procedures for evaluating the internal quality of LiDAR data. However, these procedures could be used for external quality control as well. The main premise of the proposed methodologies is that overlapping LiDAR strips will represent the same surface if and only if there are no biases in the derived surfaces. Therefore, the quality of coincidence between overlapping strips will be used as the basis for deriving the quality control measures.

Acknowledgement

This thesis is a result of almost two years of intensive research. However, this accomplishment would not be possible without the support of many people. First and foremost, the support and help I received from my adviser Professor Ayman Habib. I owe to him my advanced knowledge in photogrammetry and LiDAR. I always knocked on his door for advice and found him always willing to help. I never left his office unsatisfied or with questions still in mind. From him I learned how to think at the abstract level, and how to debug problems encountered. His creativeness and wealth of scientific knowledge were an endless source of ideas that highly contributed to my research.

I wish to express my deep appreciation to Dr. Naser El-Sheimy, Dr. Matthew Tait, and Dr. John Yackel for carefully reading and providing comments concerning various aspects of this research.

The author gratefully acknowledges the Technology Institute for Development (LACTEC), Brazil, the University of Federal do Paraná (UFPR), Brazil, and the University of Calgary information technologies department for providing a variety of datasets, which were used in the experimental part of this research. Also, I would like to acknowledge the Integrated Land Management Bureau, British Colombia, Terrapoint, Canada, and the GEOmatics for Informed DEcisions (GEOIDE) for their support of this research work.

Of course, I am also indebted to many colleagues at the Digital Photogrammetry Research Group (DPRG) and beyond. I would like to especially acknowledge Changjae Kim for his priceless advice, Kiin Bang, Ana Paula Kersting, Anna Jarvis, and Jennifer Lay for the help and the fruitful discussions we had together. Last but not least, I would like to thank my friends for their support and endless encouragement. Especially, I would like to acknowledge my best friend and cousin Ahmad Al-Durgham.

To my beloved parents

Mansour & Asma

And to my siblings

Bashar

Basheer

Mohammad

Lamees

&

The future Geomatics Engineer, my brother Khaleel

Table of Contents

Abstract	ii
Acknowledgement	iii
Dedication	iv
Table of Contents	v
List of Tables	vii
List of Figures and Illustrations	ix
List of Symbols, Abbreviations and Nomenclature	xiii
CHAPTER ONE: INTRODUCTION	1
1.1 Problem Definition and Research Objectives	1
1.2 LiDAR Overview	2
1.3 Laser Scanner Data Collection	3
1.4 Mathematical Derivation of Ground Coordinates	5
1.5 Thesis Outline	7
CHAPTER TWO: LITERATURE REVIEW	9
2.1 Introduction	9
2.2 LiDAR Quality Control	9
2.3 Review of Previous Research in LiDAR Quality Control	10
CHAPTER THREE: LIDAR ERROR ANALYSIS	15
3.1 Introduction	15
3.2 Simulation of LiDAR Linear Scanner	16
3.2.1 Linear Scanner & Boresighting Offset Bias	18
3.2.2 Linear Scanner & Boresighting Angular Roll Bias $\Delta\Phi$	21
3.2.3 Linear Scanner & Boresighting Angular Pitch Bias $\Delta\Omega$	25
3.2.4 Linear Scanner & Boresighting Angular Bias $\Delta\kappa$	27
3.2.5 Linear Scanner & Laser Beam Range Bias	29
3.2.6 Linear Scanner & Integrated GNSS/IMU Position Noise	32
3.2.7 Linear Scanner & Integrated GNSS/IMU Attitude Noise	32
3.3 Conclusion	33
CHAPTER FOUR: METHODOLOGY	35
4.1 Introduction	35
4.2 LiDAR Quality Control Using Interpolated Range and Intensity Images	36
4.3 LiDAR Quality Control Using Patches	39
4.3.1 Introduction	39
4.3.2 Segmentation of LiDAR Data	39
4.3.3 Patch Matching Process	40
4.3.4 Point Based Method	41
4.4 LiDAR Quality Control Using Lines	50
4.4.1 Introduction	50
4.4.2 Line Endpoint Method	53
4.4.3 Line Constraint Method (Collinearity Method)	55
4.5 LiDAR Quality Control Using Iterative Closest Patch (ICPatch)	59

4.6 LiDAR Quality Control Using Iterative Closest Point (ICPoint)	62
4.7 Summary	63
CHAPTER FIVE: EXPERIMENTAL RESULTS	64
5.1 Introduction.....	64
5.2 User Interface Overview (LiDAR_QC).....	64
5.3 Sensors and Data Overview	66
5.4 The First Dataset: QC Results	67
5.4.1 Intensity and Range Image Method.....	68
5.4.2 Line (Point Based and Line Constraint) Methods	69
5.4.3 Patch Method.....	71
5.4.4 Iterative Closest Patch Method.....	72
5.4.5 ICPoint Method	74
5.5 The Second Dataset: QC Results	75
5.6 Conclusion	83
CHAPTER SIX: CONCLUSION.....	85
6.1 Conclusion	85
6.2 Recommended Future Work.....	89
REFERENCES	91
APPENDIX A: PARTIAL DERIVATIVES OF THE 3D CONFORMAL EQUATION.....	95
APPENDIX B: DATA FOR INTENSITY AND RANGE IMAGE METHOD.....	97
B.1. A Sample of The Measured Points.....	97
B.2. Points Used for the Range and Intensity Image Method (manually collected)....	100

List of Tables

Table 3-1: Simulated data parameters.....	18
Table 3-2: Summary of the relationships between bias/noise sources and the flying height, flying direction, and look angle.	34
Table 5-1: Summary of the datasets used	67
Table 5-2: The averages and standard deviations of the estimated discrepancies between overlapping strips, using 100 points	68
Table 5-3: Estimated transformation parameters using conjugate linear features in overlapping strips, together with the normal distances between the linear features before and after applying the transformation.	70
Table 5-4: Transformation parameters estimated using conjugate linear features in overlapping strips, together with the normal distances between the linear features before and after applying the transformation.	70
Table 5-5: Transformation parameters estimated using conjugate planar in overlapping strips.....	71
Table 5-6: Transformation parameters estimated using automated matching of conjugate surface elements in strips 3 and 4.....	73
Table 5-7: Transformation parameters estimated using the ICPatch method in three strips.....	74
Table 5-8: Transformation parameters estimated using the ICPoint method, between overlapping strips.....	74
Table 5-9: Estimated transformation parameters between Strip 08803 and Strip 08804 using four methods.....	76
Table 5-10: Estimated transformation parameters between Strip 08804 and Strip 08805.....	77
Table 5-11: Estimated transformation parameters between Strip 08804 and Strip 13030 using four methods.....	77
Table 5-12: Estimated transformation parameters between Strip 08805 and Strip 08806 using four methods.....	78
Table 5-13: Estimated transformation parameters between Strip 08806 and Strip 08807 using two methods.	79

Table 5-14: Estimated transformation parameters between Strip 08806 and Strip 13029 using four methods.....	80
Table 5-15: Estimated transformation parameters between Strip 08807 and Strip 08808 using four methods.....	80
Table 5-16: Estimated transformation parameters between Strip 08807 and Strip 13028 using four methods.....	81
Table 5-17: Estimated transformation parameters between Strip 13027 and Strip 13028 using four methods.....	82
Table 5-18: Estimated transformation parameters between Strip 13029 and Strip 13030 using four methods.....	83
Table 6-1: Qualitative Evaluation of Quality Control methods.....	88

List of Figures and Illustrations

Figure 1.1: Examples of LiDAR system equipment: Leica Geosystems ALS 40 (left), (Leica Geosystems), and OPTECH ALTM 3100 (right), (Optech Inc).....	2
Figure 1.2: Sample LiDAR imagery: range (shaded relief) image (left) and intensity image (right).....	3
Figure 1.3: Zigzag laser scanner footprint, obtained via the deflection of the laser beam using a mirror rotating across the flying direction.	4
Figure 1.4: Elliptical laser scanner footprint, obtained via the deflection of the laser beam using a mirror rotating along and across the flying direction.....	4
Figure 1.5: Reflected signal strength of a LiDAR laser beam.	5
Figure 1.6: Coordinate systems and parameters involved in direct geo-referencing of LIDAR systems.....	6
Figure 3.1: A visual representation of the LiDAR simulation data.	17
Figure 3.2: Effects of boresighting offset bias for a linear scanner	19
Figure 3.3: Surface differences resulting from biases for a single strip (left) and two overlapping strips (right).....	19
Figure 3.4: Bias added to the roll angle: the light blue is the original swath and the dark blue is the biased one (roll angle bias).....	21
Figure 3.5: Isometric and front views of the biased and accurate surfaces (roll angle bias).....	22
Figure 3.6: A front view of two overlapping strips (roll angle bias).	22
Figure 3.7: Differences resulting from biases for a single strip (left) and two overlapping strips (right).....	23
Figure 3.8: The relationship between the range measurement and the x and z components of the point position	24
Figure 3.9: Bias added to the pitch angle: blue denotes the correct laser beam and red is the biased one (pitch angle bias).	25
Figure 3.10: Difference between the true and biased surfaces after adding a pitch angle boresighting bias.	26
Figure 3.11: Bias added to the boresighting yaw angle: the blue swath represents the original footprint and the red swath the biased one (yaw angle bias).....	27

Figure 3.12: Difference between the true and biased surfaces after adding a yaw angle boresighting bias.	28
Figure 3.13: Isometric and front views of the accurate surfaces and the surfaces affected by range bias.	29
Figure 3.14: Differences resulting from the bias for a single strip (left) and two overlapping strips (right).....	30
Figure 3.15: Curvature in the sine and cosine curves	31
Figure 3.16: The effects of noise added to the integrated GNSS/IMU position on the object space	32
Figure 3.17: Error trend resulting from the addition of random (white) noise to the integrated GNSS/IMU attitude.	33
Figure 4.1: Intensity image (left) and range image (right) generated from a LiDAR point cloud	37
Figure 4.2: Manual extraction of conjugate points from overlapping LiDAR strips. The red crosses represent the user defined locations of the conjugate features.....	37
Figure 4.3: Semi-automatic extraction of conjugate points from overlapping LiDAR strips.....	38
Figure 4.4: Two side views of an accumulator array used in the segmentation algorithm.	40
Figure 4.5: LiDAR point cloud before the segmentation (left) and after running the segmentation algorithm (right); different colors indicate different planar patches. .	40
Figure 4.6: Top view of matched patches (left) and a side view (right) showing the co-planarity of the patches.	41
Figure 4.7: Conceptual basis for using planar patches in a point-based approach for the determination of the conformal transformation parameters between two 3D datasets.	42
Figure 4.8: The flow of the least squares solution.	48
Figure 4.9: Physical line extracted from two patches on the same building.....	51
Figure 4.10: Non-physical (virtual) line extracted from two neighbouring patches on two different buildings.	51
Figure 4.11: Non-physical line extracted from two non-neighbouring patches on two different buildings.	52

Figure 4.12: Projecting points within a buffer to define the line endpoints.	52
Figure 4.13: Normal distance in a line pair.....	53
Figure 4.14: Conceptual basis for the use of linear features with the point-based approach for the determination of the conformal transformation parameters between two 3D datasets.....	54
Figure 4.15: Corresponding lines represented by non-conjugate endpoints from two different LiDAR strips.	56
Figure 4.16: Point to patch correspondence using the ICPatch method	60
Figure 4.17: Volume generated by the triangle corners from the first strip and the red point from the second strip	61
Figure 4.18: Non-matched points (red color) and matched points (blue color) with the TIN generated from another strip in the overlapping area.....	62
Figure 4.19: Point to point correspondence using the ICPatch method.....	63
Figure 5.1: Selecting an area (left), then performing the segmentation procedure (right).	65
Figure 5.2: Generating linear features (left) and generating a TIN for an area (right).....	66
Figure 5.3: Intensity images generated from the first dataset with the flying directions shown.	67
Figure 5.4: A sample of conjugate points identified in overlapping strips.	68
Figure 5.5: Histograms for the differences in the X,Y, and Z directions (left to right)....	69
Figure 5.6: Comparison of conjugate linear features before LIDAR system bias removal (left) and after bias removal (right).....	71
Figure 5.7: Locations of selected areas for the registration and automated matching of conjugate surface elements in two overlapping strips.	72
Figure 5.8 A sample of the extracted points in two strips (left); TINs were generated from the second strip point cloud (right).	73
Figure 5.9: Strips 08803 (FD W→E) and 08804 (FD E→W)	76
Figure 5.10: Strips 08804 (FD E→W) and 08805 (FD W→E)	76
Figure 5.11: Strips 08804 (FD E→W) and 13030 (FD E→W)	77
Figure 5.12: Strips 08805 (FD W→E) and 08806 (FD E→W)	78

Figure 5.13: Strips 08806 (FD E→W) and 08807 (FD W→E)	79
Figure 5.14: Strips 08806 (FD E→W) and 13029 (FD W→E)	79
Figure 5.15: Strips 08807 (FD W→E) and 08808 (FD E→W)	80
Figure 5.16: Strips 08807 (FD W→E) and 13028 (FD E→W)	81
Figure 5.17: Strips 13027 (FD W→E) and 13030 (FD E→W)	82
Figure 5.18: Strips 13029 (FD W→E) and 13030 (FD E→W)	83
Figure 6.1: LiDAR point clouds for two buildings before (top) and after (bottom) the adjustment, note that each color indicates a different strip.....	88
Figure 6.2: Measuring point number 9	97
Figure 6.3: Measuring point number 18	97
Figure 6.4: Measuring point number 27	98
Figure 6.5: Measuring point number 79	98
Figure 6.6: Measuring point number 87	99
Figure 6.7: Measuring point number 93	99

List of Symbols, Abbreviations and Nomenclature

Symbol	Definition
3D	Three-Dimensional
DPRG	Digital Photogrammetry Research Group
EQC	External Quality Control
FD	Flying Direction
GIS	Geographic Information System
GNSS	Global Navigation Satellite System
ICPatch	Iterative Closest Patch
ICPoint	Iterative Closest Point
IMU	Inertial Measurement Unit
IQC	Internal Quality Control
LASER	Light Amplification by Stimulated Emission of Radiation
LiDAR	Light Detection And Ranging
LSM	Least Squares Matching
QA	Quality Assurance
QC	Quality Control
TIN	Triangulated Irregular Network

Chapter One: **INTRODUCTION**

1.1 Problem Definition and Research Objectives

LiDAR is known to be a fast and accurate tool for surveying wide areas within a short period of time. It is able to measure millions of points in a single mission. However, during the mission, one cannot force the system to point and shoot at a specific object point. Moreover, LiDAR data lacks the redundancy that can be used in a least squares solution to come up with a measure of the data precision. The only estimate of accuracy that the end users have is the predicted root mean of squares error reported by LiDAR companies (Optech Inc).

LiDAR quality control is an important post-mission process used to verify the quality of the produced data. The objectives of this research are to develop new methods and tools for LiDAR quality control. These methods must not be time consuming, should not require a huge amount of post processing, and must be accurate.

This chapter starts with an overview to LiDAR systems, in which, typically used LiDAR systems (linear and elliptical scanners) are discussed. The second part of this chapter discusses the mathematical model of a LiDAR system used for deriving the target object coordinates.

1.2 LiDAR Overview

LiDAR (Light Detection And Ranging) has been recognized as a fast and accurate active remote sensing system. It has the capability of capturing an enormous number of points over a defined area within a realistic period of time, in comparison to conventional surveying methods. LiDAR has been around for the past thirty-five years, but it has only been widely commercialized in the last nine years (Faruque, 2003).

A LiDAR system consists of three main segments (sensors). The first is a LASER scanner that provides range information from the laser beam firing point to the object point. The second segment is a GNSS sensor that relates the range information to the ground reference frame, and thirdly, an IMU unit supplies the total system with attitude information (Habib, et al., 2007).



Figure 1.1: Examples of LiDAR system equipment: Leica Geosystems ALS 40 (left), (Leica Geosystems), and OPTECH ALTM 3100 (right), (Optech Inc).

The laser scanner is used to obtain raw range measurements from the laser beam firing points to the laser footprint. Measured ranges are then integrated with the GNSS and IMU measurements to relate them to a ground reference frame, leading to the

derivation of the ground coordinates of the laser footprint through a vector summation procedure. Figure 1.1 shows some of the LiDAR systems that are commonly used by the mapping industry.

In addition to range data, modern LiDAR systems can capture intensity images over an area. As a result of advances such as this, LiDAR is being used more extensively in mapping and GIS applications. Figure 1.2 shows a range image (in the form of shaded relief) and an intensity image taken over the same area, illustrating the complementary information obtained from the two types of data.



Figure 1.2: Sample LiDAR imagery: range (shaded relief) image (left) and intensity image (right).

1.3 Laser Scanner Data Collection

The LiDAR laser scanner emits pulses of high frequency and collects the reflections, obtaining a dense cloud of range measurements. These are the raw measurements that are used to derive the ground coordinates. Typically, a laser scanner

creates one of two types of footprints: a zigzag footprint, shown in Figure 1.3 or an elliptical footprint, shown in Figure 1.4.

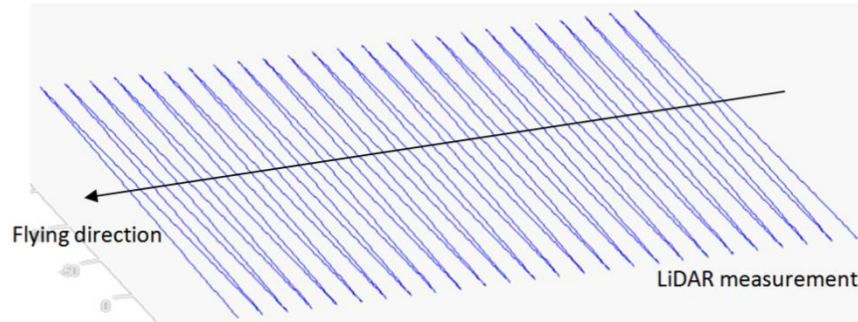


Figure 1.3: Zigzag laser scanner footprint, obtained via the deflection of the laser beam using a mirror rotating across the flying direction.

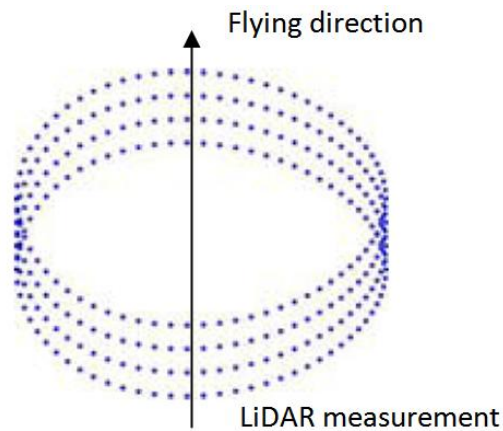


Figure 1.4: Elliptical laser scanner footprint, obtained via the deflection of the laser beam using a mirror rotating along and across the flying direction.

The energy reflected from the laser footprint is converted to a voltage profile, which is known as a waveform. As shown in Figure 1.5, each peak in the waveform received typically corresponds to a different feature or object. The peaks are distinguished from one another by their temporal separation; it can thus be seen that the cloud of red particles in the illustration are closer to the laser scanner than the yellow object. The range to each object is calculated as the signal traveling time multiplied by the speed of light, then divided by two.

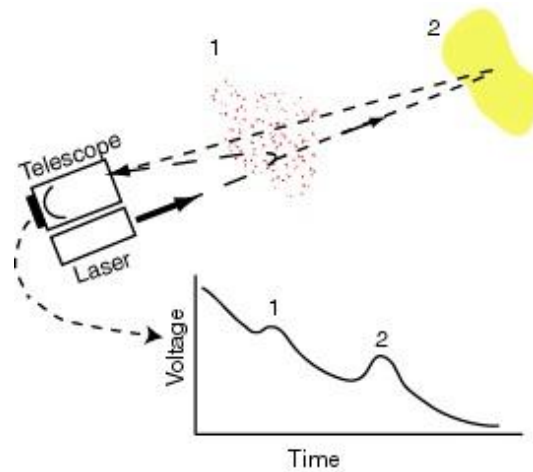


Figure 1.5: Reflected signal strength of a LiDAR laser beam.

The range measurements, together with the pointing direction of the laser scanner and information from the integrated GNSS and IMU units, are used to derive the ground coordinates of the objects in question.

1.4 Mathematical Derivation of Ground Coordinates

Figure 1.6 shows the coordinate systems involved in the LiDAR equation (the ground reference frame, the IMU body frame, the laser unit coordinate system, and the laser beam coordinate system), and shows that the LiDAR equation can be represented as a simple vector summation, as in Equation 1.1 (El-Sheimy, et al., 2005). Many researchers have proposed different forms of equations (involving more or less parameters than Equation 1.1) to be used in deriving the object point. For this research, Equation 1.1 is used to generate the required simulation data discussed in the next chapter.

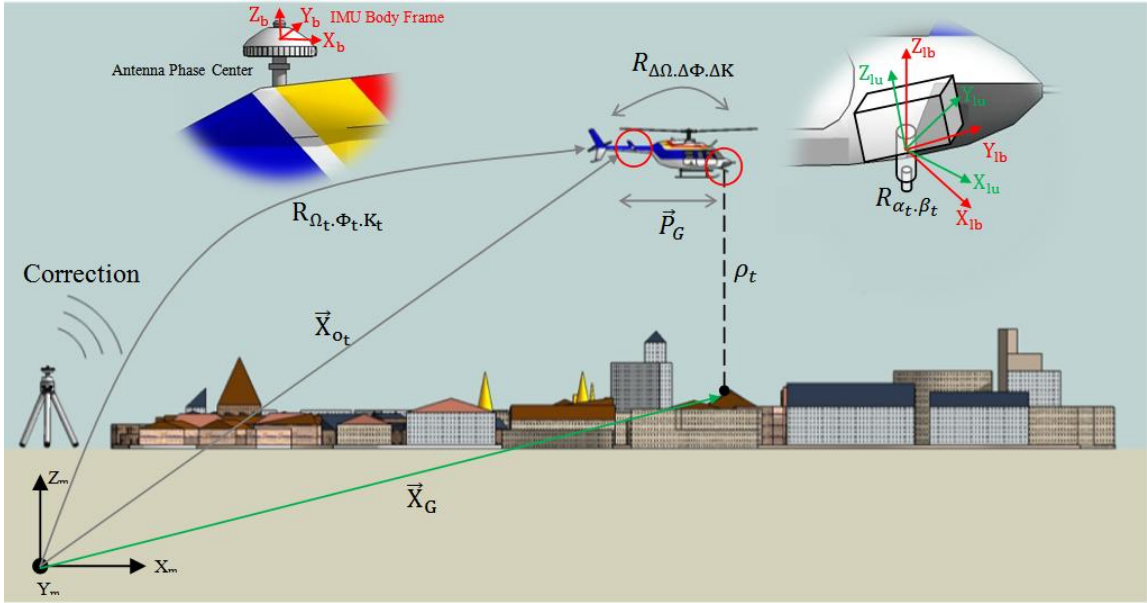


Figure 1.6: Coordinate systems and parameters involved in direct geo-referencing of LIDAR systems.

$$\vec{X}_G = \vec{X}_{o_t} + R_{\Omega_t, \Phi_t, K_t} \times R_{\Delta\Omega, \Delta\Phi, \Delta K} \times \vec{P}_G + R_{\Omega_t, \Phi_t, K_t} \times R_{\Delta\Omega, \Delta\Phi, \Delta K} \times R_{\alpha_t, \beta_t} \times \begin{bmatrix} 0 \\ 0 \\ -\rho_t \end{bmatrix} \quad \mathbf{1.1}$$

Where: (Habib, 2007)

\vec{X}_G = Ground coordinates of the object point under consideration

\vec{X}_{o_t} = Ground coordinates of the GNSS antenna phase center

\vec{P}_G = Spatial boresighting offset between the laser unit and the GNSS antenna phase center, with respect to the laser unit coordinate system

$R_{\Omega_t, \Phi_t, K_t}$ = Rotation matrix that needs to be applied to the IMU coordinate system to make it parallel to the ground coordinate system (Equation 1.2)

$$R_{\Omega_t, \Phi_t, K_t} = R_{\Omega} \times R_{\Phi} \times R_K \quad \mathbf{1.2}$$

$$\begin{bmatrix} R_{1,1} & R_{1,2} & R_{1,3} \\ R_{2,1} & R_{2,2} & R_{2,3} \\ R_{3,1} & R_{3,2} & R_{3,3} \end{bmatrix} = \begin{bmatrix} 1 & 0 & 0 \\ 0 & \cos \Omega & -\sin \Omega \\ 0 & \sin \Omega & \cos \Omega \end{bmatrix} \times \begin{bmatrix} \cos \Phi & 0 & \sin \Phi \\ 0 & 1 & 0 \\ -\sin \Phi & 0 & \cos \Phi \end{bmatrix} \times \begin{bmatrix} \cos K & -\sin K & 0 \\ \sin K & \cos K & 0 \\ 0 & 0 & 1 \end{bmatrix}$$

$R_{\Delta\Omega.\Delta\Phi.\Delta K}$ = Rotation matrix that needs to be applied to the laser unit coordinate system to make it parallel to the IMU coordinate system

$R_{\alpha_t.\beta_t}$ = Rotation matrix that needs to be applied to the laser beam coordinate system to make it parallel to the laser unit coordinate system (Equation 1.3)

$$R_{\alpha,\beta} = R_\alpha \times R_\beta$$

$$R_{\alpha,\beta} = \begin{bmatrix} \cos \alpha & -\sin \alpha & 0 \\ \sin \alpha & \cos \alpha & 0 \\ 0 & 0 & 1 \end{bmatrix} \times \begin{bmatrix} \cos \beta & 0 & \sin \beta \\ 0 & 1 & 0 \\ -\sin \beta & 0 & \cos \beta \end{bmatrix} \quad \mathbf{1.3}$$

ρ_t = Measured range between the laser beam firing point and the target object

It should be noted that the quality of the ground coordinates derived from LiDAR depends on the accuracy of the involved sub-systems (i.e., laser scanner, GNSS, and IMU). The presence of errors such as GNSS/IMU noise, laser beam biases, and boresighting biases (i.e., angular and spatial biases between the system components) will affect the quality of the results, as explained in Chapter Three.

1.5 Thesis Outline

Chapter Two starts with an explanation of what is meant by quality control. Next, a review of the previous contributions made by other researchers is presented. In Chapter Three, the errors associated with LiDAR systems and their analysis are described in detail. The methodologies used to assess the quality of LiDAR systems are discussed in Chapter Four. Also in this chapter, a brief description of an interface developed for LiDAR quality control is proposed. In Chapter Five, the experimental results of the

methodologies described in Chapter Four are discussed. Finally, Chapter Six concludes this research with a summary and discussion.

Chapter Two: **LITERATURE REVIEW**

2.1 Introduction

LiDAR quality control is a challenging procedure due to the challenges met when trying to define a similarity measure for overlapping strips. Many researchers have spent precious time trying to understand LiDAR systems in order to come up with optimized methods for system calibration, quality assurance, and LiDAR strips adjustment. The contributions in those fields are huge; however, there is not enough research towards the quality control of LiDAR systems. Therefore, the main focus of this research is to implement existing methods and develop new ones for the quality control of LiDAR systems. These methods will be also optimized and automated in a program interface developed through this research.

Section 2.2 discusses the conceptual basis of LiDAR quality control. Section 2.3 summarizes several contributions made by researchers during the last decade. Every method has its own pros and cons in terms of accuracy, level of automation, and prerequisites (required pre processing prior the quality control procedures).

2.2 LiDAR Quality Control

The term quality control in LiDAR is defined as “a post-mission procedure applied to ensure/verify the quality of collected data” (Habib, 2007). The quality control can be divided into two main parts: the Internal/relative Quality Control (IQC) and the External/absolute Quality Control (EQC). The term IQC applies when testing for inconsistencies between overlapping LiDAR strips without having true knowledge about

their relationship with the ground reference frame. EQC is used when comparing different strips with regard to the ground reference frame (e.g. using ground control points, or patches of points with known coordinates relative to the ground reference frame). Quality control is an extremely important stage; it helps to assess the quality of the available data.

Most of the current LiDAR quality control methods focus on the IQC rather than the EQC, due to the fact that it is still expensive and time-consuming to establish control points or surfaces. However, many of the IQC methods could be used for performing the EQC.

2.3 Review of Previous Research in LiDAR Quality Control

As mentioned early in this chapter, there is not enough research towards the quality control of LiDAR systems. Therefore, the main focus of this research is to implement existing methods and develop new ones for the quality control of LiDAR systems. It has been noticed that current research topics focus on the adjustment of LiDAR strips rather than detecting biases. The following paragraphs summarize strip adjustment methods suggested by other researchers.

In the last decade, several quality control procedures were proposed. These procedures vary in terms of complexity, accuracy, and time consumption. In this section, the focus will be on the internal quality control methods. In other words, the methods that

use the output of LiDAR systems (clouds of points) in the assessment of the data quality will be discussed. These methods are discussed briefly in the following paragraphs.

Pfeifer et al. (2005) suggested a correction polynomial to reduce the discrepancies between overlapping strips. This polynomial is meant to correct shift, range, and rotating mirror errors. The polynomial is a function of time; in other words, the polynomial parameters can change over time to enhance the modeling of errors in different locations. The simplest version of this polynomial is obtained when considering the polynomial parameters to be constant in the time domain.

Another IQC method, based on a least squares adjustment procedure, was proposed by Maas (2000). This method uses a set of points from the first strip and generates a Triangulated Irregular Network (TIN) from the second strip. Then the least squares design matrix is constructed based on the point to patch normal distances. In this method, Least Squares Matching (LSM) is used to find the conjugate patches for artificial points derived from the generated TIN.

Vosselman, et al. (2001) discussed the strip adjustment of LiDAR data using control and tie points. They suggested a nine-parameter mathematical model to be used when adjusting LiDAR strips. Tie points were extracted from the overlap area between LiDAR strips. Since a point to point correspondence is not available between LiDAR strips, the points had to be interpolated in order to achieve a match. In this method, field surveying is required to obtain ground control points. Therefore, this method is not

applicable in cases in which access to the study area is limited or prohibited. This is the case with many of the current EQC methods.

A method using photogrammetrically generated Digital Surface Models (DSM) was proposed by Bretar et al. (2004). The concept here is to match LiDAR strips individually with a reference DSM generated using photogrammetric techniques. In this case, the adjusted LiDAR strips are consistent with the photogrammetric reference frame, which is a benefit for any further applications (e.g. 3D modeling, true orthophoto generation, virtual reality modeling). However, this method requires the availability of aerial photos or a previously generated DSM covering the study area, or a portion of it, which is not usually the case. Furthermore, errors coming from the photogrammetric process will be inherited in the LiDAR strip adjustment. The same benefits can be obtained using the current photogrammetric and LiDAR data integration techniques. Please refer to Ghanma, 2006 for further details.

Kornus et al. (2003) suggested a block adjustment method that removes the major errors in the vertical direction. The assumption here is that LiDAR strips are affected by biases that act only in the vertical direction. Recent research proved that the amount of error in the vertical direction is smaller when compared to the error in the horizontal direction (Chapter Five). Horizontal shifts can mistakenly appear to be vertical biases, especially when interpolating different strips onto grids and generating difference images (subtracting the images from one another). This phenomenon can be seen clearly at break lines (e.g. building edges)

Rönnholm (2004) introduced a method of adjusting LiDAR strips using images covering the dataset area, and using human judgment to identify conjugate features between the images and the LiDAR strips. The adjustment process is then run simultaneously on all strips while measuring the conjugate features, until the estimated transformation parameters are no longer changing. Rönnholm argues that the human interference is an advantage, since the human has a greater ability to make judgments about features, even if the features are not perfectly clear. However, this method is not practical for LiDAR quality control. The process of quality control is expected to be fast and accurate. Moreover, due to the huge amount of data (LiDAR data) that comes out of a single mission, the process of quality control should be planned carefully, with the highest degree of optimization.

Morin, 2003 researched the calibration of a LiDAR system, by developing and implementing a new calibration method for airborne laser scanner. In his research, potential error sources associated with various LiDAR systems were addressed. A rigorous stochastic model was provided and the need for control points in the calibration process was eliminated. However, the process of LiDAR calibration is still manual and time consuming. Moreover, the suggested method requires multiple LiDAR coverage with different flying configuration that does not usually exist in the normal process of data acquisition. Usually, LiDAR data is collected in the same manner photogrammetric data is measured (overlapping strips with opposite flying directions).

Lee et al. (2005) proposed a method based on the extraction of conjugate linear features from overlapping LiDAR strips. The method starts with an area that consists of some man-made features, and runs a clustering process in order to obtain planar patches. The patches are then intersected to get linear features of infinite length, which are later truncated using information from previously extracted patches. If the overlapping strips have no biases, the conjugate features should overlap nicely. However, when biases exist, these conjugate lines will be shifted with respect to one another in a certain direction. This is a very good method when the area covered by LiDAR is rich with intersecting patches (buildings' roofs). However, in areas that have no man-made features, it would be hard to extract the required primitives (linear features) for this method. Additionally, the automation level in this method is something that should be taken into consideration when developing algorithms for extracting linear features.

Through this literature review, it has been discovered that there are no standardized procedures suggested for the quality control of LiDAR data. Moreover, the main concern of previous research is adjusting LiDAR strips, not detecting biases. Also, the automation and the optimization levels of the methods are not discussed, although it is believed that the data preparation takes the largest portion of time in the whole quality control procedure. The goal of this research is to develop and implement quality control methods/procedures that could be usable by both the data provider and the end user.

Chapter Three: LIDAR ERROR ANALYSIS

3.1 Introduction

In this chapter, we will be investigating the effects of biases and random noise in the system parameters and measurements on the quality of LiDAR output. As mentioned before, LiDAR consists of three main sensors positioned onboard the aeroplane. The GNSS unit provides position information, while the IMU unit gives attitude information. Due to the low frequency of the GNSS measurements, the IMU is used to fill in the gaps (give position information) in the GNSS data. On the other hand, the GNSS unit is used to model the drifts in the IMU derived position. Finally, the laser unit is used to obtain measurements of the object space, to feed the total system with range information.

The effects of biases in the system boresighting parameters that are determined from a calibration procedure will be scrutinized here. In addition, the effects on the LiDAR output of noise in the system measurements from the integrated GNSS/IMU units will be investigated. In Equation 1.1, noise will be added to the vector \vec{X}_{o_t} and to the rotation matrix $R_{\Omega_t, \Phi_t, K_t}$. In this rotation matrix, noise will be added to the components Ω_t, Φ_t, K_t separately to study the effects for each component of the rotation matrix. Biases will be added to the vector \vec{P}_G , which represents the offset between the laser unit and the GNSS antenna phase center, with respect to the laser unit coordinate system. In addition, biases will be added to the $R_{\Delta\Omega, \Delta\Phi, \Delta K}$ matrix in order to investigate the

significance of the calibration procedure on the accuracy of the derived object space.

Finally, biases will be added to the range measurement ρ_t .

A wide range of experiments could be carried out. For instance, one might investigate the effects of biases on R_{α_t, β_t} (the rotation matrix that needs to be applied to the laser unit coordinate system to make it parallel to the laser beam coordinate system), or apply a scale error to the measured range ρ_t . Our target here is to investigate the influences of what are believed to be the major sources of biases in LiDAR. Although the laser beam angles (α_t, β_t) are also considered as potential sources of errors, they will not be discussed, due to their strong correlations with the pitch and roll angles, respectively.

3.2 Simulation of LiDAR Linear Scanner

In order to carry out the aforementioned tests and to study precisely the effects of biases and noise, these tests must be held in a controlled environment. Therefore, a program has been designed to perform a simple simulation of LiDAR linear scanner data. This simulation starts with an artificially generated surface and trajectory. Then, LiDAR measurements and parameters are computed. After that, biases/noise are added to system parameters/measurements. Finally, the surface is reconstructed and compared with the original surface. The blue zigzag in Figure 3.1 is a visual representation of the simulated data.

The trajectory of the aeroplane is set to be along the Y-axis, and the swath angle of the laser beam is assumed to be ± 20 degrees. Five thousand points are generated in two hundred lines (swaths), and the laser beam starts from an angle of negative twenty degrees with respect to the nadir, and finishes with an angle of twenty degrees. The aeroplane travels at a speed of one hundred meters per second and an acceleration of zero. The attitude is set to zero for all rotation angles.

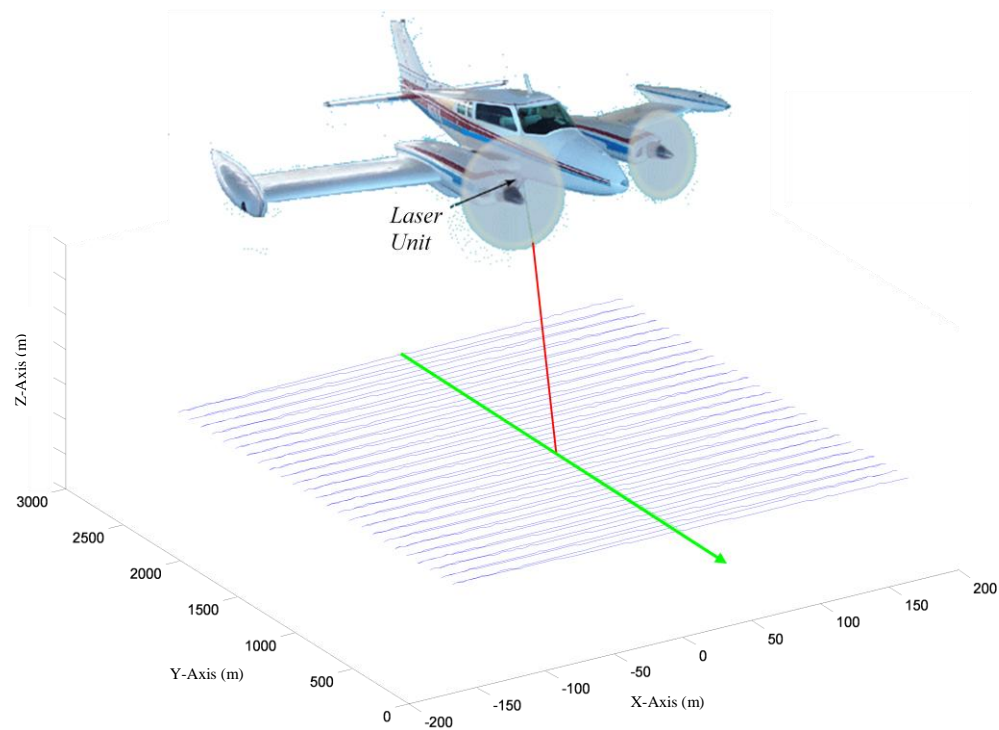


Figure 3.1: A visual representation of the LiDAR simulation data.

In the simulations, the ground is assumed to be flat, horizontal terrain in order to eliminate any terrain-related patterns in the generated figures. The flying height is set to five hundred meters above the ellipsoid (four hundred and fifty meters above the ground).

Another case that will be discussed is the generation of overlapping strips consisting of strips flown in opposite directions. An overlap of thirty percent of the strip width is assumed, a summary of this simulation configuration could be found in Table 3-1. The objective was to study the behaviour of biases when flying in different directions, at different heights, and with different overlap ratios. Although other simulations were run under different configurations (e.g. different flying heights and different overlap amounts), we will discuss only the tests done using the configuration described above, due to similarity in the results. The following section elaborates on the noises and biases added and the analysis of their effects.

Table 3-1: Simulated data parameters

Parameter	Value
Terrain Slope	Flat Horizontal Terrain
Flying Height Above Ground	450 meters, 850 meters
Scanning Angle	± 20
Flying Direction	South-North, North-South
Flying Speed	100 meters per second
Scanner Type	Linear Scanner
Overlap Percentage	30%
Number of Samples in one Line (Forward and Backward)	200
Total Number of Samples	5000 per strip
Strip Width	~225 meters, ~620 meters

3.2.1 Linear Scanner & Boresighting Offset Bias

Shifts of ten, twenty, and thirty centimetres were added to the X,Y,Z components, respectively, of the boresighting vector \vec{P}_G , and, as expected, the effects of this bias are

constant shifts in the object space. The blue zigzag in Figure 3.2 represents the ground truth and the pink one is the ground derived after adding the shifts.

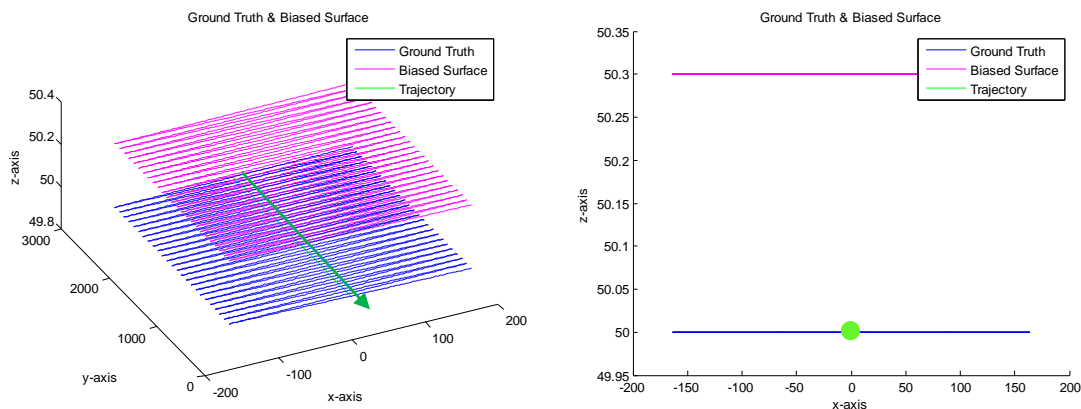


Figure 3.2: Effects of boresighting offset bias for a linear scanner

Note that in the above figure, we are able to visualize biases in the Z direction only. A better visualization of the errors could be accomplished by subtracting the true surface from the biased surface (Figure 3.3). Note that the biases in the planimetric directions are dependent on the flying direction, while the bias in the Z direction is not.

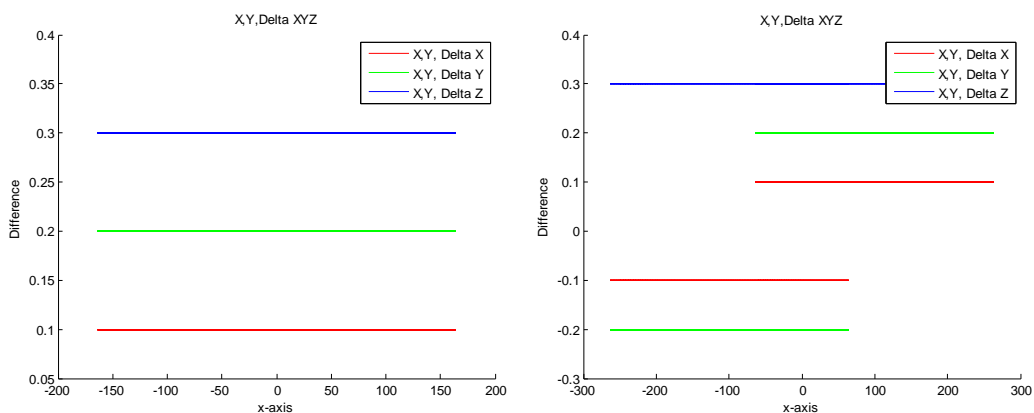


Figure 3.3: Surface differences resulting from biases for a single strip (left) and two overlapping strips (right).

Another way to study the effects of biases is by deriving their impacts using the LiDAR equation. This is accomplished by deriving LiDAR equation with respect to the parameter containing the desired bias. Equations 3.1 to 3.5 represent the steps done to derive the effects of the boresighting offset bias. For simplification purposes, the boresighting shift and orientation parameters are set to zero. Therefore, the matrix $R_{\Delta\Omega,\Delta\Phi,\Delta K}$ will always be identity. Also, the attitude angles are set to zero for the same reason.

$$\vec{X}_G = \vec{X}_{o_t} + \underbrace{R_{\Omega_t,\Phi_t,K_t} \times R_{\Delta\Omega,\Delta\Phi,\Delta K}}_R \times \vec{P}_G + \underbrace{R_{\Omega_t,\Phi_t,K_t} \times R_{\Delta\Omega,\Delta\Phi,\Delta K}}_R \times R_{\alpha_t,\beta_t} \times \begin{bmatrix} 0 \\ 0 \\ -\rho_t \end{bmatrix} \quad 3.1$$

$$\vec{X}_G = \vec{X}_{o_t} + R \times \begin{bmatrix} \Delta X_G \\ \Delta Y_G \\ \Delta Z_G \end{bmatrix} + R \times R_{\alpha_t,\beta_t} \times \begin{bmatrix} 0 \\ 0 \\ -\rho_t \end{bmatrix} \quad 3.2$$

$$\frac{\partial \vec{X}_G}{\partial \Delta X_G} = \begin{bmatrix} R_{1,1} & R_{1,2} & R_{1,3} \\ R_{2,1} & R_{2,2} & R_{2,3} \\ R_{3,1} & R_{3,2} & R_{3,3} \end{bmatrix} \times \begin{bmatrix} 1 \\ 0 \\ 0 \end{bmatrix} = \begin{bmatrix} R_{1,1} \\ R_{2,1} \\ R_{3,1} \end{bmatrix}, \partial \vec{X}_G = \begin{bmatrix} \partial \Delta X_G \\ 0 \\ 0 \end{bmatrix} \quad 3.3$$

$$\frac{\partial \vec{X}_G}{\partial \Delta Y_G} = \begin{bmatrix} R_{1,1} & R_{1,2} & R_{1,3} \\ R_{2,1} & R_{2,2} & R_{2,3} \\ R_{3,1} & R_{3,2} & R_{3,3} \end{bmatrix} \times \begin{bmatrix} 0 \\ 1 \\ 0 \end{bmatrix} = \begin{bmatrix} R_{1,2} \\ R_{2,2} \\ R_{3,2} \end{bmatrix}, \partial \vec{X}_G = \begin{bmatrix} 0 \\ \partial \Delta Y_G \\ 0 \end{bmatrix} \quad 3.4$$

$$\frac{\partial \vec{X}_G}{\partial \Delta Z_G} = \begin{bmatrix} R_{1,1} & R_{1,2} & R_{1,3} \\ R_{2,1} & R_{2,2} & R_{2,3} \\ R_{3,1} & R_{3,2} & R_{3,3} \end{bmatrix} \times \begin{bmatrix} 0 \\ 0 \\ 1 \end{bmatrix} = \begin{bmatrix} R_{1,3} \\ R_{2,3} \\ R_{3,3} \end{bmatrix}, \partial \vec{X}_G = \begin{bmatrix} 0 \\ 0 \\ \partial \Delta Z_G \end{bmatrix} \quad 3.5$$

It can be seen clearly now that the derived errors (Equations 3.3 to 3.5) have the same magnitude and direction as the added errors. This indicates that such a bias will be independent of the flying height and the look angle, but will be dependent on the flying

direction because of the contribution of the rotation matrix. As mentioned before, the attitude information is set to zero, but when flying in the opposite direction, the yaw angle is set to 180 degrees.

3.2.2 Linear Scanner & Boresighting Angular Roll Bias $\Delta\Phi$

In this test, a sixty second bias was added to the boresighting roll angle $\Delta\phi$ (Figure 3.4). Since we are dealing with a linear scanner and a bias acting across the flying direction (the flying direction is along the Y axis), the major bias is expected to be in the X direction.

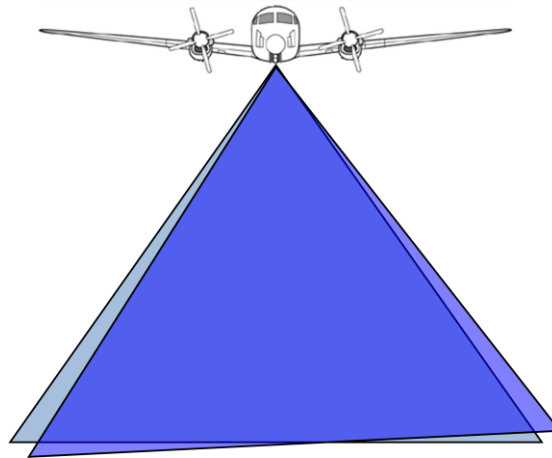


Figure 3.4: Bias added to the roll angle: the light blue is the original swath and the dark blue is the biased one (roll angle bias).

The following figure shows the simulated ground object after adding the desired bias. It is clear that errors in the vertical direction are experienced. Figure 3.6 shows two strips (flown in opposite directions) generated after adding the same bias in both strips. Note that the direction of the biased surface changes between strips.

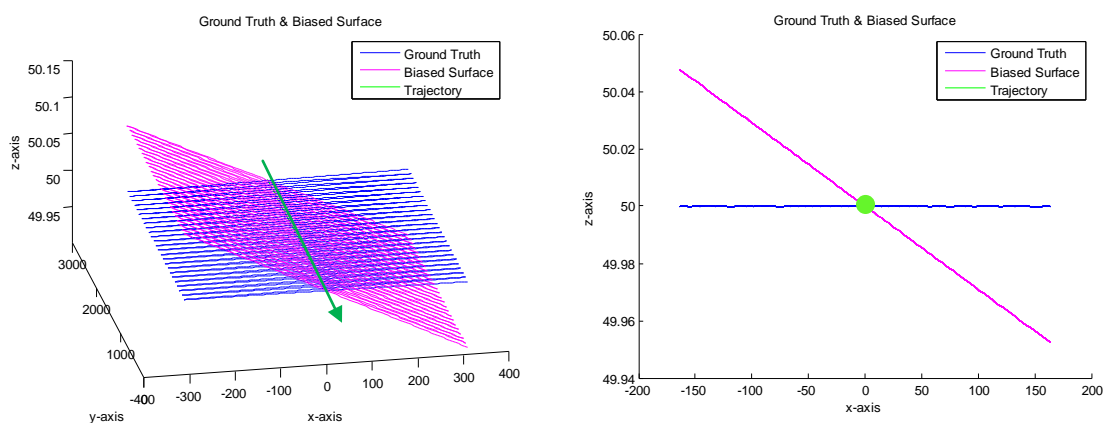


Figure 3.5: Isometric and front views of the biased and accurate surfaces (roll angle bias).

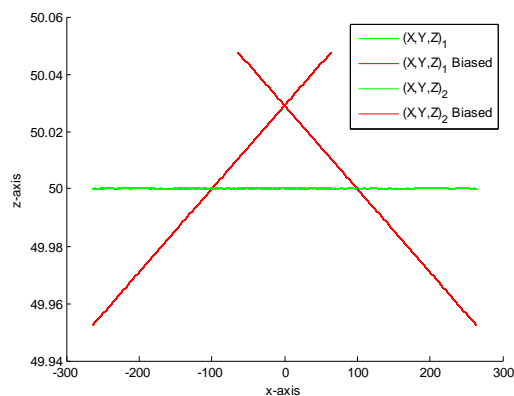


Figure 3.6: A front view of two overlapping strips (roll angle bias).

The effects of a bias in the roll angle can be seen clearly in the difference figures below (Figure 3.7). In the left figure, we notice that the major errors appear in the across flight direction, as expected. The Z direction experienced different magnitudes of error depending on the look angle of the laser beam (error is maximum when the beam is at the edges, and minimum at the nadir point).

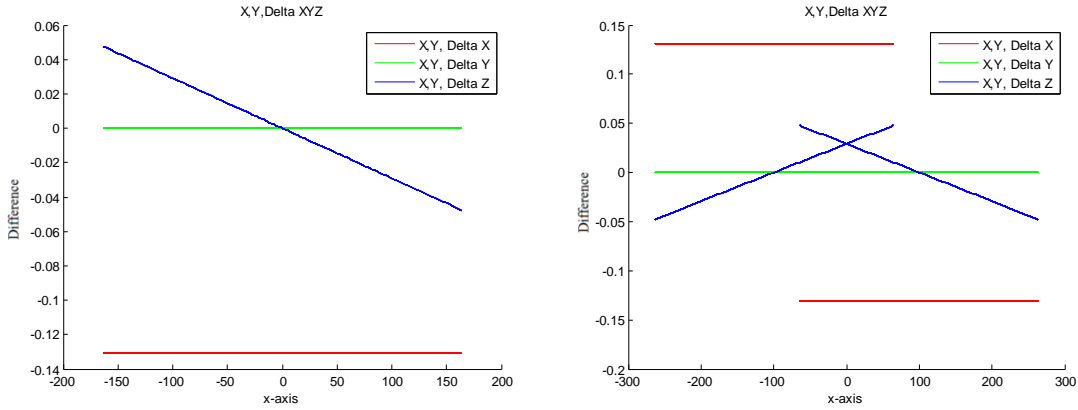


Figure 3.7: Differences resulting from biases for a single strip (left) and two overlapping strips (right).

It is obvious that in the case of this bias, the behavior of the errors is dependent on the flying direction. Note how the errors in the across flight and Z directions changes between strips. This indicates that it is possible to detect such a bias whenever we have overlapping strips in opposite directions (only bias in the Z direction could be detected when flying in similar directions). To verify these conclusions, one can derive the errors caused by the roll angle, as shown in Equations 3.6 to 3.11.

Assuming that the angle $\Delta\Phi$ is very small, therefore $\sin \Delta\Phi = \Delta\Phi$, and $\cos \Delta\Phi = 1$.

$$\vec{X}_G = \vec{X}_{o_t} + R_{\Omega_t, \Phi_t, K_t} \times R_{\Delta\Omega, \Delta\Phi, \Delta K} \times \vec{P}_G + R_{\Omega_t, \Phi_t, K_t} \times R_{\Delta\Omega, \Delta\Phi, \Delta K} \times R_{\alpha_t, \beta_t} \times \begin{bmatrix} 0 \\ 0 \\ -\rho_t \end{bmatrix} \quad 3.6$$

$$\vec{X}_G = \vec{X}_{o_t} + R_{\Omega_t, \Phi_t, K_t} \times \begin{bmatrix} 1 & 0 & \Delta\Phi \\ 0 & 1 & 0 \\ -\Delta\Phi & 0 & 1 \end{bmatrix} \times \vec{P}_G + R_{\Omega_t, \Phi_t, K_t} \times \begin{bmatrix} 1 & 0 & \Delta\Phi \\ 0 & 1 & 0 \\ -\Delta\Phi & 0 & 1 \end{bmatrix} \times R_{\alpha_t, \beta_t} \times \begin{bmatrix} 0 \\ 0 \\ -\rho_t \end{bmatrix} \quad 3.7$$

$$\frac{\partial \vec{X}_G}{\partial \Delta\Phi} = R_{\Omega_t, \Phi_t, K_t} \times \begin{bmatrix} 0 & 0 & 1 \\ 0 & 0 & 0 \\ -1 & 0 & 0 \end{bmatrix} \times \vec{P}_G + R_{\Omega_t, \Phi_t, K_t} \times \begin{bmatrix} 0 & 0 & 1 \\ 0 & 0 & 0 \\ -1 & 0 & 0 \end{bmatrix} \times R_{\alpha_t, \beta_t} \times \begin{bmatrix} 0 \\ 0 \\ -\rho_t \end{bmatrix} \quad 3.8$$

$$\frac{\partial \vec{X}_G}{\partial \Delta\Phi} = R_{\Omega_t \cdot \Phi_t \cdot K_t} \times \begin{bmatrix} \Delta Z_G \\ 0 \\ -\Delta X_G \end{bmatrix} + R_{\Omega_t \cdot \Phi_t \cdot K_t} \times \begin{bmatrix} -\rho_t \cos \beta \\ 0 \\ -\rho_t \cos \alpha \sin \beta \end{bmatrix} \quad 3.9$$

$$\frac{\partial \vec{X}_G}{\partial \Delta\Phi} = \begin{bmatrix} -R_{1,3} \Delta X_G + R_{1,1} \Delta Z_G - \rho_t [R_{1,3} \cos \alpha \sin \beta + R_{1,1} \cos \beta] \\ -R_{2,3} \Delta X_G + R_{2,1} \Delta Z_G - \rho_t [R_{2,3} \cos \alpha \sin \beta + R_{2,1} \cos \beta] \\ -R_{3,3} \Delta X_G + R_{3,1} \Delta Z_G - \rho_t [R_{3,3} \cos \alpha \sin \beta + R_{3,1} \cos \beta] \end{bmatrix} \quad 3.10$$

Assuming $R = I$, and $P_G = 0$ yeilds,

$$\partial \vec{X}_G = \begin{bmatrix} -\rho \cos \beta \times \partial \Delta\Phi \\ 0 \\ -\rho \sin \beta \times \partial \Delta\Phi \end{bmatrix} = \begin{bmatrix} -z \times \partial \Delta\Phi \\ 0 \\ -x \times \partial \Delta\Phi \end{bmatrix} \quad 3.11$$

Note that in Equation 3.11, the term $\rho \cos \beta$ is nothing but the flying height ‘z’ above the ground (simulated surface), which will always be constant. However, the term $\rho \sin \beta$ is the x position of the measured point, which changes depending on the look angle β (Figure 3.8). Therefore, the height is expected to be constant over the whole strip, and the variation in x is dependent on the look angle (Figure 3.7). This x component is also dependent on the flying height, due to the range component. Generally speaking, the effect of a bias added to the roll angle is dependent on the look angle, the flying height, and the flying direction.

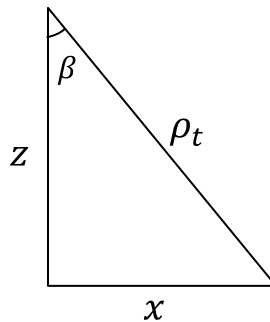


Figure 3.8: The relationship between the range measurement and the x and z components of the point position

3.2.3 Linear Scanner & Boresighting Angular Pitch Bias $\Delta\Omega$

In this subsection, a bias of 60 seconds is added to the pitch angle. Figure 3.9 illustrates the added bias. The linear scanner is assumed to be looking down (blue ray), as shown in this side view. The bias makes look forward or backward, depending on the sign of the bias (red ray).

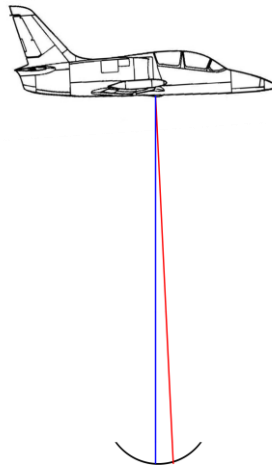


Figure 3.9: Bias added to the pitch angle: blue denotes the correct laser beam and red is the biased one (pitch angle bias).

Figure 3.10 is used to visualize the difference between the true and biased surfaces. The effect of this bias acts mainly along the flying direction. The resulting differences in the across flight and Z directions were zero, causing the X curve to overlap with the Z curve. This is not the case when dealing with an elliptical scanner, for which more error is expected to act across the flying direction.

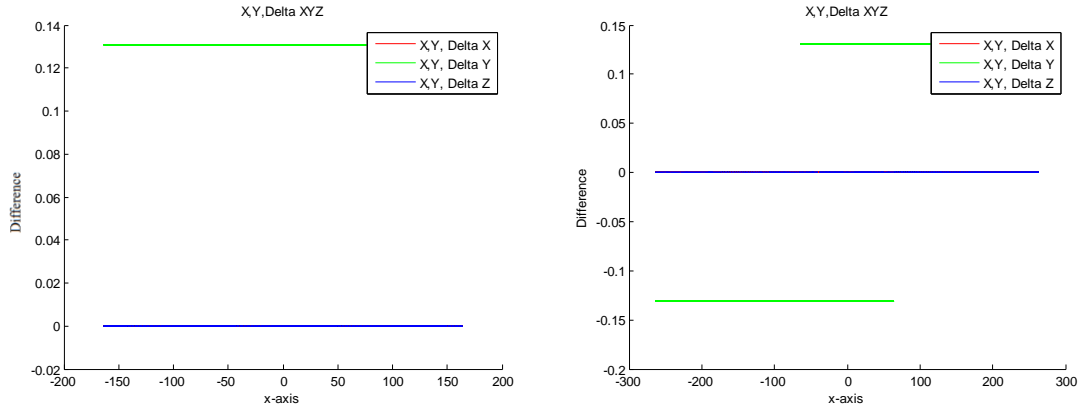


Figure 3.10: Difference between the true and biased surfaces after adding a pitch angle boresighting bias.

Similarly to what has been done in the previous subsections, the results shown in Figure 3.10 are verified by mathematically deriving the errors resulting from the pitch angle bias. Equations 3.12 through 3.17 show the flow of the derivation. Similar assumptions to the ones made in the previous section will be used here.

$$\vec{X}_G = \vec{X}_{o_t} + R_{\Omega_t, \Phi_t, K_t} \times R_{\Delta\Omega, \Delta\Phi, \Delta K} \times \vec{P}_G + R_{\Omega_t, \Phi_t, K_t} \times R_{\Delta\Omega, \Delta\Phi, \Delta K} \times R_{\alpha_t, \beta_t} \times \begin{bmatrix} 0 \\ 0 \\ -\rho_t \end{bmatrix} \quad 3.12$$

$$\vec{X}_G = \vec{X}_{o_t} + R_{\Omega_t, \Phi_t, K_t} \times \begin{bmatrix} 1 & 0 & 0 \\ 0 & 1 & -\Delta\Omega \\ 0 & \Delta\Omega & 1 \end{bmatrix} \times \vec{P}_G + R_{\Omega_t, \Phi_t, K_t} \times \begin{bmatrix} 1 & 0 & 0 \\ 0 & 1 & -\Delta\Omega \\ 0 & \Delta\Omega & 1 \end{bmatrix} \times R_{\alpha_t, \beta_t} \times \begin{bmatrix} 0 \\ 0 \\ -\rho_t \end{bmatrix} \quad 3.13$$

$$\frac{\partial \vec{X}_G}{\partial \Delta\Omega} = R_{\Omega_t, \Phi_t, K_t} \times \begin{bmatrix} 0 & 0 & 0 \\ 0 & 0 & -1 \\ 0 & 1 & 0 \end{bmatrix} \times \vec{P}_G + R_{\Omega_t, \Phi_t, K_t} \times \begin{bmatrix} 0 & 0 & 0 \\ 0 & 0 & -1 \\ 0 & 1 & 0 \end{bmatrix} \times R_{\alpha_t, \beta_t} \times \begin{bmatrix} 0 \\ 0 \\ -\rho_t \end{bmatrix} \quad 3.14$$

$$\frac{\partial \vec{X}_G}{\partial \Delta\Omega} = R_{\Omega_t, \Phi_t, K_t} \times \begin{bmatrix} 0 \\ -\Delta Z_G \\ \Delta Y_G \end{bmatrix} \times \vec{P}_G + R_{\Omega_t, \Phi_t, K_t} \times \begin{bmatrix} 0 \\ \rho_t \cos \beta \\ \rho_t \sin \alpha \sin \beta \end{bmatrix} \quad 3.15$$

$$\frac{\partial \vec{X}_G}{\partial \Delta\Omega} = \begin{bmatrix} R_{1,3}\Delta Y_G - R_{1,2}\Delta Z_G + \rho_t [R_{1,3} \sin \alpha \sin \beta + R_{1,2} \cos \beta] \\ R_{2,3}\Delta Y_G - R_{2,2}\Delta Z_G + \rho_t [R_{2,3} \sin \alpha \sin \beta + R_{2,2} \cos \beta] \\ R_{3,3}\Delta Y_G - R_{3,2}\Delta Z_G + \rho_t [R_{3,3} \sin \alpha \sin \beta + R_{3,2} \cos \beta] \end{bmatrix} \quad 3.16$$

$$\partial \vec{X}_G = \begin{bmatrix} 0 \\ \rho \cos \beta \times \partial \Delta \Omega \\ 0 \end{bmatrix} \quad 3.17$$

Equation 3.17 proves that this bias has no effect on either the across flight or the Z positions, and that there is a constant bias along the flying direction ($\rho \cos \beta = z$), which is consistent with the results shown in Figure 3.10. Finally, we conclude that biases added to the pitch angle affect the ‘along flight’ direction only. Moreover, these effects are independent of the laser scanner look angle, but dependent on the flying height and direction.

3.2.4 Linear Scanner & Boresighting Angular Bias $\Delta \kappa$

For this test, 60 seconds are added to the Yaw angle $\Delta \kappa$, and Figure 3.11 indicates that the effects of this bias are along the flying direction. Figure 3.12 visualizes the resulting difference between the true and biased surfaces. In the right part of the figure, it is seen that this bias is independent of the flying direction (differences for both strips are identical, regardless of the flying direction). This bias is still detectable in overlapping strips due to the differences between the overlapping areas; however, one cannot detect this bias when comparing strips with 100% overlap.

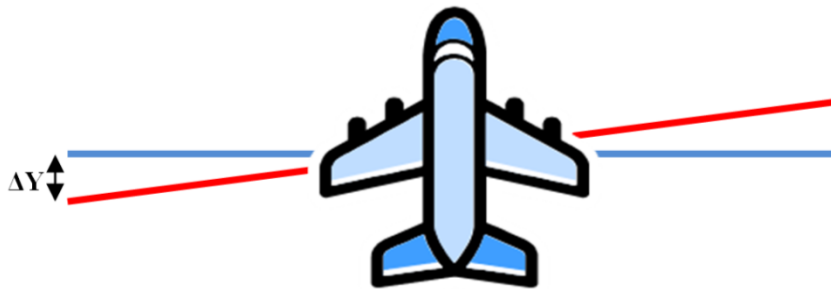


Figure 3.11: Bias added to the boresighting yaw angle: the blue swath represents the original footprint and the red swath the biased one (yaw angle bias).

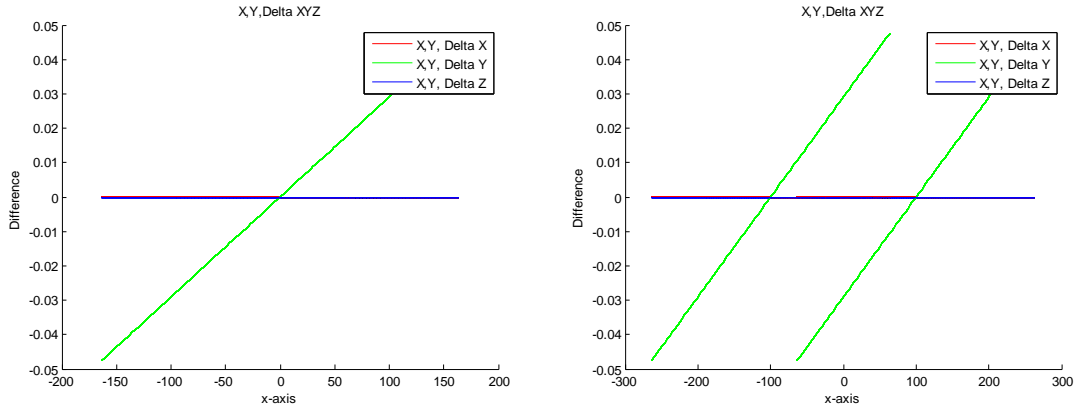


Figure 3.12: Difference between the true and biased surfaces after adding a yaw angle boresighting bias.

Similar to the previous sections, Equations 3.18 to 3.23 shows the mathematical derivation of Yaw angle error in LiDAR equation.

$$\vec{X}_G = \vec{X}_{o_t} + R_{\Omega_t, \Phi_t, K_t} \times R_{\Delta\Omega, \Delta\Phi, \Delta K} \times \vec{P}_G + R_{\Omega_t, \Phi_t, K_t} \times R_{\Delta\Omega, \Delta\Phi, \Delta K} \times R_{\alpha_t, \beta_t} \times \begin{bmatrix} 0 \\ 0 \\ -\rho_t \end{bmatrix} \quad 3.18$$

$$\vec{X}_G = \vec{X}_{o_t} + R_{\Omega_t, \Phi_t, K_t} \times \begin{bmatrix} 1 & -\Delta K & 0 \\ \Delta K & 1 & 0 \\ 0 & 0 & 1 \end{bmatrix} \times \vec{P}_G + R_{\Omega_t, \Phi_t, K_t} \times \begin{bmatrix} 1 & -\Delta K & 0 \\ \Delta K & 1 & 0 \\ 0 & 0 & 1 \end{bmatrix} \times R_{\alpha_t, \beta_t} \times \begin{bmatrix} 0 \\ 0 \\ -\rho_t \end{bmatrix} \quad 3.19$$

$$\frac{\partial \vec{X}_G}{\partial \Delta K} = R_{\Omega_t, \Phi_t, K_t} \times \begin{bmatrix} 0 & -1 & 0 \\ 1 & 0 & 0 \\ 0 & 0 & 0 \end{bmatrix} \times \vec{P}_G + R_{\Omega_t, \Phi_t, K_t} \times \begin{bmatrix} 0 & -1 & 0 \\ 1 & 0 & 0 \\ 0 & 0 & 0 \end{bmatrix} \times R_{\alpha_t, \beta_t} \times \begin{bmatrix} 0 \\ 0 \\ -\rho_t \end{bmatrix} \quad 3.20$$

$$\frac{\partial \vec{X}_G}{\partial \Delta K} = R_{\Omega_t, \Phi_t, K_t} \times \begin{bmatrix} -\Delta Y_G \\ \Delta X_G \\ 0 \end{bmatrix} + R_{\Omega_t, \Phi_t, K_t} \times \begin{bmatrix} -\rho_t \sin \alpha \sin \beta \\ \rho_t \cos \alpha \sin \beta \\ 0 \end{bmatrix} \quad 3.21$$

$$\frac{\partial \vec{X}_G}{\partial \Delta K} = \begin{bmatrix} R_{1,2} \Delta X_G - R_{1,1} \Delta Y_G + \rho [R_{1,2} \cos \alpha \sin \beta - R_{1,1} \sin \alpha \sin \beta] \\ R_{2,2} \Delta X_G - R_{2,1} \Delta Y_G + \rho [R_{2,2} \cos \alpha \sin \beta - R_{2,1} \sin \alpha \sin \beta] \\ R_{3,2} \Delta X_G - R_{3,1} \Delta Y_G + \rho [R_{3,2} \cos \alpha \sin \beta - R_{3,1} \sin \alpha \sin \beta] \end{bmatrix} \quad 3.22$$

$$\frac{\partial \vec{X}_G}{\partial \Delta K} = \begin{bmatrix} 0 \\ \rho \sin \beta \times \partial \Delta K \\ 0 \end{bmatrix} \quad 3.23$$

3.2.5 Linear Scanner & Laser Beam Range Bias

Laser range bias occurs when the laser beam gives inaccurate (biased) measurements. There are two possible cases; the first is a scaled bias that adds errors to the measurements as a function of the range, and the second is a constant bias that is added regardless of the range value (timing bias). The constant bias is discussed in this section while the other bias will not be discussed due to similarity between the results of both biases. The figure below shows the effects of a 50 cm bias that is added to the range value. Notice the smiling effect on the biased surface.

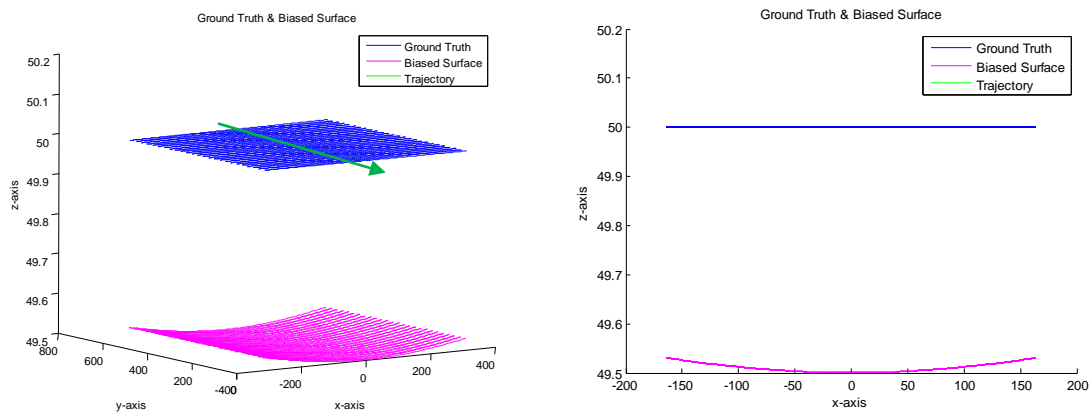


Figure 3.13: Isometric and front views of the accurate surfaces and the surfaces affected by range bias.

In the following figure (on the left), notice that the smiling effect appears only for the differences in the Z direction. However, other tests showed a slight curvature in the X differences as well. In the figure on the right, we notice that the errors are independent of the flying direction.

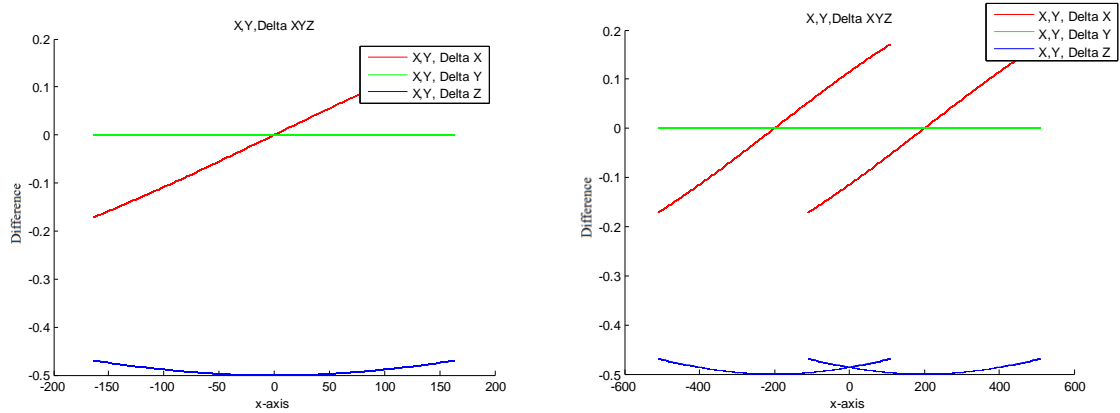


Figure 3.14: Differences resulting from the bias for a single strip (left) and two overlapping strips (right).

A mathematical proof of this bias effect is shown in Equations 3.24 to 3.28. As mentioned before, the boresighting parameters and the attitude angles are assumed to be zero for simplification purposes. Equation 3.28 shows that there is no error component acting in the Y direction. Errors are mainly in the Z direction, with a maximum bias when the look angle is downward ($\beta = 0^\circ$). Error appears and increases across the flying direction as the look angle strays from the nadir direction ($\beta = \pm 20^\circ$).

$$\vec{X}_G = \vec{X}_{O_t} + \underbrace{R_{\Omega_t, \Phi_t, K_t} \times R_{\Delta\Omega, \Delta\Phi, \Delta K}}_R \times \vec{P}_G + \underbrace{R_{\Omega_t, \Phi_t, K_t} \times R_{\Delta\Omega, \Delta\Phi, \Delta K}}_R \times R_{\alpha_t, \beta_t} \times \begin{bmatrix} 0 \\ 0 \\ -\rho_t \end{bmatrix} \quad 3.24$$

$$\frac{\partial \vec{X}_G}{\partial \rho} = \underbrace{R_{\Omega_t, \Phi_t, K_t} \times R_{\Delta\Omega, \Delta\Phi, \Delta K}}_R \times R_{\alpha_t, \beta_t} \times \begin{bmatrix} 0 \\ 0 \\ -1 \end{bmatrix} \quad 3.25$$

$$\frac{\partial \vec{X}_G}{\partial \rho} = \underbrace{R_{\Omega_t, \Phi_t, K_t} \times R_{\Delta\Omega, \Delta\Phi, \Delta K}}_R \times \begin{bmatrix} \cos \alpha \sin \beta \\ \sin \alpha \sin \beta \\ -\cos \beta \end{bmatrix} \quad 3.26$$

$$\frac{\partial \vec{X}_G}{\partial \rho} = \begin{bmatrix} R_{1,1} \cos \alpha \sin \beta + R_{1,2} \sin \alpha \sin \beta - R_{1,3} \cos \beta \\ R_{2,1} \cos \alpha \sin \beta + R_{2,2} \sin \alpha \sin \beta - R_{2,3} \cos \beta \\ R_{3,1} \cos \alpha \sin \beta + R_{3,2} \sin \alpha \sin \beta - R_{3,3} \cos \beta \end{bmatrix} \quad 3.27$$

Since the angle α is equal to zero for a linear scanner, and assuming $R = I$ yields,

$$\frac{\partial \vec{X}_G}{\partial \rho} = \begin{bmatrix} \sin \beta \times \partial \rho \\ 0 \\ -\cos \beta \times \partial \rho \end{bmatrix} \quad 3.28$$

As mentioned before, errors appear in the Z and across the flying (X) directions. The errors in the Z direction are not linear (Figure 3.14). It was mentioned also that the bias in the X direction is non-linear as well. The reason why the smiling effect is obvious in the Z curve and not in the X curve could be related to the behaviour of the sine and cosine curves. Figure 3.15-right shows both the sine and cosine curves. We are interested in the portion between -20 and 20 degrees (Figure 3.15-left), which is the rotating mirror rotational range. It is clear that the curvature in the cosine curve for this portion is higher.

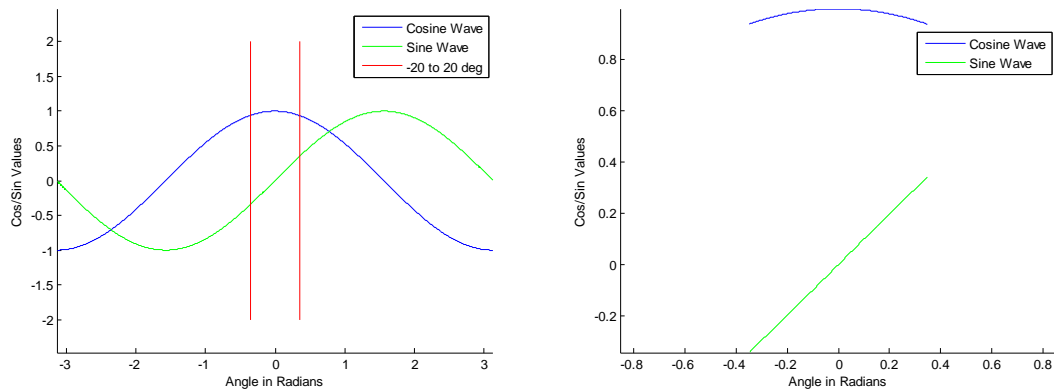


Figure 3.15: Curvature in the sine and cosine curves

3.2.6 Linear Scanner & Integrated GNSS/IMU Position Noise

In this subsection, random noise with a Gaussian distribution is added to the integrated GNSS/IMU position information. This random noise produces random errors with the same magnitude in the object space, as shown in Figure 3.16. Similarly to the biases introduced in the boresighting shifts, this noise is independent of the flying height (Equation 1.1) and the look angle.

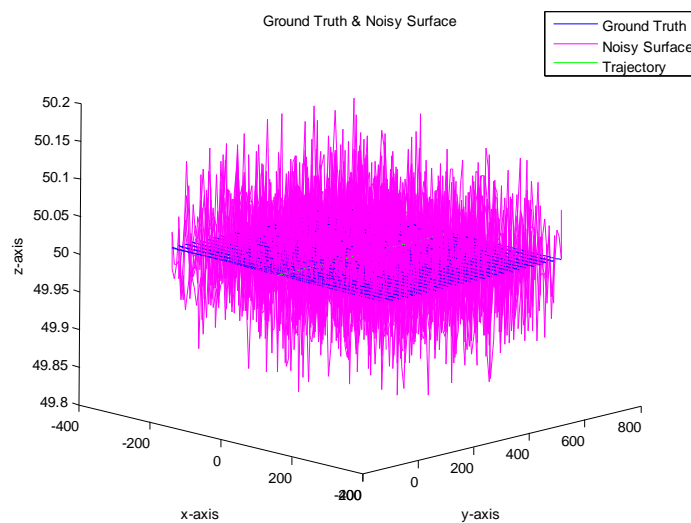


Figure 3.16: The effects of noise added to the integrated GNSS/IMU position on the object space

3.2.7 Linear Scanner & Integrated GNSS/IMU Attitude Noise

Usually, it is expected that random noise will lead to random errors in the derived point cloud. Moreover, it is commonly believed that random noise will not affect the relative accuracy (ASPRS LiDAR Committee (PAD), 2004). However, this is not the case for LIDAR systems. In other words, some of the random errors might affect the relative accuracy of the derived point cloud. Depending on the considered parameter, the relative effect of the corresponding noise level might not be the same. As an illustration, Figure

3.17 shows that a given attitude noise in the INS derived orientation will affect the nadir region of the flight trajectory less significantly than off nadir regions. Thus, the INS error will affect the relative accuracy of LIDAR derived point cloud.

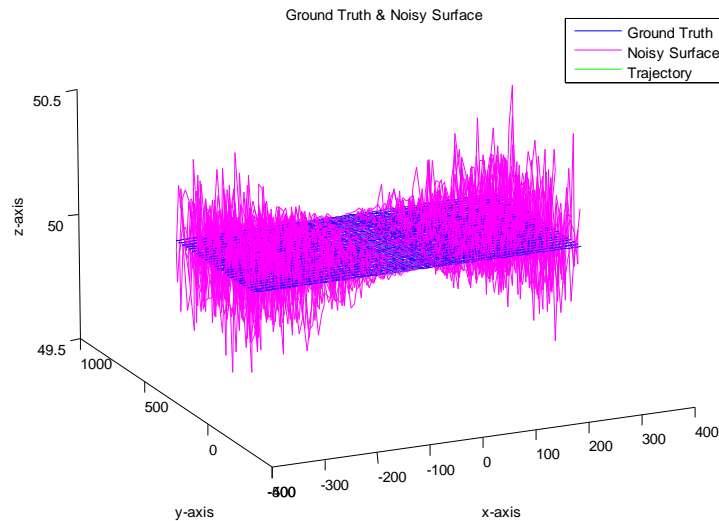


Figure 3.17: Error trend resulting from the addition of random (white) noise to the integrated GNSS/IMU attitude.

3.3 Conclusion

As shown in this chapter, biases have different influences on the reconstructed surfaces; some of them are dependent on the flight direction, while others are independent of the flying direction. Biases might affect the accuracy in a certain direction, or in some cases, can act in more than one direction. In addition, these biases vary in terms of the dependency on the look angle and on the flying height. From such information, an indication of the error source might be derived. The following table summarizes the behavior of various errors in the derived object space resulting from biases and noise in the system parameters and measurements, respectively.

Table 3-2: Summary of the relationships between bias/noise sources and the flying height, flying direction, and look angle¹.

	Flying Height	Flying Direction	Look Angle
Boresighting Offset Bias	Effect is independent of the Flying Height	Effect is independent of the Flying Direction	Effect is independent of the Look Angle
Boresighting Angular Bias	Effect Increases with the Flying Height	Effect Changes with the Flying Direction	Effect Changes with the Look Angle (Except Across the Flying Direction)
Laser Beam Range Bias	Effect is independent of the Flying Height	Effect is independent of the Flying Direction	Effect Depends on the Look Angle (Except Along the Flying Direction)
Laser Beam Angular Bias	Effect Increases with the Flying Height	Effect Changes with the Flying Direction (Except Along the Flying Direction)	Effect Changes with the Look Angle (Except Across the Flying Direction)
Position noise	Effect is independent of the Flying Height	-	Effect is independent of the Look Angle
Attitude noise	Effect Increases with the Flying Height	-	Effect Changes with the Look Angle (Except Across the Flying Direction)

¹ Assumptions: linear scanner, constant attitude & straight line trajectory, flying direction parallel to the Y axis, and a flat horizontal terrain.

Chapter Four: **METHODOLOGY**

4.1 Introduction

As suggested by the LiDAR equation (Equation 1.1), there is no redundancy in LiDAR measurements. This is because, due to the random nature of LiDAR points, one cannot measure the exact same point in different passes. Therefore, unlike with photogrammetric data, one cannot use explicit measures to assess the quality of LiDAR-derived positional information (e.g. the a posteriori variance component and the variance-covariance matrix of the derived ground coordinates of LiDAR footprints). Therefore, alternative quality control methods are necessary for this type of data. In this chapter, some measures for the internal and external quality control of LiDAR data will be provided.

The need has arisen for unconventional ways to define the correspondence between different strips. Lines and patches have been studied in this research, and have proven to work with both simulated and real data. To extract patches and lines from LiDAR data, a segmentation procedure must be run in order to isolate point clouds that belong to planar patches. Urban areas are rich with planar patches, which can be located on building roofs and, in general, on any manmade monuments. These patches are later intersected to produce the required linear features.

The methods addressed in this chapter include the Iterative Closest Patch method (ICPatch) and the Iterative Closest Point method (ICPoint). The ICPatch method has

proven to work efficiently, while the ICPpoint method is good only when looking for a fast and approximate way to qualify our data.

In this research, LiDAR_QC software was designed to make the LiDAR quality control process as smooth and as fast as possible. LiDAR quality control using lines and patches is implemented in this software in both fully automated and semi-automated procedures. A brief description of LiDAR_QC can be found in Chapter 5.

This chapter starts with a discussion of quality control using range and intensity images, which is proposed in Section 4.2. In Section 4.3, the quality control of LiDAR data using segmented planar patches will be discussed. At the beginning of the latter section, a brief description of LiDAR data segmentation is provided. Two methods of quality control using linear features (the endpoint method and the line constraint method) are discussed in Section 4.4. Section 4.5 describes the Iterative Closest Patch (ICPatch) method, and finally, the Iterative Closest Point (ICPoint) method is discussed in Section 4.6.

4.2 LiDAR Quality Control Using Interpolated Range and Intensity Images

This approach requires both interpolated range and intensity images. The intensity images are used to extract similar features in overlapping strips. The range image is used to obtain the height values for the planimetric coordinates retrieved from the intensity images. Figure 4.1 shows examples of intensity (left) and range (right) images generated from a LiDAR point cloud.

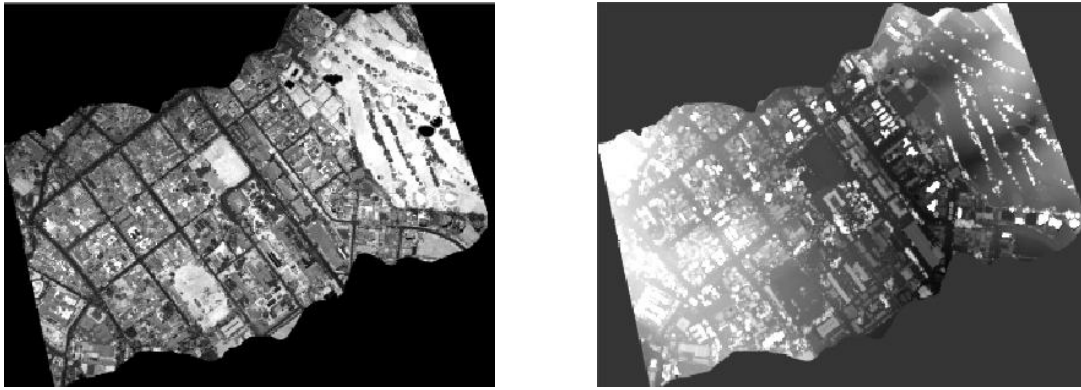


Figure 4.1: Intensity image (left) and range image (right) generated from a LiDAR point cloud

In this approach, the user must manually measure the points in both strips, by first identifying corner features in the intensity image of the first strip and then, using his/her judgment, decide the proper location of its conjugate in the second strip, as in Figure 4.2. The height data could be extracted automatically from the range image at the planimetric location of the identified points in the intensity images. These heights could also be extracted from the raw measurement using the nearest neighbour technique. Unfortunately, this method is time consuming due to the manual nature of the procedure. Moreover, the interpolation of the intensity and range images adds errors to the data and thus the results of this method might be unreliable and incorrect.

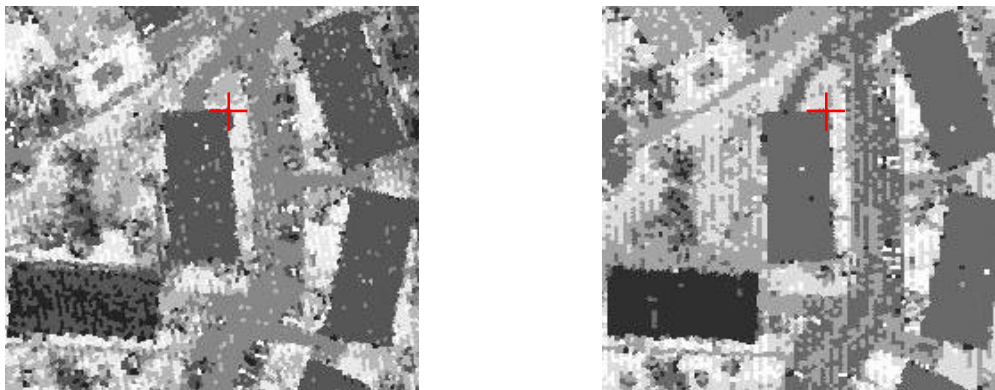


Figure 4.2: Manual extraction of conjugate points from overlapping LiDAR strips. The red crosses represent the user defined locations of the conjugate features.

A semi-automated process using the above method was developed using the concept of cross correlation. Since the intensity images are registered, once a point is selected in the left strip, its location can be used as an origin for the cross correlation. A window, with a predefined size, is the search space. Then a moving matching window within the search space is compared with the template to define the similarity measure. Then, the location with the highest similarity measure represents the corresponding point location.

Figure 4.3 shows the results from the cross correlation procedure. Each red cross in the left image represents a user defined location (manually clicked) and each red cross in the right strip represents the origin of the corresponding search space. Each blue cross is the best match to a template defined from the left strip (i.e. the location of the matching window with the highest correlation coefficient). Note that some of the cross correlation results fail to find the right conjugate point (there are ambiguities) due to the poor detail in the image. This problem can be reduced by increasing the template size, but on the other hand, doing so would lead to a greater required calculation time. Also, the careful selection of the reference template is necessary.

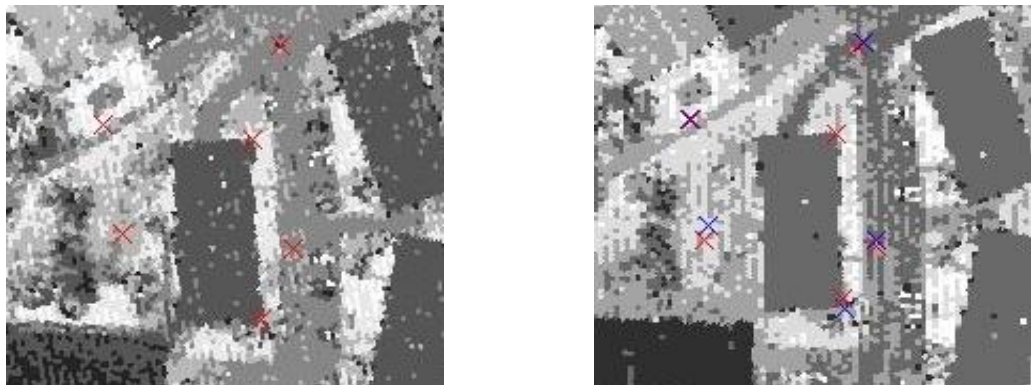


Figure 4.3: Semi-automatic extraction of conjugate points from overlapping LiDAR strips.

4.3 LiDAR Quality Control Using Patches

4.3.1 Introduction

Conjugate planar patches in overlapping strips should be coplanar, regardless of the flying direction or any other parameters, unless there are biases affecting the data. Using this fact, planar patches can be used to qualify or detect biases in the LiDAR datasets. Before we discuss this method, a procedure that is used for the segmentation of LiDAR data (extraction of planar patches) is discussed in the following section.

4.3.2 Segmentation of LiDAR Data

A new approach for planar patch segmentation from LiDAR data was developed by Kim et al. (2007). This segmentation procedure begins with a neighbourhood definition based on the physical characteristics of the surfaces. Then the surface normals (which are used as attributes) are calculated from predefined origins to the computed planar patches. These attributes are added to an accumulator array (Figure 4.4, in a form of a histogram) for the purpose of clustering. Two origins are used to derive the aforementioned attributes for each patch, in order to avoid ambiguities. The boundaries of the clusters are then studied in order to disambiguate co-planar patches that represent different physical surfaces. Please refer to Kim, et al., 2007 for further explanation. Once the segmentation process is done as shown in Figure 4.5-right, LiDAR data is now classified into groups which are ready to be matched with other patches from different strips.

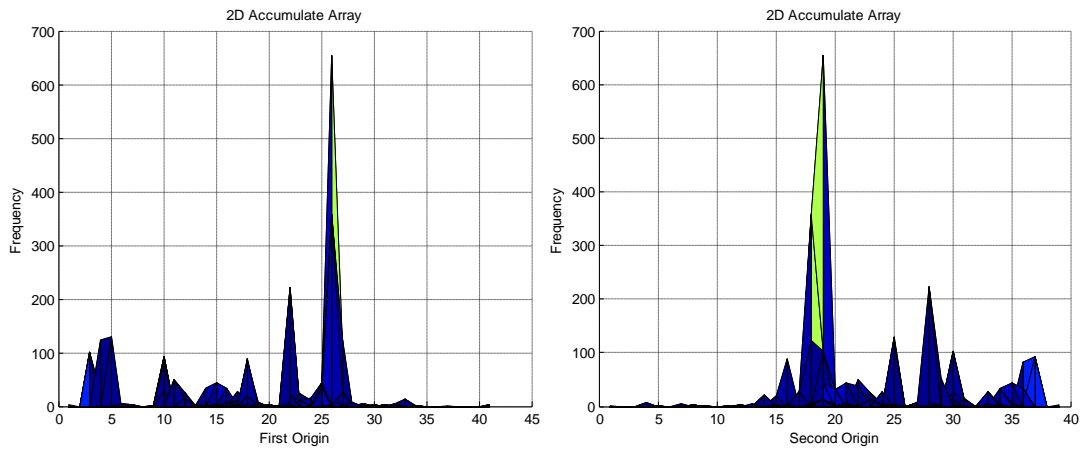


Figure 4.4: Two side views of an accumulator array used in the segmentation algorithm.

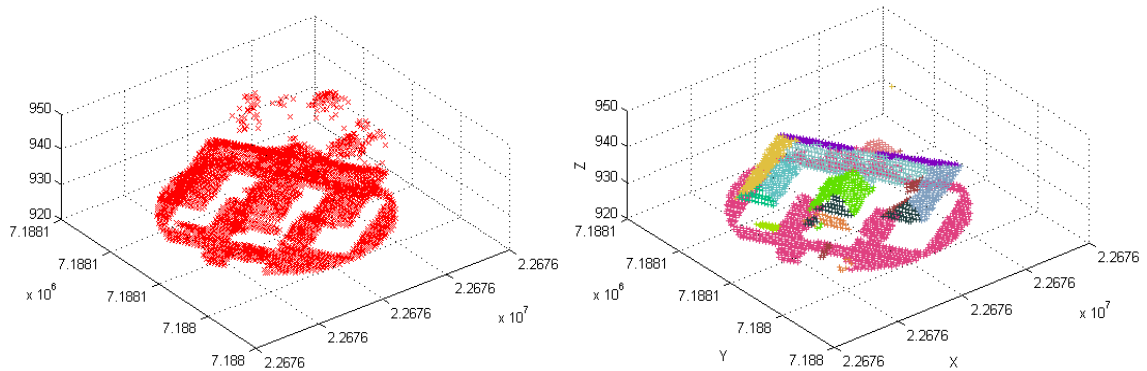


Figure 4.5: LiDAR point cloud before the segmentation (left) and after running the segmentation algorithm (right); different colors indicate different planar patches.

4.3.3 Patch Matching Process

Once the segmentation of LiDAR data is done in a common area for two overlapping strips, it is time to start matching conjugate patches, which represent the same physical surface. This could be accomplished through an automatic process as described below:

1. Generate the centroid for each patch in both strips; since conjugate patches are similar, the centroids of the conjugate patches should be very close to each other. Therefore, the closest centroid in one strip (or the centroids

that is located within a buffer from the target centroid in the other strip) is/are assumed to be a potential match.

2. The angle(s) between the first patch and the potential conjugate patch(es) are compared to determine the degree of similarity between these patches.
3. Once the patch with the best matching parameters is found, both patches are visualized to ensure the correctness of the chosen patch, and to determine the number of points constituting these patches; patches containing more points are preferred. An example of this visualization is shown in Figure 4.6.

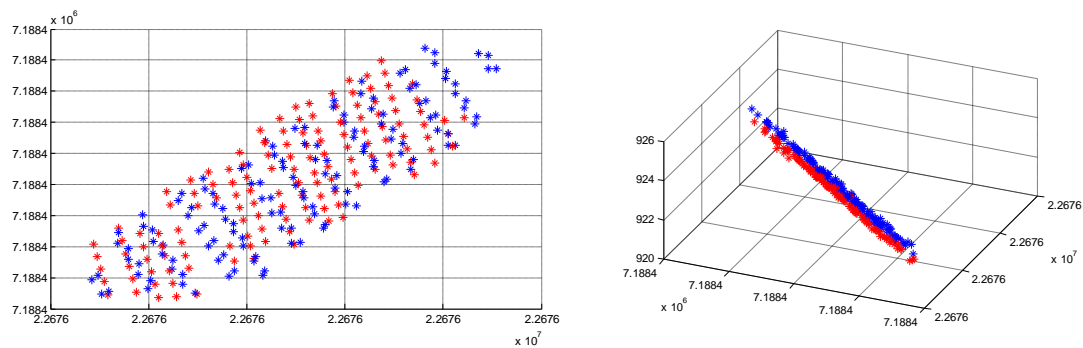


Figure 4.6: Top view of matched patches (left) and a side view (right) showing the co-planarity of the patches.

4.3.4 Point Based Method

Once we have obtained conjugate planar patches, the relationship between patches with similar characteristics must be established. Usually, LiDAR data is provided to the end user with an estimate of the point accuracy. The idea in this method is to expand or relax these points' accuracies along the direction parallel to the plane, while maintaining the original accuracy along the direction normal to the plane (Habib, et al., 2007). Once this is accomplished, a point to point relationship could be established, even

if these points are not conjugate. A description of how to expand the aforementioned error ellipsoids is in the following paragraphs.

Assume Figure 4.7-a is a point in the XYZ coordinate system with the error ellipsoid shown. The variance covariance matrix representing this error ellipse is transformed based on the rotation matrix R (rotation matrix between the reference frame coordinate system (XYZ) and the plane coordinate system (UVW), where UV are along the plane and W is normal to the plane parallel direction) obtained from the plane fitting process. The matrix is transformed into the plane coordinate system according to the law of error propagation, Equation 4.1, as shown in Figure 4.7-b.

$$\Sigma_{UVW} = R \times \begin{bmatrix} \sigma_X^2 & \sigma_{XY} & \sigma_{XZ} \\ \sigma_{XY} & \sigma_Y^2 & \sigma_{YZ} \\ \sigma_{XZ} & \sigma_{YZ} & \sigma_Z^2 \end{bmatrix} \times R^T \quad 4.1$$

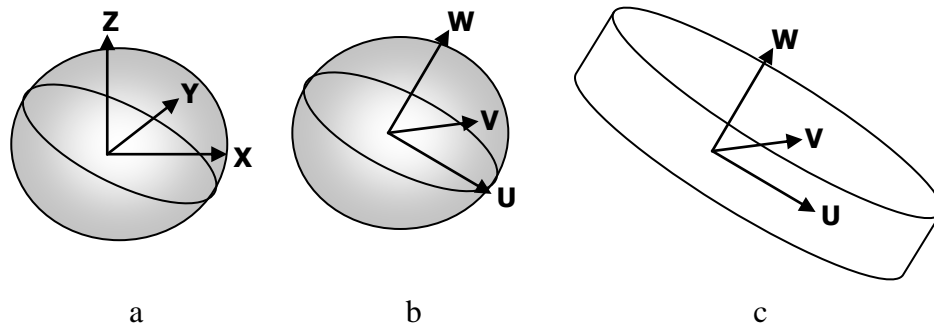


Figure 4.7: Conceptual basis for using planar patches in a point-based approach for the determination of the conformal transformation parameters between two 3D datasets.

Next, the variances are artificially enlarged along the direction parallel to the plane, which is, in this case, the UV plane, according to Equation 4.2 and Figure 4.7-c.

$$\sum'_{UVW} = R \times \begin{bmatrix} \sigma_X^2 & \sigma_{XY} & \sigma_{XZ} \\ \sigma_{XY} & \sigma_Y^2 & \sigma_{YZ} \\ \sigma_{XZ} & \sigma_{YZ} & \sigma_Z^2 \end{bmatrix} \times R^T + \begin{bmatrix} N & 0 & 0 \\ 0 & M & 0 \\ 0 & 0 & 0 \end{bmatrix} \quad 4.2$$

In the above equation, the N and M terms are user-defined, or can be set automatically using previous knowledge of the plane dimensions.

One might argue that it would be better to multiply the expanded variances instead of adding them (Equation 4.3). Both equations are valid as long as we are aware of the special cases involved in each equation. For example, the user might input very small variance values that will not make the expanded values big enough.

$$\sum_{UVW} = R \times \begin{bmatrix} \sigma_X^2 & \sigma_{XY} & \sigma_{XZ} \\ \sigma_{XY} & \sigma_Y^2 & \sigma_{YZ} \\ \sigma_{XZ} & \sigma_{YZ} & \sigma_Z^2 \end{bmatrix} \times R^T \quad 4.3$$

$$\sum'_{UVW} = \begin{bmatrix} \sigma_U^2 \times N & \sigma_{UV} & \sigma_{UW} \\ \sigma_{UV} & \sigma_V^2 \times M & \sigma_{VW} \\ \sigma_{UW} & \sigma_{VW} & \sigma_W^2 \end{bmatrix}$$

Once the variances are expanded, they may be transformed back to the original XYZ coordinate system, as shown in Equation 4.4

$$\sum'_{XYZ} = R^T \times \sum'_{UVW} \times R \quad 4.4$$

From here, any point in the first plane could be considered a match for any point in the second plane, where the only restriction is that the plane with the larger number of points should be truncated to have the same number of points as found in the other plane. A minimum of four patches (three non-parallel and one parallel) are required, in the ideal case, to define the datum parameters. For further explanation of the minimum requirement, please refer to Section 4.5 in Ghanma, 2006.

A 3D-Conformal Transformation is a transformation that preserves the geometry of the objects being transformed; it uses three translations, three rotations, and a scale factor. This transformation is assumed to be valid between the points from different patches; however, there is no assumption that the 3D-Conformal Transformation is the best model to be used for LiDAR error modeling. The target here is to detect any biases or inconsistencies in the LiDAR data. This could be done using the conformal transformation in the case of no biases; the 3D conformal parameters are estimated as one for the scale factor and zeros for the remaining parameters. However, if biases exist, the estimated parameters will deviate from the aforementioned values.

A least squares solution is used to estimate the three rotations, three translations, and scale factor. Since no biases is assumed to exist in LiDAR data, initial approximations of these unknowns can be considered to be three zeros, three zeros, and one, respectively. In order to summarise the process flow of the least squares solution, let us define the following entities:

XYZ_1 A $[3n \times 1]$ vector that contains the point coordinates of the first dataset; n represents the number of points.

XYZ_2 A $[3n \times 1]$ vector that contains the point coordinates of the second data set.

$SXYZ_1$ A $[3 \times 3]$ matrix that contains the variance-covariance information for each point in dataset 1.

$SXYZ_2$ A $[3 \times 3]$ matrix that contains the variance-covariance information for each point in dataset 2.

- X_T Initial approximation of the translation along the X-axis.
- Y_T Initial approximation of the translation along the Y-axis.
- Z_T Initial approximation of the translation along the Z-axis.
- S Initial approximation of the scale factor between the two datasets.
- Ω Initial approximation of the rotation around the X-axis.
- Φ Initial approximation of the rotation around the Y-axis.
- K Initial approximation of the rotation around the Z-axis.
- R The $[3 \times 3]$ rotation matrix resulting from Equation 4.5.
- A The $[3n \times 7]$ design matrix.
- \mathcal{W} The $[3 \times 3]$ weight matrix built for each point.
- W The $[3n \times 3n]$ block diagonal weight matrix; each block is $[3 \times 3]$ and has n subblocks of \mathcal{W} along the diagonal.
- N The $[7 \times 7]$ constructed normal matrix.
- L A $[3n \times 1]$ observation vector.
- X The $[7 \times 1]$ estimated corrections to the unknown parameters.
- i An integer counter that represents the i^{th} row in a given matrix; i is a zero-based counter with a maximum value of $3n - 1$.

The first step is to build the rotation matrix, as shown in Equation 4.5, in order to build the weight matrix (\mathcal{W}) of each individual point.

$$R = R_{\Omega} \times R_{\Phi} \times R_K \quad 4.5$$

$$\begin{bmatrix} R_{1,1} & R_{1,2} & R_{1,3} \\ R_{2,1} & R_{2,2} & R_{2,3} \\ R_{3,1} & R_{3,2} & R_{3,3} \end{bmatrix} = \begin{bmatrix} 1 & 0 & 0 \\ 0 & \cos \Omega & -\sin \Omega \\ 0 & \sin \Omega & \cos \Omega \end{bmatrix} \times \begin{bmatrix} \cos \Phi & 0 & \sin \Phi \\ 0 & 1 & 0 \\ -\sin \Phi & 0 & \cos \Phi \end{bmatrix} \times \begin{bmatrix} \cos K & -\sin K & 0 \\ \sin K & \cos K & 0 \\ 0 & 0 & 1 \end{bmatrix}$$

Now, $SXYZ_1$ and $SXYZ_2$ are merged together, after transforming $SXYZ_2$ to the $SXYZ_1$ coordinate system, as shown in the following set of equations:

$$XYZ_{1true} = X_T + S \times R \times XYZ_{2true} \quad 4.6$$

$$[XYZ_{1obs} - e_{XYZ_1}] = X_T + S \times R \times [XYZ_{2obs} - e_{XYZ_2}] \quad 4.7$$

$$XYZ_{1obs} = X_T + S \times R \times XYZ_{2obs} + [e_{XYZ_1} - S \times R \times e_{XYZ_2}] \quad 4.8$$

$$D\{e_{XYZ_1} - S \times R \times e_{XYZ_2}\} = SXYZ_1 + S \times R \times SXYZ_2 \times R^T \times S = SXYZ = \begin{bmatrix} SXX & SXY & SXZ \\ SXY & SYZ & SYZ \\ SXZ & SYZ & SZZ \end{bmatrix} \quad 4.9$$

The weight matrix \mathcal{W} of each point is simply the inverse of the variance covariance matrix resulting from Equation 4.10.

$$\mathcal{W} = SXYZ^{-1} \quad 4.10$$

After computing \mathcal{W} as shown in Equation 4.10, the \mathcal{W} matrix can now be converted to its final form by adding the weight information for all the points in a block diagonal shape, as shown in Equation 4.11

$$W = \begin{bmatrix} \mathcal{W}_0 & \cdots & 0 \\ \vdots & \ddots & \vdots \\ 0 & \cdots & \mathcal{W}_{n-1} \end{bmatrix} \quad 4.11$$

The L matrix can be computed by subtracting the points' values in XYZ_2 from their corresponding values in XYZ_1 , after applying the transformation function. Equations 4.12, 4.13, and 4.14 represent the procedure for the X, Y, and Z values, respectively.

$$L_{i \times 3+0} = XYZ_{1i,1} - X_T - S \times [R_{1,1} \quad R_{1,2} \quad R_{1,3}] \times [XYZ_{2i,1} \quad XYZ_{2i,2} \quad XYZ_{2i,3}]^T \quad 4.12$$

$$L_{i \times 3+1} = XYZ_{1i,2} - Y_T - S \times [R_{2,1} \quad R_{2,2} \quad R_{2,3}] \times [XYZ_{2i,1} \quad XYZ_{2i,2} \quad XYZ_{2i,3}]^T \quad 4.13$$

$$L_{i \times 3+2} = XYZ_{1i,3} - Z_T - S \times [R_{3,1} \quad R_{3,2} \quad R_{3,3}] \times [XYZ_{2i,1} \quad XYZ_{2i,2} \quad XYZ_{2i,3}]^T \quad 4.14$$

Each point yields three equations; the partial derivatives of these equations with respect to the parameters can be found in Appendix A. Once the formulas for the partial derivatives are built, they are used to build the design matrix, as shown below.

$$A = \begin{bmatrix} \frac{\partial X_{P1}}{\partial X_T} & \frac{\partial X_{P1}}{\partial Y_T} & \frac{\partial X_{P1}}{\partial Z_T} & \frac{\partial X_{P1}}{\partial S} & \frac{\partial X_{P1}}{\partial \Omega} & \frac{\partial X_{P1}}{\partial \Phi} & \frac{\partial X_{P1}}{\partial K} \\ \frac{\partial Y_{P1}}{\partial X_T} & \frac{\partial Y_{P1}}{\partial Y_T} & \frac{\partial Y_{P1}}{\partial Z_T} & \frac{\partial Y_{P1}}{\partial S} & \frac{\partial Y_{P1}}{\partial \Omega} & \frac{\partial Y_{P1}}{\partial \Phi} & \frac{\partial Y_{P1}}{\partial K} \\ \frac{\partial Z_{P1}}{\partial X_T} & \frac{\partial Z_{P1}}{\partial Y_T} & \frac{\partial Z_{P1}}{\partial Z_T} & \frac{\partial Z_{P1}}{\partial S} & \frac{\partial Z_{P1}}{\partial \Omega} & \frac{\partial Z_{P1}}{\partial \Phi} & \frac{\partial Z_{P1}}{\partial K} \\ \frac{\partial X_{P2}}{\partial X_T} & \frac{\partial X_{P2}}{\partial Y_T} & \frac{\partial X_{P2}}{\partial Z_T} & \frac{\partial X_{P2}}{\partial S} & \frac{\partial X_{P2}}{\partial \Omega} & \frac{\partial X_{P2}}{\partial \Phi} & \frac{\partial X_{P2}}{\partial K} \\ \frac{\partial Y_{P2}}{\partial X_T} & \frac{\partial Y_{P2}}{\partial Y_T} & \frac{\partial Y_{P2}}{\partial Z_T} & \frac{\partial Y_{P2}}{\partial S} & \frac{\partial Y_{P2}}{\partial \Omega} & \frac{\partial Y_{P2}}{\partial \Phi} & \frac{\partial Y_{P2}}{\partial K} \\ \frac{\partial Z_{P2}}{\partial X_T} & \frac{\partial Z_{P2}}{\partial Y_T} & \frac{\partial Z_{P2}}{\partial Z_T} & \frac{\partial Z_{P2}}{\partial S} & \frac{\partial Z_{P2}}{\partial \Omega} & \frac{\partial Z_{P2}}{\partial \Phi} & \frac{\partial Z_{P2}}{\partial K} \\ \vdots & \vdots & \vdots & \vdots & \vdots & \vdots & \vdots \\ \frac{\partial X_n}{\partial X_T} & \frac{\partial X_n}{\partial Y_T} & \frac{\partial X_n}{\partial Z_T} & \frac{\partial X_n}{\partial S} & \frac{\partial X_n}{\partial \Omega} & \frac{\partial X_n}{\partial \Phi} & \frac{\partial X_n}{\partial K} \\ \frac{\partial Y_n}{\partial X_T} & \frac{\partial Y_n}{\partial Y_T} & \frac{\partial Y_n}{\partial Z_T} & \frac{\partial Y_n}{\partial S} & \frac{\partial Y_n}{\partial \Omega} & \frac{\partial Y_n}{\partial \Phi} & \frac{\partial Y_n}{\partial K} \\ \frac{\partial Z_n}{\partial X_T} & \frac{\partial Z_n}{\partial Y_T} & \frac{\partial Z_n}{\partial Z_T} & \frac{\partial Z_n}{\partial S} & \frac{\partial Z_n}{\partial \Omega} & \frac{\partial Z_n}{\partial \Phi} & \frac{\partial Z_n}{\partial K} \end{bmatrix}_{3n \times 7} \quad 4.15$$

After all the required matrices have been prepared, a least squares solution can be performed in order to obtain the corrections to the given initial approximations (Equation 4.16). And the quality of the least squares solution could be estimated by calculating sigma a posteriori as in Equation 4.17.

$$X_{Correction} = [A^T \times W \times A]^{-1} \times A^T \times W \times L \quad 4.16$$

$$\hat{\sigma}_o^2 = \frac{V^T \times W \times V}{Redundancy}, \text{ where } V = A \times X_{Correction} - L \quad 4.17$$

These corrections are added to the initial approximations in order to rebuild the matrices for a second loop of the least squares solution; this process is repeated until the

estimated sigma is not changing significantly. The following diagram shows the work flow for the iterative solution.

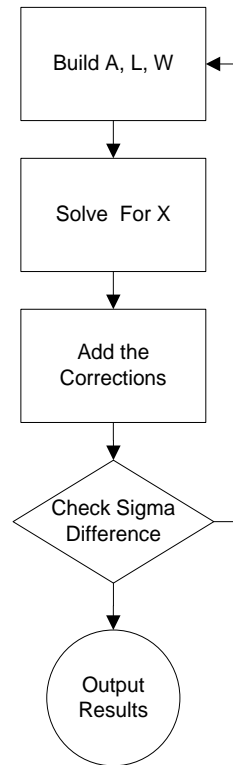


Figure 4.8: The flow of the least squares solution.

Sometimes, numerical instability is experienced due to the huge values of XYZ_1 and XYZ_2 used to build the N matrix. This instability occurs when trying to invert the N matrix, and might cause wrong results. A simple solution to overcome this problem is to subtract a constant value (the centroid of one of the datasets) from the given XYZ_1 and XYZ_2 values. However, it was proven that this shift affects the estimated translation parameters, and that the best value for the shift is the centroid of the point cloud. A summary of this proof is provided below.

We have the following 3D-Conformal Equation,

$$XYZ_1 = X_T + S \times R \times XYZ_2 \quad 4.18$$

By changing the origin of the reference frame, it is expected that the transformation parameters will change as shown in Equation 4.19,

$$[XYZ_1 - \bar{X}] = \hat{X}_T + \hat{S} \times \hat{R} \times [XYZ_2 - \bar{X}] \quad 4.19$$

In the above equation, \bar{X} is the centroid of XYZ_2 . Now, we would like to investigate the relationship between (X_T, S, R) and $(\hat{X}_T, \hat{S}, \hat{R})$,

$$XYZ_1 = \hat{X}_T + \bar{X} - \hat{S} \times \hat{R} \times \bar{X} + \hat{S} \times \hat{R} \times XYZ_2 \quad 4.20$$

$$XYZ_1 = [\hat{X}_T + (I_3 - \hat{S} \times \hat{R}) \times \bar{X}] + \hat{S} \times \hat{R} \times XYZ_2 \quad 4.21$$

The above equation is valid for all the points within X_{S1} & X_{S2} if and only if:

1. $X_T = \hat{X}_T + (I_3 - \hat{S} \times \hat{R}) \times \bar{X}$.
2. $S \times R = \hat{S} \times \hat{R} \Rightarrow S = \hat{S}$ and $R = \hat{R}$.

From the above points, it is concluded that changes due to the shift affect the translation vector only. Now, we will investigate the correctness of choosing the centroid coordinates as the shift. The estimated shifts in the second dataset before and after applying the transformation could be calculated as bellow.

$$\Delta X = [XYZ_2 - \bar{X}] - \hat{X}_T - \hat{S} \times \hat{R} \times [XYZ_2 - \bar{X}] \quad 4.22$$

Now, summing all the values in ΔX gives the following equation,

$$\sum \Delta X = \sum [XYZ_2 - \bar{X}] - \sum \hat{X}_T - \hat{S} \times \hat{R} \times \sum [XYZ_2 - \bar{X}] \quad 4.23$$

Rearranging Equation 4.23 and replacing $\sum \bar{X}$ with $n \times \bar{X}$ and $\sum \hat{X}_T$ with $n \times \hat{X}_T$ yields,

$$\sum \Delta X = \sum XYZ_2 - n \times \bar{X} - n \times \hat{X}_T - \hat{S} \times \hat{R} \times \left[\sum XYZ_2 - n \times \bar{X} \right] \quad 4.24$$

Knowing that $\sum XYZ_{2_{true}} = n \times \bar{X}$, one yields,

$$\sum \Delta X = -n \times \hat{X}_T \Rightarrow \hat{X}_T = -\frac{\sum \Delta X}{n} \quad 4.25$$

From the above, we conclude that the estimated shifts \hat{X}_T is equal to the average shifts for all the points in the second dataset. Which happens only and only if the origin of the dataset is shifted to be at the centroid of the same dataset.

4.4 LiDAR Quality Control Using Lines

4.4.1 Introduction

Lines have proven to be useful in various photogrammetric applications (e.g. Camera Calibration, Single Photo Resection, etc.) (Habib, A; Morgan, M; Kim, E.M; Cheng, R, 2004). In the same manner, lines are thought to be useful for the purpose of LiDAR Quality Control.

Once the patches are extracted, as described in Section 4.3, lines can be obtained by intersecting neighbouring patches. Usually, the lines used have physical representations. Virtual lines could be used as well, as long as they are not too far from their patches, because the reliability of the lines is reduced if they are located far from their patches. Figure 4.9 shows a typical line extracted from two patches on the same building. Another acceptable line shape could be as shown in Figure 4.10.

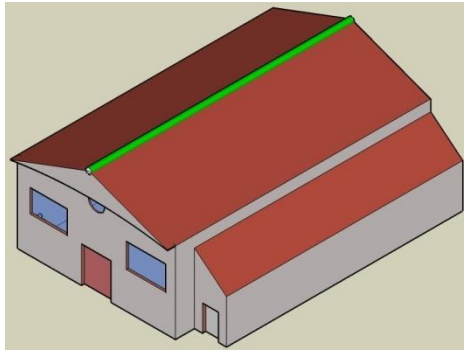


Figure 4.9: Physical line extracted from two patches on the same building.

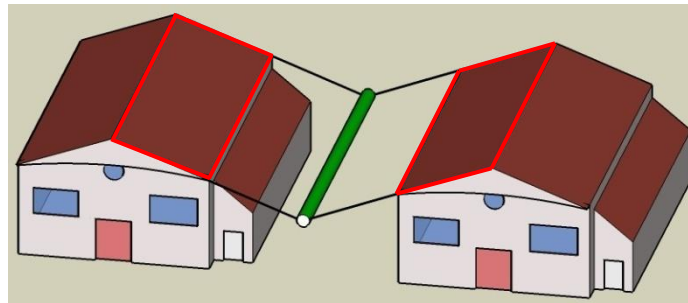


Figure 4.10: Non-physical (virtual) line extracted from two neighbouring patches on two different buildings.

When extracting the lines, it is up to the operator to decide whether the line is acceptable. A threshold value for the distance between the line and the patches could be introduced in order to automate the line extraction process. In this research, the threshold is set to be twice the point density. Figure 4.11 shows a case in which the line will be rejected. Unreliable lines result in incorrect estimates of the bias between the LiDAR strips. The aforementioned threshold is also used to determine the extreme points (endpoints) of the lines, by simply projecting all the points that fall within a certain buffer onto the line segment (Figure 4.12) and selecting the points farthest along the line segment to be the endpoints.

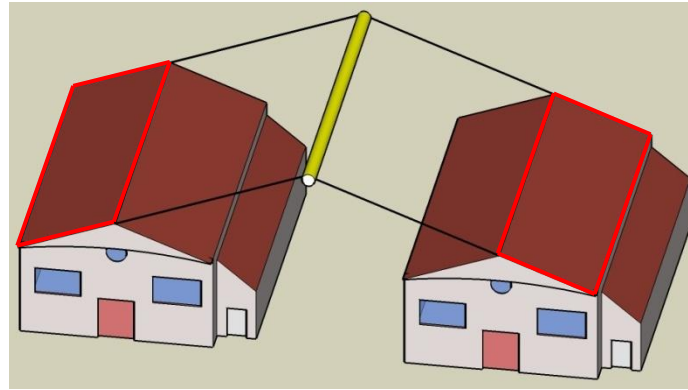


Figure 4.11: Non-physical line extracted from two non-neighbouring patches on two different buildings.

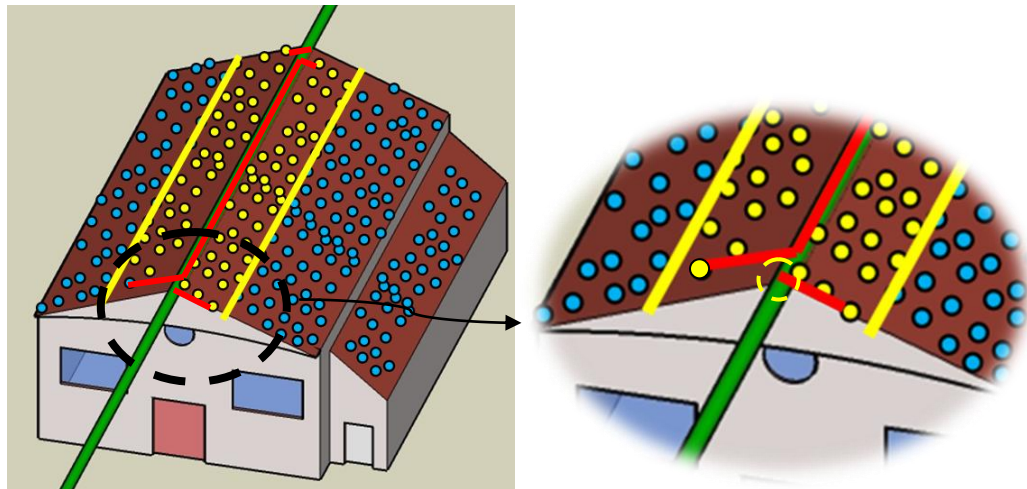


Figure 4.12: Projecting points within a buffer to define the line endpoints.

The matching of conjugate lines is done in a fully automated procedure. Simply, the following three conditions must apply in order to consider a pair of lines in overlapping strips to be conjugate:

1. The average normal distance between the lines should be less than a threshold.

The normal distance is the average of the normal distances shown in Figure 4.13.

2. The angle between the two lines should be small (less than 5 degrees); in other words, the differences between the parameters for the first line and those for the second line should be very small.
3. Finally, a reasonable overlap between the lines should exist; 70% overlap is an example of a reasonable overlap percentage. This overlap percentage is defined as the shortest distance between the two lines' endpoints, divided by the longest distance between endpoints (projected at one of the lines). Figure 4.13 shows an example of the overlap between two lines.
4. Finally, after all the lines are matched, they will be visualized to the user to make a judgment on which lines should be included and which ones are outliers.

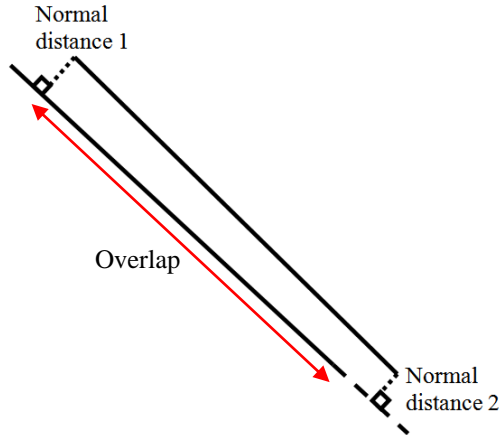


Figure 4.13: Normal distance in a line pair.

4.4.2 Line Endpoint Method

This method employs the same concept introduced in Section 4.3 but in this case, the variances are expanded along one dimension only, which is, in this case, along the direction parallel to the line.

Using the error propagation formula shown in Equation 4.26, the variances of the lines' endpoints are transformed to the UVW coordinate system, in which the U axis is parallel to the line, and the V and W axes are perpendicular to the U axis. Then, using the same method used in the previous expansion process, the endpoint variances are expanded along the line direction, as shown in Equation 4.27.

$$\sum_{UVW} = R \times \begin{bmatrix} \sigma_X^2 & \sigma_{XY} & \sigma_{XZ} \\ \sigma_{XY} & \sigma_Y^2 & \sigma_{YZ} \\ \sigma_{XZ} & \sigma_{YZ} & \sigma_Z^2 \end{bmatrix} \times R^T \quad 4.26$$

Figure 4.14 presents the conceptual basis of using linear features with the point-based approach for the determination of the conformal transformation parameters between two 3D datasets.

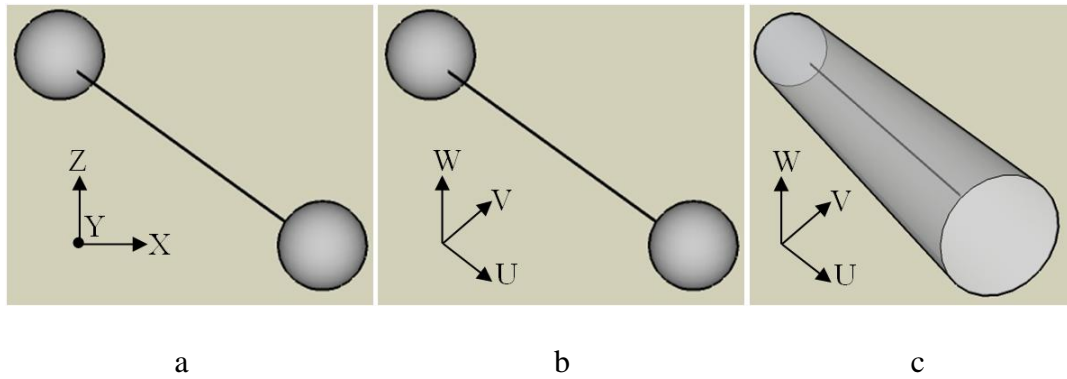


Figure 4.14: Conceptual basis for the use of linear features with the point-based approach for the determination of the conformal transformation parameters between two 3D datasets.

$$\sum'_{UVW} = R \times \begin{bmatrix} \sigma_X^2 & \sigma_{XY} & \sigma_{XZ} \\ \sigma_{XY} & \sigma_Y^2 & \sigma_{YZ} \\ \sigma_{XZ} & \sigma_{YZ} & \sigma_Z^2 \end{bmatrix} \times R^T + \begin{bmatrix} N & 0 & 0 \\ 0 & 0 & 0 \\ 0 & 0 & 0 \end{bmatrix} \quad 4.27$$

Once the variances are expanded as shown in Figure 4.14-c, they can be returned to the XYZ coordinate system using Equation 4.28.

$$\sum'_{XYZ} = R^T \times \sum'_{UVW} \times R \quad 4.28$$

Now, the matrices required to perform a least squares solution can be built in a similar way to that discussed in Section 4.3.4. Each endpoint yields three equations (six equations for each line pair); the partial derivatives of the observations with respect to the parameters are exactly the same as the Equations shown in Appendix A. Once the formulas for the partial derivatives are built, they are used to build the design matrix, as shown in Equation 4.15. A minimum of two non-coplanar lines are needed to define the reference datum.

After all the required matrices are prepared, a least squares solution is performed in order to obtain the corrections to the given initial approximations (Equation 4.16). The resulting corrections are added to the initial approximations in order to rebuild the matrices for a second loop of the least squares solution. This process is repeated until no significant change occurs in the computed a posteriori sigma value.

4.4.3 Line Constraint Method (Collinearity Method)

In contrast to the method in Section 4.4.2, endpoints in extracted lines are not used directly. The collinearity of the conjugate lines, which is defined by the lines' endpoints, is instead used to provide the necessary constraints for the definition of the transformation parameters.

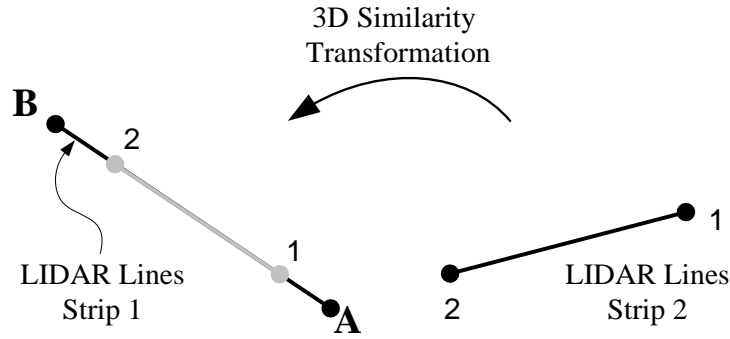


Figure 4.15: Corresponding lines represented by non-conjugate endpoints from two different LiDAR strips.

From Figure 4.15, we are able to define a constraint such that point 1 can be represented with respect to the line AB. Point 1, after applying the required 3D conformal transformation, is equal to the point A plus a scale factor multiplied by the vector \overrightarrow{AB} . A mathematical representation of this constraint is shown below.

$$\begin{bmatrix} X_T \\ Y_T \\ Z_T \end{bmatrix} + S \times R_{\Omega, \Phi, K} \times \begin{bmatrix} X_1 \\ Y_1 \\ Z_1 \end{bmatrix} = \begin{bmatrix} X_A \\ Y_A \\ Z_A \end{bmatrix} + \lambda_1 \times \begin{bmatrix} X_B - X_A \\ Y_B - Y_A \\ Z_B - Z_A \end{bmatrix} \quad 4.29$$

Where $[X_T \ Y_T \ Z_T]^T$ is the translation between the origins of the coordinate systems of the two LiDAR strips, S and λ_1 are scale factors, and $R_{\Omega, \Phi, K}$ is an orthogonal rotation matrix.

A similar constraint equation can be written for point 2 (Equation 4.30). It is worth mentioning here that it is not important to match a point from one line with the closest point in the conjugate line. For instance, the constraint equation for point 1 can be written with respect to either one of the points A and B. The scale factors λ_1 and λ_2 take care of either case.

$$\begin{bmatrix} X_T \\ Y_T \\ Z_T \end{bmatrix} + S \times R_{\Omega,\Phi,K} \times \begin{bmatrix} X_2 \\ Y_2 \\ Z_2 \end{bmatrix} = \begin{bmatrix} X_A \\ Y_A \\ Z_A \end{bmatrix} + \lambda_2 \times \begin{bmatrix} X_B - X_A \\ Y_B - Y_A \\ Z_B - Z_A \end{bmatrix} \quad 4.30$$

Next, subtracting Equation 4.30 from Equation 4.29 yields:

$$S \times R_{\Omega,\Phi,K} \times \begin{bmatrix} X_2 - X_1 \\ Y_2 - Y_1 \\ Z_2 - Z_1 \end{bmatrix} = [\lambda_2 - \lambda_1] \times \begin{bmatrix} X_B - X_A \\ Y_B - Y_A \\ Z_B - Z_A \end{bmatrix} \quad 4.31$$

The three scale factors S , λ_2 , and λ_1 can be substituted by one scale factor λ . After the substitution and rearrangement of the above equation, the following equation is produced:

$$\lambda \times R_{\Omega,\Phi,K} \times \begin{bmatrix} X_2 - X_1 \\ Y_2 - Y_1 \\ Z_2 - Z_1 \end{bmatrix} = \begin{bmatrix} X_B - X_A \\ Y_B - Y_A \\ Z_B - Z_A \end{bmatrix} \quad 4.32$$

Similarly to the manipulation that is done in forming the collinearity equations, we divide the first two rows by the third one in order to eliminate the scale factor from the above equation. This will result in the following:

$$\frac{X_B - X_A}{Z_B - Z_A} = \frac{R_{1,1} \times [X_2 - X_1] + R_{1,2} \times [Y_2 - Y_1] + R_{1,3} \times [Z_2 - Z_1]}{R_{3,1} \times [X_2 - X_1] + R_{3,2} \times [Y_2 - Y_1] + R_{3,3} \times [Z_2 - Z_1]}$$

and, 4.33

$$\frac{Y_B - Y_A}{Z_B - Z_A} = \frac{R_{2,1} \times [X_2 - X_1] + R_{2,2} \times [Y_2 - Y_1] + R_{2,3} \times [Z_2 - Z_1]}{R_{3,1} \times [X_2 - X_1] + R_{3,2} \times [Y_2 - Y_1] + R_{3,3} \times [Z_2 - Z_1]}$$

These two equations contribute to the determination of the rotation angles Ω , Φ , and K . The next equations to be derived are those that contribute to the determination of the scale factor and the translation vector. These equations are shown

below. For further explanation, please refer to Section 3.4.2 in the work by Ghanma, 2006.

Applying the same constraint to point '1' in Figure 4.15 yields Equation 4.33,

$$\begin{bmatrix} X_T \\ Y_T \\ Z_T \end{bmatrix} + S \times \begin{bmatrix} x_1 \\ x_1 \\ x_1 \end{bmatrix} = \begin{bmatrix} X_A \\ Y_A \\ Z_A \end{bmatrix} + \lambda_1 \times \begin{bmatrix} X_B - X_A \\ Y_B - Y_A \\ Z_B - Z_A \end{bmatrix} \quad 4.34$$

Where,

$$\begin{bmatrix} x_1 \\ y_1 \\ z_1 \end{bmatrix} = R \times \begin{bmatrix} X_1 \\ Y_1 \\ Z_1 \end{bmatrix}$$

Re-arranging the terms in the above equation, and dividing the first two rows by the third one to eliminate λ_1 , will yields Equations 4.35 and 4.36.

$$\frac{X_B - X_A}{Z_B - Z_A} = \frac{X_T + Sx_1 - X_A}{Z_B + Sz_1 - Z_A} \quad 4.35$$

$$\frac{Y_B - Y_A}{Z_B - Z_A} = \frac{Y_T + Sy_1 - Y_A}{Z_B + Sz_1 - Z_A} \quad 4.36$$

Applying the same derivation above for point '2' in Figure 4.15 gives the following equations,

$$\frac{X_B - X_A}{Z_B - Z_A} = \frac{X_T + Sx_2 - X_A}{Z_B + Sz_2 - Z_A} \quad 4.37$$

$$\frac{Y_B - Y_A}{Z_B - Z_A} = \frac{Y_T + Sy_2 - Y_A}{Z_B + Sz_2 - Z_A} \quad 4.38$$

Finally, dividing Equations 4.35 and 4.36 by Equations 4.37 and 4.38, respectively, and re-arranging the terms yields the following final equations,

$$\frac{X_T + Sx_1 - X_A}{Z_B + Sz_1 - Z_A} = \frac{X_T + Sx_2 - X_A}{Z_B + Sz_2 - Z_A} \quad 4.39$$

and,

$$\frac{Y_T + Sy_1 - Y_A}{Z_B + Sz_1 - Z_A} = \frac{Y_T + Sy_2 - Y_A}{Z_B + Sz_2 - Z_A} \quad 4.40$$

A minimum of two non-coplanar line pairs are needed to recover the three translations, three rotations and scale factor.

The endpoint and line constraint methods are expected to yield similar results. The endpoint method looks easier to derive and to apply since we are still using the traditional point-based least squares solution; however, this is an insignificant difference. The minimum requirements for both methods are the same (two non-coplanar lines). Therefore, the conclusions made are that both methods give similar results and that they have the same load in terms of processing time.

4.5 LiDAR Quality Control Using Iterative Closest Patch (ICPatch)

So far, all the above quality control methods require some form of pre-processing of the raw data (i.e. generating range and intensity images, segmentation, plane intersection). Hencke, other methods of quality control might be developed while using the original point cloud, or at least methods that requires minimal pre processing of the original data.

The ICPatch method does not assume point to point correspondence; it assumes a point to patch relationship. Consider two LiDAR strips; the first strip is provided in TIN (Triangulated Irregular Network) form, and the second strip is given as a cloud of points.

For a given area, consider that the two datasets represent the same physical surface, but with different point distribution. Figure 4.16 presents the point to patch correspondence.

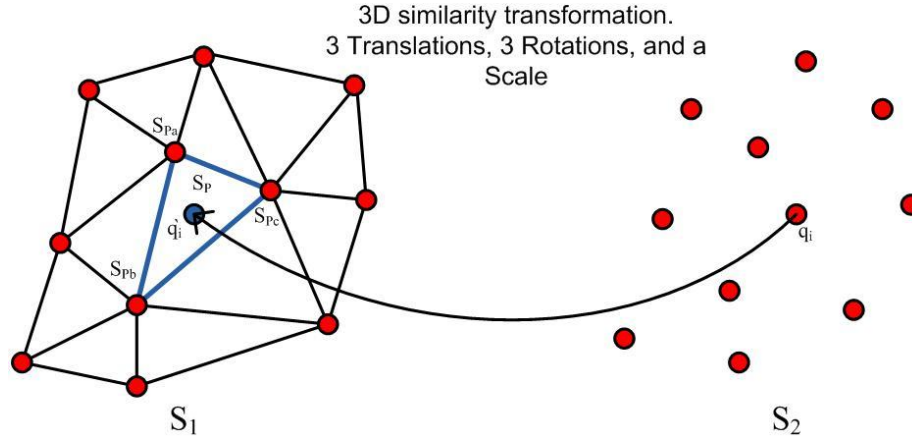


Figure 4.16: Point to patch correspondence using the ICPatch method

If we are to transform the points in S_2 to S_1 , the point q_i will be represented as \hat{q}_i in S_1 .

The transformation function is the 3D conformal function shown below:

$$\begin{bmatrix} X_{\hat{q}_i} \\ Y_{\hat{q}_i} \\ Z_{\hat{q}_i} \end{bmatrix} = \begin{bmatrix} X_T \\ Y_T \\ Z_T \end{bmatrix} + S \times R_{\Omega, \Phi, K} \times \begin{bmatrix} X_{q_i} \\ Y_{q_i} \\ Z_{q_i} \end{bmatrix} \quad 4.41$$

Theoretically, if both surfaces are representing the same object perfectly, the point \hat{q}_i should belong to the triangle S_{Pa}, S_{Pb}, S_{Pc} . In other words, the normal distance from \hat{q}_i to the triangular surface should be zero. This is the constraint that is used in this method, for which a mathematical representation of the constraint is shown Equation 4.42. Please refer to Cheng, 2006 for further details.

$$\begin{vmatrix} X_{\hat{q}_i} & Y_{\hat{q}_i} & Z_{\hat{q}_i} & 1 \\ X_{Pa} & Y_{Pa} & Z_{Pa} & 1 \\ X_{Pb} & Y_{Pb} & Z_{Pb} & 1 \\ X_{Pc} & Y_{Pc} & Z_{Pc} & 1 \end{vmatrix} = 0 \quad 4.42$$

The final task to be done, before running a least squares solution, is to establish the correspondence between the patches in the first strip and the points in the second strip. In other words, it is necessary to determine which points in strip 2 belong to which patches in strip 1. To accomplish this, two conditions are set, after transforming the second surface to the first one using the initial approximations of the transformation parameters. First, we should find the patch with the shortest normal distance to the selected point, and second, the projection of that point onto the triangle should be located within the triangle. The volume of the tetrahedron shown in Figure 4.17 is minimized in the least squares solution, which is repeated until the estimated parameters do not change. Not all of the points and patches are expected to have a match; examples of non-matching points and patches are shown in Figure 4.18. It worth mentioning also that this method requires many more iterations than previous methods to converge to the right parameters; this will not be considered a disadvantage, however, as even with this huge number of iterations, the time spent is still reasonable.

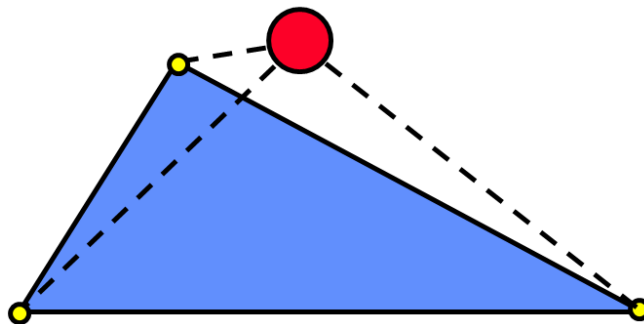


Figure 4.17: Volume generated by the triangle corners from the first strip and the red point from the second strip

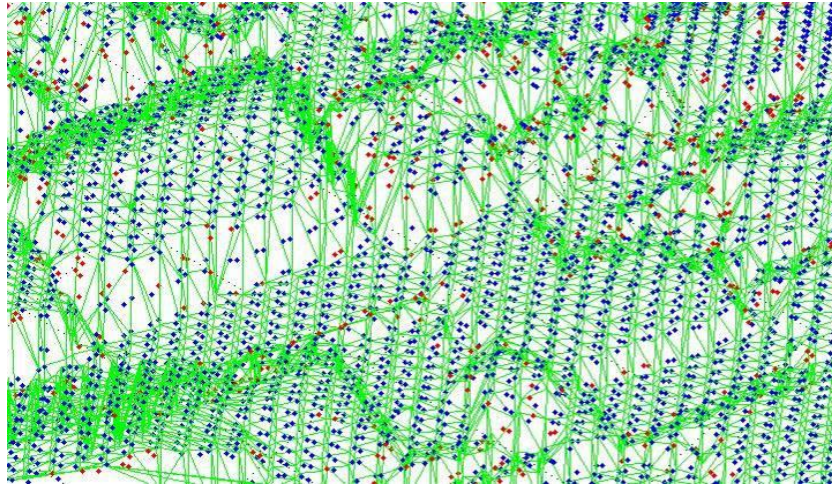


Figure 4.18: Non-matched points (red color) and matched points (blue color) with the TIN generated from another strip in the overlapping area.

When dealing with a huge amount of bias or when trying to calculate the transformation parameters between two different surfaces, good estimates of the 3D similarity transformation parameters are required. For further explanation of how to accomplish this, please refer to Habib, et al., 2001, and Habib, et al., 2006.

4.6 LiDAR Quality Control Using Iterative Closest Point (ICPoint)

This is a very simple method that can be used to roughly detect biases and errors. The procedure for this method requires only that the second surface be transformed to the first surface using the initial approximations of the transformation parameters. Then, for each point in the second surface, the closest point in the first surface is found and the points are then assumed to be conjugate (Zhang, 1994), although there is no point to point correspondence in overlapping LiDAR strips. This method is considered to be approximate, and it has issues with reliability. It is not recommended to use this method alone or to trust the results, due to the assumptions made.

In the least squares solution, the distances between the matched points are minimized; in the second iteration, new matches are searched for and the distances are minimized again. This procedure is repeated until no significant changes occur in the estimated transformation parameters.

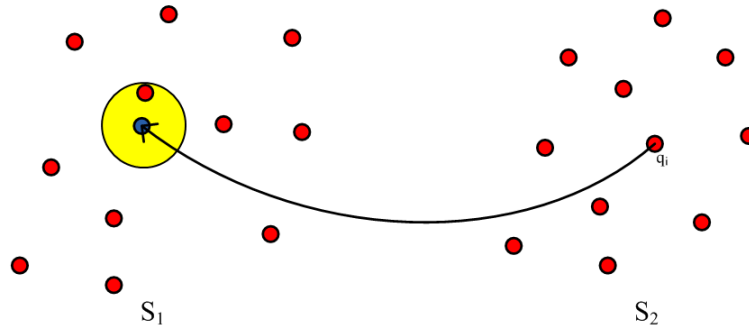


Figure 4.19: Point to point correspondence using the ICPoint method.

4.7 Summary

In summary, five methodologies were discussed, three of which are recommended to be used (using lines, using patches (point based), and IC Patches). The other two methods could be used, but the resulting estimated parameters will be infected by other sources of errors (interpolation effects in the range and intensity method, and inaccurate assumptions for the ICPoint method). In the next chapter, an evaluation of these five methods is carried out using real datasets.

Chapter Five: **Experimental Results**

5.1 Introduction

In Chapter four, five approaches for LiDAR quality control were discussed. The first approach was to perform quality control using range and intensity images. Then, the patches method was explained, after which two approaches using the lines method were outlined. Finally, the iterative closest patch method was explained, as well as the iterative closest point method. In this chapter, these methods will be tested using real data provided by two different sensors covering different areas. This chapter starts with an overview of the developed software, followed by a quick description of the sensors and datasets used. Then, the results from the first dataset will be shown and discussed, followed by the results and discussion of the second dataset.

5.2 User Interface Overview (LiDAR_QC)

When this research began, the algorithms and tools necessary to carry out quality control procedures were available in separate software packages. Running these programs separately was time-consuming, as one has to jump between different programs and define input and output for each piece of software. The idea of the LiDAR_QC program evolved for two reasons: first, to have an easy-to-use interface that groups the quality control methods used side by side with the data pre-processing tools, and second, to speed up the process of performing quality control.

Usually, quality control is expected to be fast and accurate. However, due to the large amount of data (LiDAR data) that comes out of a single mission, the process of quality control should be planned carefully, with the highest degree of optimization. That was the target when the development of this interface began. This program (LiDAR_QC) is capable of preparing the required features (points, lines, patches, and TIN surfaces) for the purpose of quality control. It is also able to perform quality control using intensity and range images, lines, and patches. Figure 5.1 shows an example of an extracted area (left) and the same area after applying the segmentation algorithm. Figure 5.2 (left) visualizes the extracted lines in a certain area; the right figure shows the generated TIN for the same area.

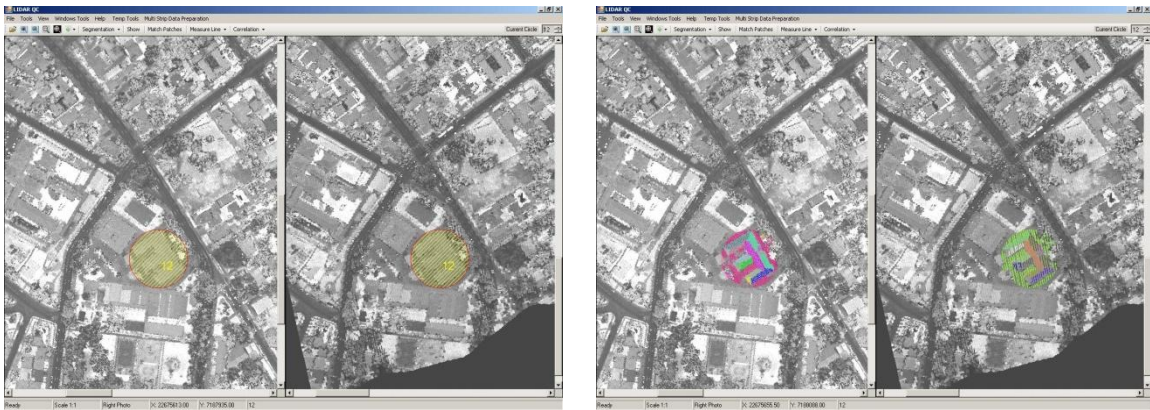


Figure 5.1: Selecting an area (left), then performing the segmentation procedure (right).

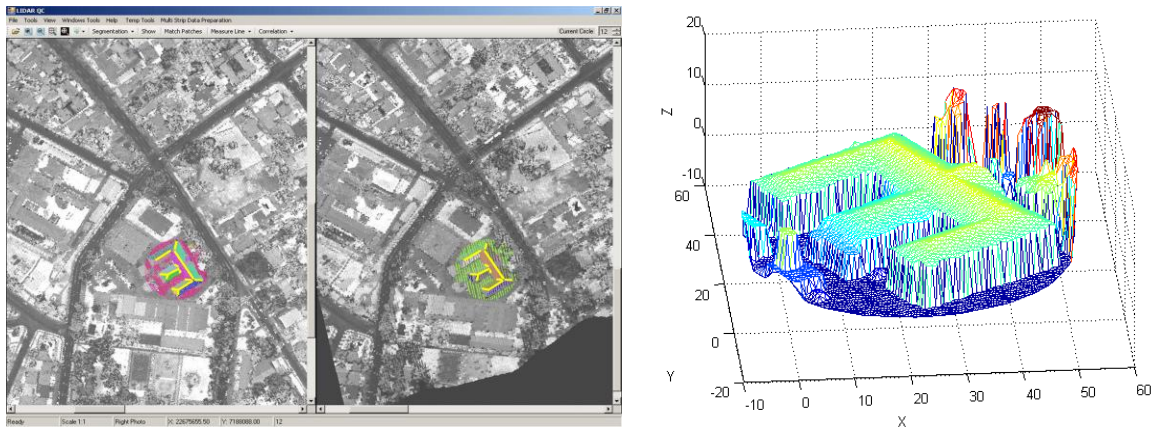


Figure 5.2: Generating linear features (left) and generating a TIN for an area (right)

5.3 Sensors and Data Overview

Table 5-1 summarizes the metadata for the datasets used. The first dataset was provided by LACTEC, and the second dataset was provided by the University of Calgary IT Center.

For the first dataset, the following quality control methods were used:

1. Intensity and Range Image Method
2. Line (Point Based and Line constraint) Methods
3. Patch Method
4. ICPatch Method
5. ICPoint Method

For the second dataset, the following quality control methods were used:

1. Line (Point Based and Line constraint) Methods
2. Patch Method
3. ICPatch Method
4. ICPoint Method

Table 5-1: Summary of the datasets used

	Dataset 1	Dataset 2
Data Provider	LACTEC	UofC IT Center
Survey Location	Brazil	UofC
Sensor Model	ALTM 2050	ALTM 3100
Scanner Type	Linear	Linear
Flying Height (m)	~1000	~1200
Pulse Rate (kHz)	50	50
Ground Point Spacing (m)	~0.70	~0.75
Reported Vertical Accuracy (cm)	15	9
Reported Horizontal Accuracy (cm)	50	50
Overlap Percentage (%)	~75	~50
Number of Strips	3	11
Number of Pairs	3	10

5.4 The First Dataset: QC Results

Figure 5.3 shows the intensity images generated from the first dataset, with an aeroplane symbol that represents the flying direction. The second and fourth strips were observed from the same flying direction, while the third strip was collected from the opposite flying direction. The intensity images were generated using commercial software; the pixel size was set to be 0.50 meters since the average point spacing is around 0.70 meters. These strips have a triple overlap that yields three pairs.

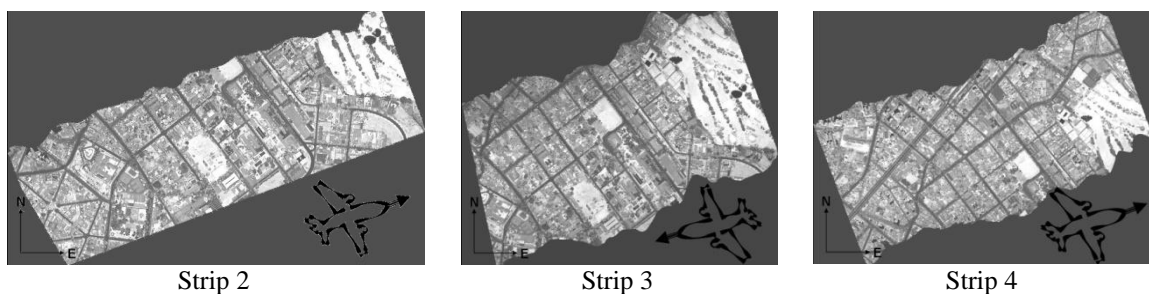


Figure 5.3: Intensity images generated from the first dataset with the flying directions shown.

5.4.1 Intensity and Range Image Method

In this method, one hundred conjugate points were collected from strips three and four, then the differences between them in all directions were calculated. Table 5-2 summarizes the resulting average distances and their standard deviations; for detailed measurements, please refer to Appendix B.

Table 5-2: The averages and standard deviations of the estimated discrepancies between overlapping strips, using 100 points

	Average (m)	Standard deviation (m)
X	0.33	0.54
Y	0.38	0.59
Z	0.12	0.42

Figure 5.4 shows a sample of the measured points; note how hard it is to find conjugate features in the intensity images due to the poor detail (more samples are shown in Appendix B).

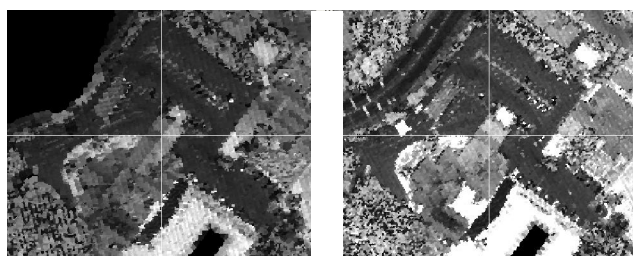


Figure 5.4: A sample of conjugate points identified in overlapping strips.

The following histograms show the difference distributions in the X, Y, and Z directions. Note that this method may produce blunders even if the operator is very careful in identifying conjugate features. Usually, identifiable features in urban areas are located at the break lines, where the major interpolation artefacts occur. Also, changes in the laser signal reflectance between overlapping strips will disturb the cross correlation

best match results; note how this affects the variance of the measurements in the Z direction.

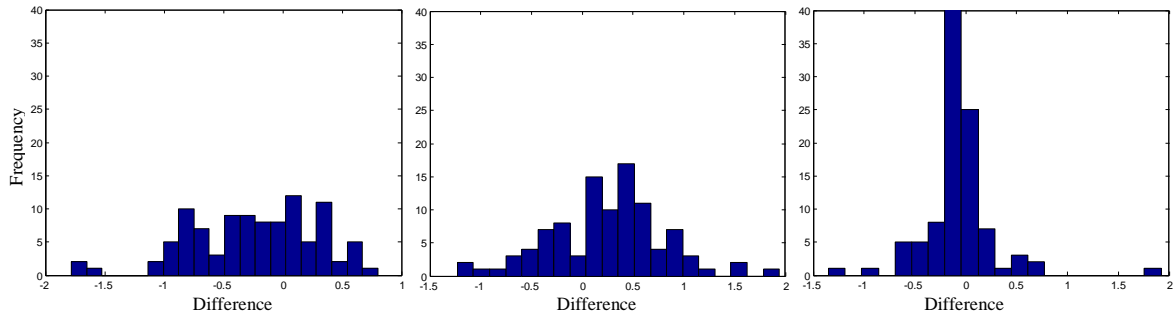


Figure 5.5: Histograms for the differences in the X,Y, and Z directions (left to right)

5.4.2 Line (Point Based and Line Constraint) Methods

For this method, two tests were performed. The first one was done to compare the results of the point based method to those of the line constraint method. Table 5-3 shows the resulting estimated transformation parameters using the above methods for strips 3 and 4. Note how the results are very similar. Also note how the average normal distance changes after applying the transformation. This indicates that this method was successful in detecting and removing biases. However, the variances of the normal distances did not change. That is because the nature of the rigid body transformation (3D similarity transformation) maintains the relationships between the points (the internal angles between the points do not change).

Table 5-3: Estimated transformation parameters using conjugate linear features in overlapping strips, together with the normal distances between the linear features before and after applying the transformation.

	Line-Constraint Approach	Line-Endpoint Approach
Scale Factor	1.0006	0.9998
X_T (m)	0.75	0.77
Y_T (m)	-0.17	-0.17
Z_T (m)	0.05	0.06
Ω (°)	-0.0386	-0.0421
Φ (°)	-0.0125	-0.0048
K (°)	-0.0145	-0.0134
Normal Distance (m) (Before)	0.49 ± 0.24	0.49 ± 0.24
Normal Distance (m) (After)	0.18 ± 0.18	0.18 ± 0.19

In the second test, lines were measured in the three pairs using the LiDAR_QC software, and the line constraint method was run to evaluate the internal quality of the strips. Table 5-4 shows the resulting estimated transformation parameters between the strips. Figure 5.6 shows a sample of the linear features used before and after applying the estimated transformation parameters. In the ideal case (when no biases exist) the transformation parameters should be one for the scale and zeros for the translation and rotation parameters. It is clear that biases exist in this dataset. Note also how the estimated bias in the X direction is dependent on the flying direction (the bias is estimated to be very small in strips 2 and 4, and this changes when dealing with different flying directions).

Table 5-4: Transformation parameters estimated using conjugate linear features in overlapping strips, together with the normal distances between the linear features before and after applying the transformation.

	Strips 2 & 3	Strips 3 & 4	Strips 2 & 4
Transformation Parameter / # of Lines	24	36	24
Scale Factor	1.0002	1.0006	1.0013
X_T (m)	-0.56	0.75	0.10
Y_T (m)	0.04	-0.17	-0.16
Z_T (m)	0.03	0.05	0.13
Ω (°)	0.0205	-0.0386	-0.0147
Φ (°)	0.0062	-0.0125	-0.0073
K (°)	0.0261	-0.0145	-0.0113
Normal Distance (m) (Before)	0.38 ± 0.22	0.49 ± 0.24	0.26 ± 0.14

Normal Distance (m) (After)	0.18 ± 0.19	0.18 ± 0.18	0.16 ± 0.11
-----------------------------	-----------------	-----------------	-----------------

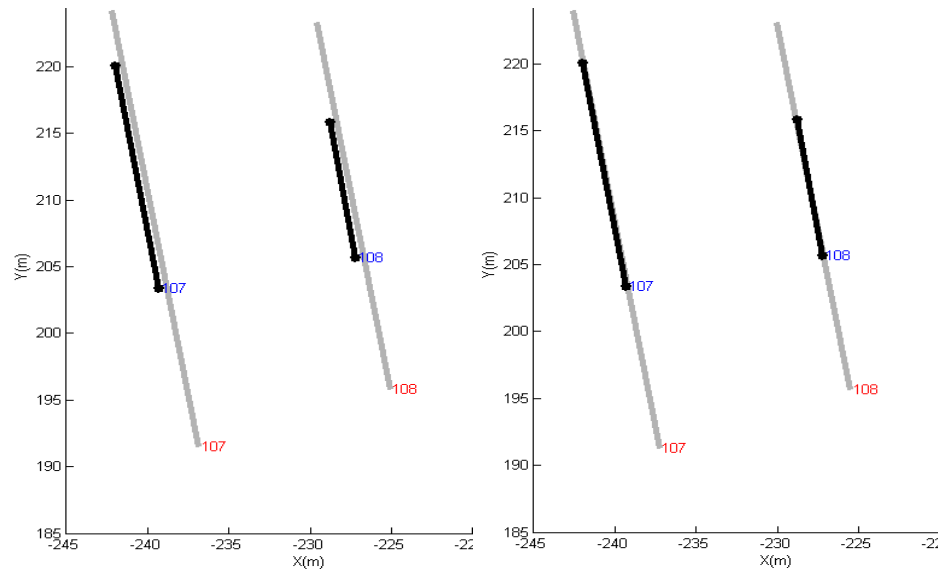


Figure 5.6: Comparison of conjugate linear features before LIDAR system bias removal (left) and after bias removal (right)

5.4.3 Patch Method

In this method, planar patches were collected from the three strips using the LiDAR_QC software. The resulting estimated transformation parameters are shown in Table 5-5. Note that the results are very consistent with the parameters estimated using the line methods in Table 5-3 and Table 5-4.

Table 5-5: Transformation parameters estimated using conjugate planar in overlapping strips.

	Strips 2 & 3	Strip 3&4	Strips 2 & 4
Transformation Parameter / # of Patches	21	22	22
Scale Factor	1.0000	0.9996	0.9995
X_T (m)	-0.52	0.72	0.08
Y_T (m)	-0.13	-0.17	-0.21
Z_T (m)	0.05	0.09	0.14
Ω (°)	0.0289	-0.0561	-0.0802
Φ (°)	0.0111	-0.0139	-0.0342
K (°)	0.0364	0.0288	0.0784
Normal Distance (m) (After)	0.04	0.03	0.04

5.4.4 Iterative Closest Patch Method

Two main objectives were met with this experiment. The first was to compare this method with the line and patch methods. The second objective was to use different areas with different point distributions to determine the significance of the sample distribution on the estimated parameters.

Table 5-6 shows the transformation parameters estimated using automated matching of conjugate surface elements in strips 3 and 4, and using one, three, and seven selected areas. Figure 5.7 shows the locations of the selected areas for the registration and automated matching of conjugate surface elements in two overlapping strips. Figure 5.8 shows an example of one of the extracted circles (circle three in Figure 5.7). Note that the results that are most similar to those of the methods in the previous sections were obtained when using seven areas. However, the results coming from the use of one and three areas are still fairly similar.

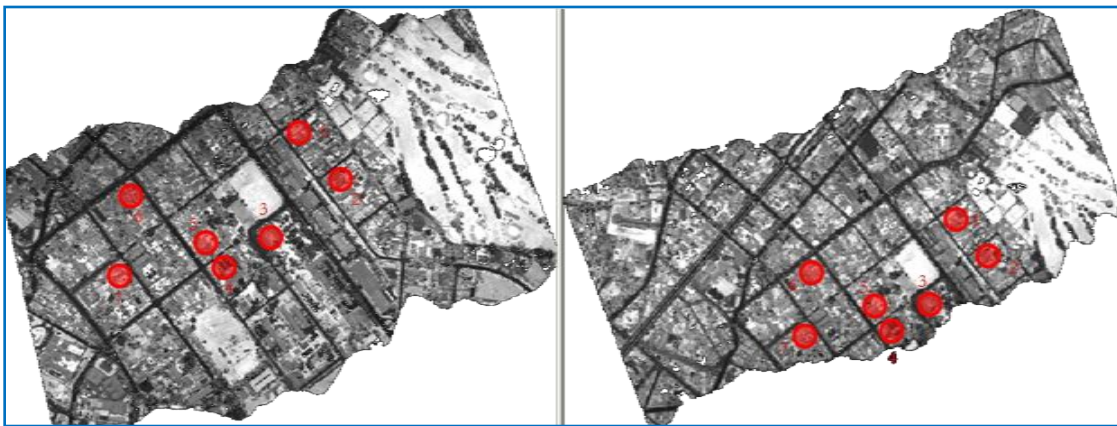


Figure 5.7: Locations of selected areas for the registration and automated matching of conjugate surface elements in two overlapping strips.

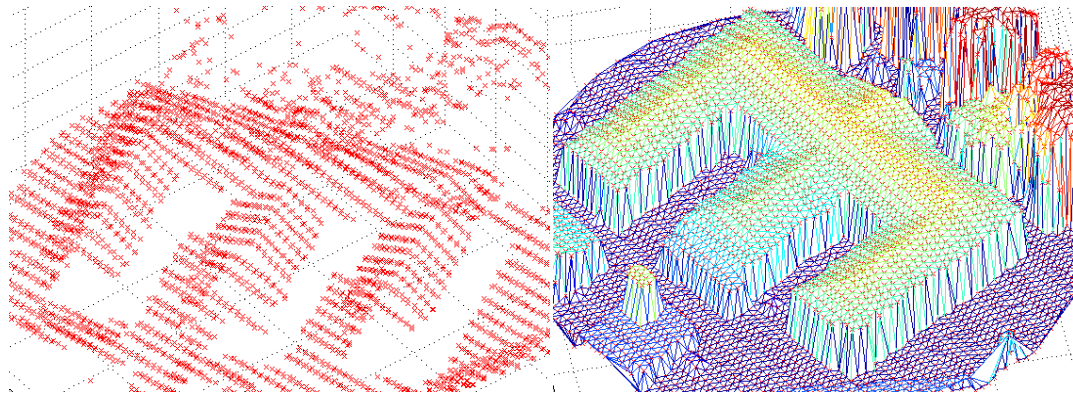


Figure 5.8 A sample of the extracted points in two strips (left); TINs were generated from the second strip point cloud (right).

Table 5-6: Transformation parameters estimated using automated matching of conjugate surface elements in strips 3 and 4.

	One Building (1)	Three Building Areas (1,2,3)	Seven Building Areas
Scale Factor	0.9997	0.9998	0.9998
X_T (m)	0.85	0.56	0.75
Y_T (m)	-0.07	-0.26	-0.13
Z_T (m)	0.15	0.09	0.12
Ω ($^\circ$)	-0.0218	-0.0200	-0.0267
Φ ($^\circ$)	-0.0201	-0.0034	-0.0088
K ($^\circ$)	0.1239	-0.0189	-0.0003
Average Normal Distance (m) (after adjustment)	0.10	0.09	0.09

In the second test, circles were extracted from the three pairs (Figure 5.3) using the LiDAR_QC software, and the ICPatch method was run to evaluate the internal quality of the strips. Table 5-7 shows the resulting estimated transformation parameters between the strips

Table 5-7: Transformation parameters estimated using the ICPatch method in three strips.

	Strips 2& 3	Strips 3& 4	Strips 2& 4
Scale Factor	0.9996	0.9998	0.9993
X_T (m)	-0.55	0.75	0.19
Y_T (m)	-0.06	-0.13	-0.18
Z_T (m)	0.03	0.12	0.16
Ω (°)	0.0080	-0.0267	-0.0213
Φ (°)	0.0059	-0.0088	-0.0053
K (°)	-0.0009	-0.0003	0.0012
Average Normal Distance (m) (after adjustment)	0.09	0.09	0.10

5.4.5 ICPoint Method

For the ICPoint method, the resulting estimated parameters are shown in Table 5-8. Note how the results are deviating from those of the patch, line, and the ICPatch methods. As mentioned in Chapter 4, this method is considered to be an approximate one, and it has issues with reliability. It is not recommended to use this method alone or to trust the results, due to the inaccurate assumptions made. However, sometimes this method gives reasonable results, as we will see with the second dataset.

Table 5-8: Transformation parameters estimated using the ICPoint method, between overlapping strips.

	Strips 2&3	Strips 3&4	Strips 2&4
Scale Factor	0.9997	1.0002	0.9994
X_T (m)	-0.47	0.70	0.26
Y_T (m)	-0.27	-0.32	-0.41
Z_T (m)	0.00	0.04	0.15
Ω (°)	0.0132	-0.0394	-0.0302
Φ (°)	0.0082	-0.0141	-0.0059
K (°)	0.0039	-0.0007	-0.0100
Average Distance (m)	0.51	0.51	0.60

5.5 The Second Dataset: QC Results

For this dataset, the lines, patches, ICPatch and ICPPoint quality control methods were applied to all datasets, except for two pairs (5 and 10) due to a lack of linear features and planar patches. The intensity and range image method was not used here due to the confident conclusion that it is not suitable for the quality control of LiDAR data. This dataset was collected in two different flight missions; the first three digits of the intensity image name indicate the Julian day, and the flying directions (FD) of the strips are indicated in the figure headings.

1. Pair 1: Strips 08803 and 08804

For the pair shown in Figure 5.9, the resulting transformation parameters are shown in Table 5-9. The transformation parameter values indicate that conjugate surface elements in this pair are coinciding with one another nicely. The reported transformation parameters are close to the expected values in the absence of biases. In Figure 5.9, the yellow circles indicate areas extracted for the ICPatch and ICPPoint methods, while the red circles were used for the extraction of planar patches and linear features. The average normal distances shown in Table 5-9 were computed after applying the transformation parameters. Note the large average distance value resulting from the ICPPoint method. In this case, the number indicates roughly the average point spacing only. Notice the consistency of the reported parameters from different methods in Table 5-9.

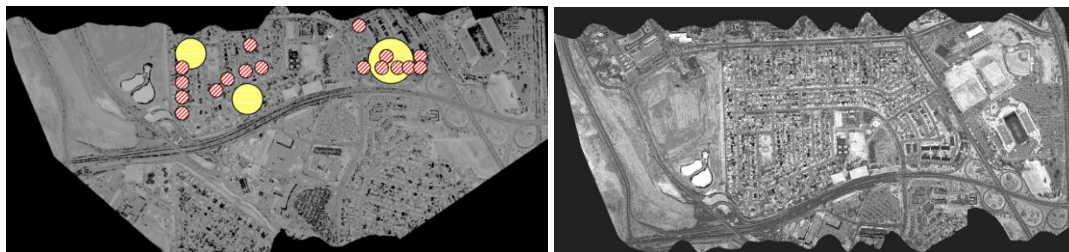


Figure 5.9: Strips 08803 (FD W→E) and 08804 (FD E→W)

Table 5-9: Estimated transformation parameters between Strip 08803 and Strip 08804 using four methods.

Method		Estimated Transformation Parameters							Av_Dist (m)	
		S	XT (m)	YT (m)	ZT (m)	Omega (deg)	Phi (deg)	Kappa (deg)		
08803 & 08804	Patch Method	1.00019	-0.02	-0.02	0.02	-0.0151	0.0023	0.0052	0.03	
	Line	Collinearity	1.00009	0.04	-0.08	0.02	-0.0132	0.0020	0.0039	0.10
		Endpoint	0.99995	0.02	-0.02	0.01	-0.0084	-0.0003	0.0068	0.08
	ICPatch	0.99990	-0.01	-0.12	0.01	-0.0023	-0.0009	0.0029	0.04	
	ICPoint	0.99980	-0.08	-0.27	0.00	-0.0036	-0.0011	0.0022	0.51	

2. Pair 2: Strips 08804 and 08805

For the pair shown in Figure 5.10, the resulting transformation parameters are shown in Table 5-10. The transformation parameter values indicate that this data pair is suffering from a bias in the X direction. Although this pair was collected from the same mission from which pair 1 was collected, biases appeared in this pair. Note how the results from the various methods are consistent.

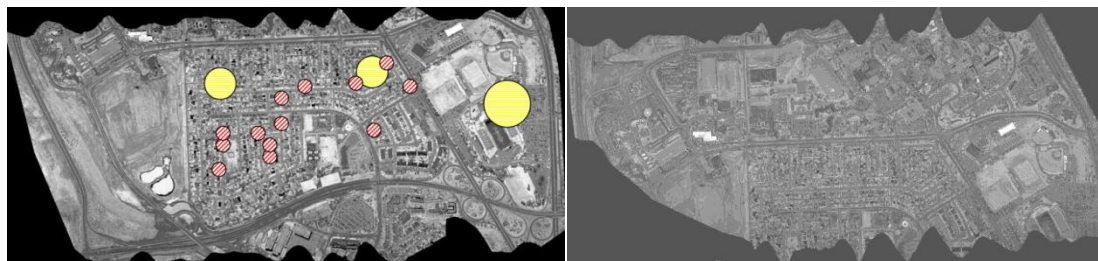


Figure 5.10: Strips 08804 (FD E→W) and 08805 (FD W→E)

Table 5-10: Estimated transformation parameters between Strip 08804 and Strip 08805.

Method		Estimated Transformation Parameters							Av_Dist (m)	
		S	XT (m)	YT (m)	ZT (m)	Omega (deg)	Phi (deg)	Kappa (deg)		
08804 & 08805	Patch Method	1.00003	0.76	0.14	-0.01	0.0185	0.0060	0.0175	0.03	
	Line	Collinearity	1.00037	0.80	0.10	-0.03	0.0156	0.0022	-0.0011	0.15
		Endpoint	0.99987	0.80	0.25	-0.02	0.0164	0.0054	0.0270	0.13
	ICPatch	1.00010	0.86	0.10	-0.02	0.0039	0.0006	0.0073	0.04	
	ICPoint	1.00000	0.80	-0.08	-0.04	0.0089	0.0004	0.0080	0.57	

3. Pair 3: Strips 08804 and 13030

For the pair shown in Figure 5.11, the resulting transformation parameters are shown in Table 5-11. The transformation parameter values indicate that this data pair is suffering from a bias in the X direction. This pair showed a similar bias to the one in pair 2 in terms of direction. Note that this data pair is coming from two different missions.

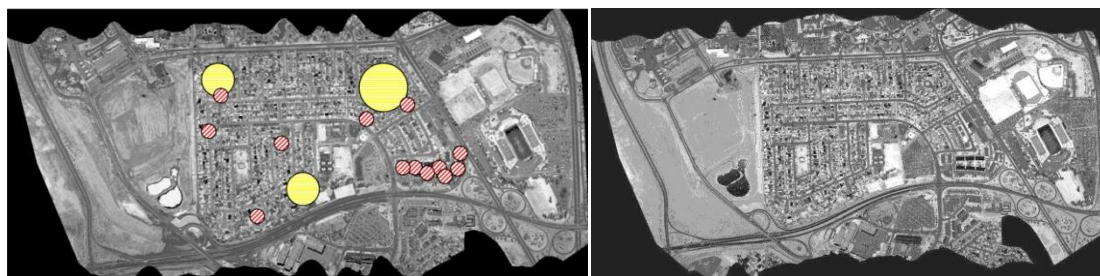


Figure 5.11: Strips 08804 (FD E→W) and 13030 (FD E→W)

Table 5-11: Estimated transformation parameters between Strip 08804 and Strip 13030 using four methods.

Method		Estimated Transformation Parameters							Av_Dist (m)	
		S	XT (m)	YT (m)	ZT (m)	Omega (deg)	Phi (deg)	Kappa (deg)		
08804 & 13030	Patch Method	0.99962	0.43	0.13	-0.06	0.0132	-0.0002	-0.0238	0.04	
	Line	Collinearity	0.99997	0.41	0.13	-0.05	0.0108	0.0005	-0.0106	0.15
		Endpoint	1.00002	0.37	0.18	-0.04	0.0131	-0.0021	-0.0083	0.15
	ICPatch	1.00010	0.47	0.21	0.00	0.0104	0.0019	0.0012	0.04	
	ICPoint	1.00000	0.44	0.19	0.00	0.0093	0.0019	-0.0014	0.57	

4. Pair 4: Strips 08805 and 08806

For the pair shown in Figure 5.12, the resulting transformation parameters are shown in Table 5-12. The transformation parameter values indicate that these datasets are nicely coinciding with one another. The reported transformation parameters are within the range of the system noise.

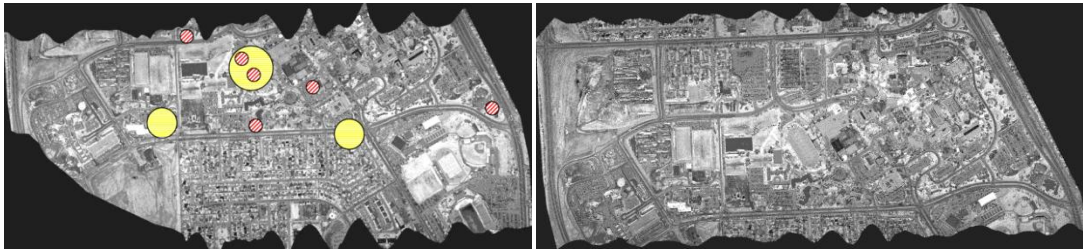


Figure 5.12: Strips 08805 (FD W→E) and 08806 (FD E→W)

Table 5-12: Estimated transformation parameters between Strip 08805 and Strip 08806 using four methods.

Method		Estimated Transformation Parameters							Av_Dist (m)	
		S	XT (m)	YT (m)	ZT (m)	Omega (deg)	Phi (deg)	Kappa (deg)		
08805 & 08806	Patch Method	1.00012	0.10	0.09	-0.02	-0.0225	0.0019	0.0064	0.02	
	Line	Collinearity	1.00014	0.08	0.00	-0.02	-0.0061	-0.0020	-0.0006	0.10
		Endpoint	1.00005	0.06	0.05	-0.02	-0.0241	0.0018	0.0073	0.09
	ICPatch	0.9999	0.07	-0.10	-0.01	-0.0101	-0.0010	0.0013	0.04	
	ICPoint	0.9999	0.02	-0.11	-0.01	-0.0097	-0.0014	-0.0051	0.52	

5. Pair 5: Strips 08806 and 08807

For the pair shown in Figure 5.13, the resulting transformation parameters are shown in Table 5-13. For this pair, it was very hard to find conjugate planar patches and linear features. Therefore, the ICPatch and the ICPoint methods were used to detect the presence of biases. These methods were successful in detecting biases in the X direction.

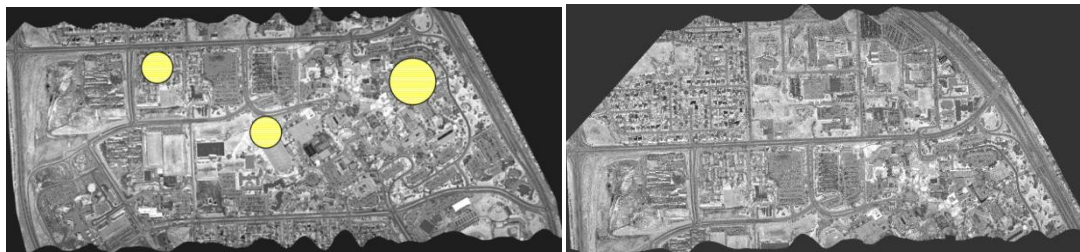


Figure 5.13: Strips 08806 (FD E→W) and 08807 (FD W→E)

Table 5-13: Estimated transformation parameters between Strip 08806 and Strip 08807 using two methods.

Method		Estimated Transformation Parameters							Av_Dist (m)
		S	XT (m)	YT (m)	ZT (m)	Omega (deg)	Phi (deg)	Kappa (deg)	
08806 & 08807	Patch Method	-	-	-	-	-	-	-	-
	Line	Collinearity	-	-	-	-	-	-	-
		Endpoint	-	-	-	-	-	-	-
	ICPatch	1.0000	0.85	0.04	0.06	0.0036	0.0008	-0.0038	0.04
	ICPoint	0.9999	0.78	-0.04	0.05	0.0013	0.0008	-0.0020	0.55

6. Pair 6: Strips 08806 and 13029

For the pair shown in Figure 5.14, the resulting transformation parameters are shown in Table 5-14. Once more, biases were detected along the X direction (flying direction).

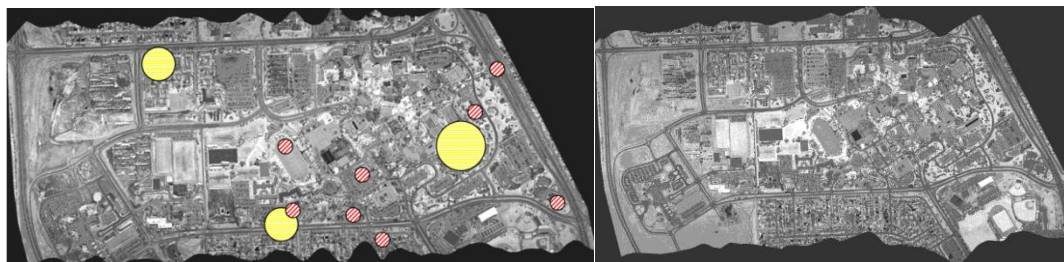


Figure 5.14: Strips 08806 (FD E→W) and 13029 (FD W→E)

Table 5-14: Estimated transformation parameters between Strip 08806 and Strip 13029 using four methods.

Method		Estimated Transformation Parameters							Av_Dist (m)	
		S	XT (m)	YT (m)	ZT (m)	Omega (deg)	Phi (deg)	Kappa (deg)		
08806 & 13029	Patch Method	1.00012	-0.32	-0.24	0.03	0.0140	-0.0032	-0.0124	0.03	
	Lines	Collinearity	1.00021	-0.30	-0.15	0.03	0.0017	-0.0013	0.0035	0.06
		Endpoint	1.00026	-0.27	-0.14	0.04	-0.0045	0.0015	0.0080	0.06
	ICPatch	0.9998	-0.29	0.03	0.01	0.0015	0.0001	-0.0126	0.04	
	ICPoint	0.9998	-0.17	0.01	0.00	0.0033	-0.0003	-0.0170	0.58	

7. Pair 7: Strips 08807 and 08808

For the pair shown in Figure 5.15, the resulting transformation parameters are shown in Table 5-15. The transformation parameter values indicate that these datasets are coinciding properly with one another. The reported transformation parameters indicate the absence of biases.

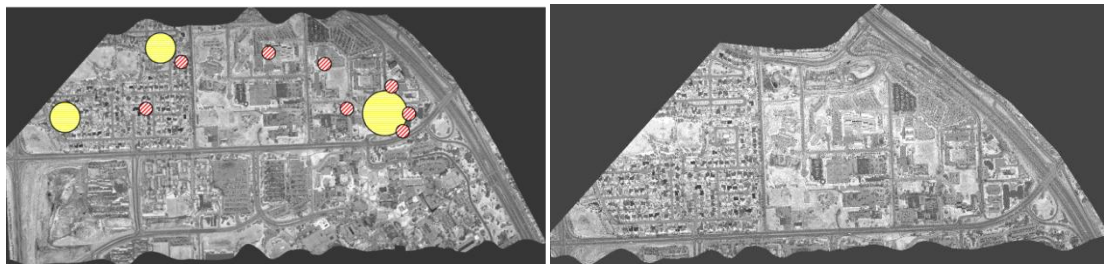


Figure 5.15: Strips 08807 (FD W→E) and 08808 (FD E→W)

Table 5-15: Estimated transformation parameters between Strip 08807 and Strip 08808 using four methods.

Method		Estimated Transformation Parameters							Av_Dist (m)	
		S	XT (m)	YT (m)	ZT (m)	Omega (deg)	Phi (deg)	Kappa (deg)		
08807 & 08808	Patch Method	1.00041	0.11	-0.08	-0.01	-0.0157	0.0015	-0.0033	0.01	
	Line	Collinearity	1.00079	0.18	-0.06	-0.02	-0.0120	0.0004	0.0040	0.09
		Endpoint	1.00183	0.21	-0.08	-0.02	-0.0352	0.0032	0.0071	0.13
	ICPatch	1.0000	0.16	-0.13	-0.02	-0.0114	-0.0000	-0.0034	0.04	
ICPoint	0.9999	0.10	-0.20	-0.02	-0.0138	0.0002	0.0064	0.52		

8. Pair 8: Strips 08807 and 13028

For the pair shown in Figure 5.16, the resulting transformation parameters are shown in Table 5-16. Again, biases were detected along the X direction (flying direction). Note how sometimes the ICPPoint method gives different results when compared to the other quality control methods; this is due to the inaccurate point-to-point relationship assumed.

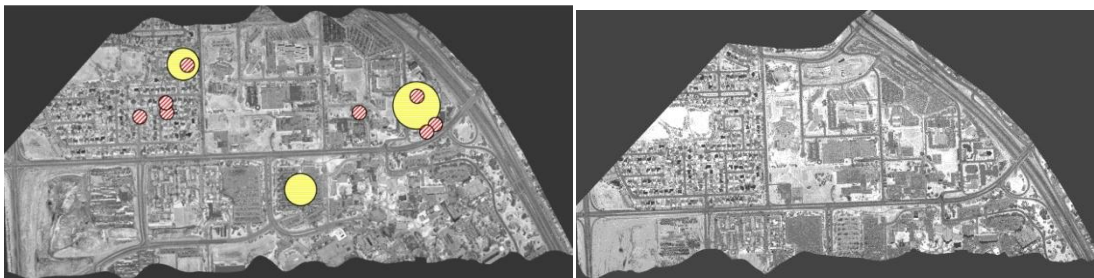


Figure 5.16: Strips 08807 (FD W→E) and 13028 (FD E→W)

Table 5-16: Estimated transformation parameters between Strip 08807 and Strip 13028 using four methods.

Method		Estimated Transformation Parameters							Av_Dist (m)	
		S	XT (m)	YT (m)	ZT (m)	Omega (deg)	Phi (deg)	Kappa (deg)		
08807 & 13028	Patch Method	1.00018	0.44	-0.03	-0.02	0.0021	-0.0029	-0.0056	0.02	
	Line	Collinearity	1.00023	0.51	0.01	-0.00	-0.0064	0.0131	0.0281	0.11
		Endpoint	1.00015	0.45	-0.00	-0.03	-0.0057	0.0239	-0.0400	0.09
	ICPatch	1.0001	0.46	-0.05	-0.01	-0.0109	0.0017	-0.0005	0.04	
	ICPoint	1.0000	0.33	-0.07	-0.04	-0.0053	0.0010	0.0004	0.56	

9. Pair 9: Strips 13027 and 13030

For the pair shown in Figure 5.17, the resulting transformation parameters are shown in Table 5-17. The transformation parameter values indicate a large bias in this pair along the X direction. When dealing with large biases similar to this one, it is useful

to relax the thresholds used for the automated matching of lines and patches. This can be done when having trouble extracting existing planar patches and lines.

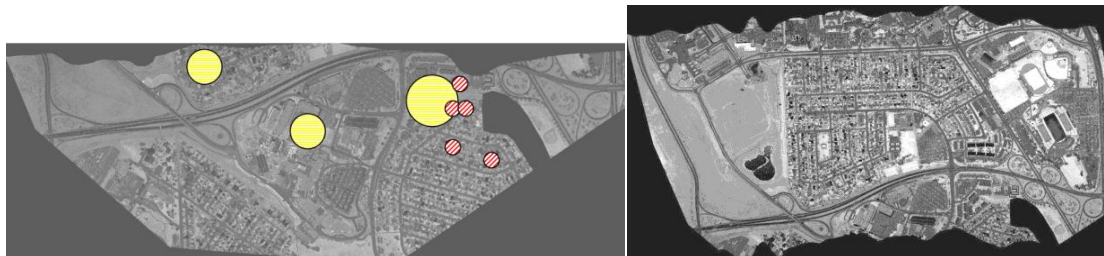


Figure 5.17: Strips 13027 (FD W→E) and 13030 (FD E→W)

Table 5-17: Estimated transformation parameters between Strip 13027 and Strip 13028 using four methods.

Method		Estimated Transformation Parameters							Av_Dist (m)	
		S	XT (m)	YT (m)	ZT (m)	Omega (deg)	Phi (deg)	Kappa (deg)		
13027 & 13030	Patch Method	1.00051	1.23	-0.39	-0.07	-0.0584	-0.0131	-0.0158		
	Line	Collinearity	1.0016	1.22	-0.35	-0.13	-0.0034	-0.0613	-0.1927	0.13713
		Endpoint	1.0020	1.19	-0.45	-0.10	-0.0258	-0.0118	-0.1038	0.09419
	ICPatch	1.0001	1.37	-0.43	-0.05	-0.0515	0.0004	-0.0050	0.04611	
	ICPoint	1.0005	1.42	-0.70	-0.05	-0.0523	-0.0006	-0.0139	0.58316	

10. Pair 10: Strips 13029 and 13030

For the pair shown in Figure 5.18, the resulting transformation parameters are shown in Table 5-18. The transformation parameter values indicate a large bias in this pair along the X direction, but with a different magnitude when compared to that of pair 9, although both pairs have the same flight configuration (same flying direction for the first and second strips).

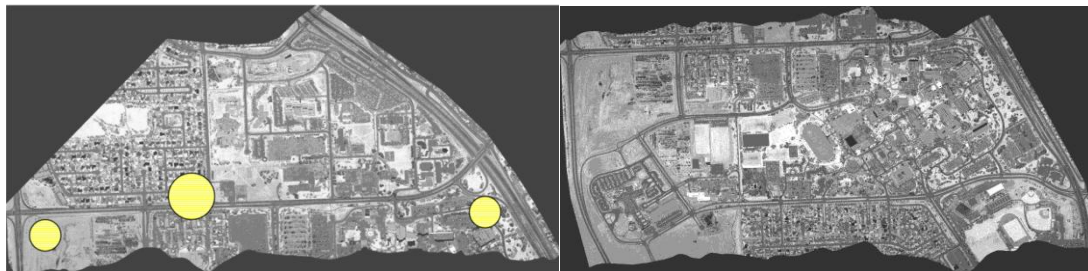


Figure 5.18: Strips 13029 (FD W→E) and 13030 (FD E→W)

Table 5-18: Estimated transformation parameters between Strip 13029 and Strip 13030 using four methods.

Method		Estimated Transformation Parameters								
		S	XT (m)	YT (m)	ZT (m)	Omega (deg)	Phi (deg)	Kappa (deg)	Av_Dist (m)	
13028 & 13029	Patch Method	-	-	-	-	-	-	-	-	
	Line	Collinearity	-	-	-	--	-	-	-	-
		Endpoint	-	-	-	-	-	-	-	-
	ICPatch	1.0002	-1.21	0.28	-0.00	0.0380	-0.0006	0.0026	0.04781	
	ICPoint	1.0002	-1.15	0.21	-0.00	0.0353	0.0000	0.0155	0.69023	

5.6 Conclusion

To conclude this chapter, it has been proven that the quality control methods discussed in this thesis are all capable of detecting biases in LiDAR data pairs (except for the intensity and range image method), with different degrees of confidence in the estimated transformation parameters. The line methods, patch method (point based method), and ICPatch method had high compatibility in their results.

As shown early in this chapter, using intensity and range images for quality control yields biased results. The ICPoint method gave results that were more consistent with the parameters estimated using the line, patch and ICPatch methods. However, the

results from the ICPpoint method cannot be fully trusted due to the inaccurate assumption of point-to-point correspondence in overlapping LiDAR data.

Chapter Six: **Conclusion**

6.1 Conclusion

LiDAR quality control is an important post-mission process used to verify the quality of the data produced. As mentioned in the introduction chapter, the main objectives of this research were to develop new methodologies and tools for LiDAR quality control. After the quick introduction to LiDAR and the literature review in Chapter 2, the errors associated with LiDAR systems were discussed in Chapter 3. Chapter 4 discussed the suggested quality control methods and their implementation. In Chapter 5, experiments were done and the results were discussed for the verification of the quality of the suggested methods.

In Chapter 3, it was concluded that different LiDAR system biases have different effects on the reconstructed surfaces; some of them are dependent on the flight direction, while others are independent of the flying direction. Biases might affect the accuracy in a certain direction, or in some cases, can act in more than one direction. In addition, these biases vary in terms of their dependency on the look angle and on the flying height. From such information, an indication of the source of each bias may be derived. For example, the behavior of the boresighting offset bias is independent of the flying height and the laser unit look angle, but dependent on the flying direction, for the planimetric coordinates. On the other hand, the effects of the boresighting angular bias are proportional to the flying height, and dependent on the flying direction and the look angle. In the same manner, noise in LiDAR systems can be analyzed. For example, the

impact of the positioning noise in the integrated GNSS/IMU unit is independent of the flying height and of the laser scanner look angle.

In Chapter 4, five categories of methodologies were discussed, among which four were recommended. The first methodology suggests using conjugate linear features from overlapping LiDAR strips as a measure of the data quality; the conceptual basis of this method is that conjugate linear features from different strips should overlap in the absence of biases. The second method uses planar patches; conjugate patches in overlapping strips should be coplanar in the ideal case (absence of biases). The third method is called the ICPatch method and uses a Triangulated Irregular Network generated from raw LiDAR data; it assumes a point-to-patch correspondence. Finally, the ICPPoint method, which assumes a point-to-point correspondence and does not require any pre-processing, is discussed. The range and intensity image method is not recommended due to the inconsistency in the results when compared with those of the first four methods. In this chapter, a user-friendly interface was also developed in Microsoft Visual C#, to prepare the required data and to perform the procedures for the aforementioned quality control methods.

The fusion of the aforementioned methods in single software will yield a practical quality control bundle that has many options. Also, it will give the capability to perform quality control checks in various areas (urban areas, rural areas.. etc). For example, urban areas are usually rich of linear features and planar patches, therefore the lines and patches methods could be used. On the other hand, line and patches cannot

usually be found in rural areas, but still, the terrain variation will make it possible for the ICPatch and ICPPoint methods to work. Even on places that has no features or terrain variation (e.g., airport runway), one could still evaluate part of the transformation parameters (Z shift, pitch and roll angles). Moreover, if biases exist in the undetermined parameters will not have any impact on the available surfaces (e.g., horizontal biases still lead to the same surface).

It has been proven, in Chapter 5, that the quality control methods discussed in this thesis (except for the intensity and range image method) are all capable of detecting biases in LiDAR data pairs, with differing degrees of confidence in the estimated transformation parameters. The line methods, patch method (point based method), and ICPatch method had highly compatible results. As shown early in this thesis, using intensity and range images for quality control yields inconsistent results. The ICPPoint method gave results that were more consistent with the parameters estimated using the line, patch and ICPatch methods. However, the results of the ICPPoint method cannot be fully trusted due to the inaccurate assumption of point-to-point correspondence in overlapping LiDAR data. The following table summarizes the various methods in terms of the required pre-processing, the time efficiency, and the reliability of the results, based on the experience gained from this research. Note that more stars indicate a better rank.

Table 6-1: Qualitative Evaluation of Quality Control methods

Method	Preprocessing	Time Efficiency	Reliability
Lines Constraint	★★	★★★	★★★★★★
Lines End Point	★★	★★★	★★★★★★
Patches Method	★★★	★★★★	★★★★★★
ICPatch	★★★★	★★★★	★★★★★★
ICPoint	★★★★★★	★★★★★★	★★★
Range and Intensity	★★★	★★★	★★

It has been mentioned that the purpose of this research is not to model biases; the target here is to detect biases. Therefore, the 3D similarity transformation was suggested as a mathematical model. However, experiments proved that it is possible to use the 3D similarity transformation in the relative adjustment of LiDAR strips; the following figure shows an example of the adjustment of LiDAR strips based on the parameters estimated using the quality control methods.

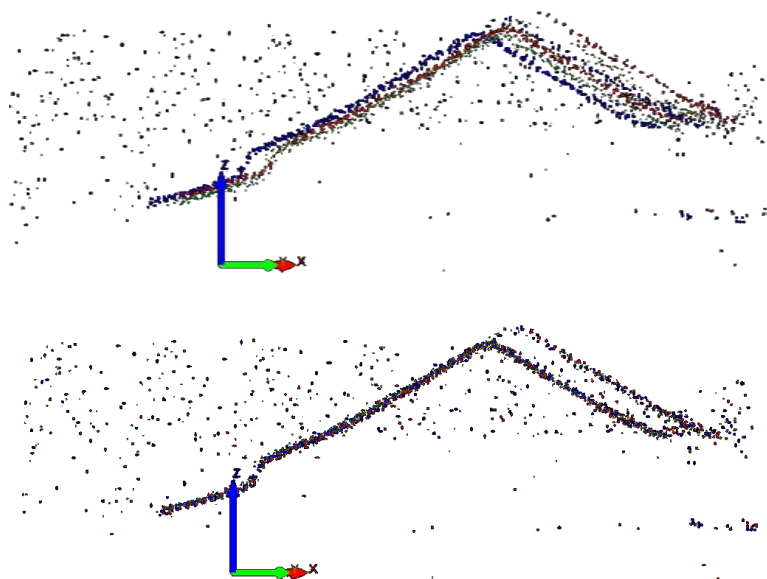


Figure 6.1: LiDAR point clouds for two buildings before (top) and after (bottom) the adjustment, note that each color indicates a different strip.

6.2 Recommended Future Work

Although the quality control methods suggested in this thesis have been carefully investigated and tested using multiple datasets, more testing is still required in order to ensure the reliability and practicality of these methods. These tests must also be performed by other researchers in order to gain neutral judgment regarding the sequence of the suggested workflow, and to generate ideas for potential enhancements that will act towards improving the performance of our program. It is also highly recommended to offer this product to industry in order to get feedback regarding the possibility of standardizing this software for commercial use.

More potential future work would be to relate the biases detected through the quality control procedures with their sources. This will have a positive impact on the processes of quality assurance and system calibration. Currently, the end user does not have access to the raw measurements from LiDAR systems, which has a negative impact on the understanding of LiDAR systems and, as a result, on the process of quality assurance.

A guideline is needed to make the output of the quality control process meaningful for the end-user. In other words, it is recommended to come up with a definition of what amount of biases is accepted to appear in the data what ones are rejected. This guideline should be updated in parallel with the enhancements achieved in the LiDAR quality assurance research field.

As mentioned earlier in this thesis, the quality control methods discussed could be used for absolute/external quality control; it is recommended to perform testing in this area in order to study the feasibility of this process. It is recommended to use Real Time Kinematic (RTK) GNSS techniques in the collection of surfaces for the ICPatch and ICPPoint methods. The current generation of RTK receivers contain interfaces that enable the automatic logging of data at intervals of a certain time or distance. For the line- and patch-based methods, it is recommended to use a reflectorless-capable Total Station to collect planar patch data (building roofs).

References

ASPRS LiDAR Committee (PAD) ASPRS Guidelines, Vertical Accuracy Reporting for Lidar Data [Online] = ASPRS Guidelines - Vertical Accuracy Reporting for LIDAR Data and LAS Specifications. Ed. Flood, M.. - May 2004. - August 2006. -

<http://www.asprs.org/society/divisions/ppd/standards/Lidar%20guidelines.pdf>.

Bretar F, Pierrot-Deseilligny Marc and Roux Michel Solving the Strip Adjustment Problem of 3D Airborne Lidar Data [Conference] // Geoscience and Remote Sensing Symposium. IGARSS '04. IEEE International. - 2004. - Vol. 7. - pp. 4734-4737.

Cheng Rita Department of Geomatics Engineering website [Online] = Registration for the In-Vivo Studies of Osteoarthritis based on Magnetic Resonance Imaging // Department of Geomatics Engineering. - April 2006. - September 19, 2007. -

<http://www.geomatics.ucalgary.ca/Papers/Thesis/AH/06.20242.RitaCheng.pdf>.

El-Sheimy N, Valeo C and Habib Ayman Digital Terrain Modelling: Acquisition, Manipulation and Applications [Book]. - Norwood, Massachusetts : Artech House, 2005.

Faruque Fazlay S. LIDAR Image Processing Creates Useful Imagery [Article] // ArcUser Magazine. - January-March 2003.

Ghanma Mwafag Department of Geomatics Engineering website [Online] = Integration of Photogrammetry and LiDAR // <http://www.geomatics.ucalgary.ca>. - University Of Calgary, April 2006. - July 2007. -

<http://www.geomatics.ucalgary.ca/Papers/Thesis/AH/06.20241.MwafagGhanma.pdf>.

Habib A, Cheng R and Kim E Automatic Surface Matching for the Registration of LIDAR Data and MR Imagery [Journal]. - [s.l.] : ETRI (Electronics and telecommunication Research Institute) Jurnal, 2006. - 2 : Vol. 28.

Habib A, Lee Y and Morgan M Surface Matching and Change Detection Using a Modified Hough Transformation for Robust Parameter Estimation [Journal]. - [s.l.] : The Photogrammetric Record, October 2001. - 98 : Vol. 17. - pp. 303-315.

Habib Ayman ENGO 531 - Advanced Photogrammetric and Ranging Techniques [Online] // <http://dprg.geomatics.ucalgary.ca>. - 2007. - July 2007. - http://dprg.geomatics.ucalgary.ca/files/Courses/531/AKAM_531_PPT_CH4_1.pdf.

Habib Ayman F, Al-Durgham Mohannad Mansour and Quackenbush Paul Alternative Methodologies for the Quality Control of LIDAR Systems [Article] // CIG/ISPRS Joint Conference. - Toronto : [s.n.], May 22-25, 2007. - p. 12.

Habib Ayman, Al-Durgham Mohannad and Quackenbush Paul Alternative Methodologies for the Quality Control of LIDAR Systems [Conference] // ASPRS Annual Conference. - Tampa, Florida : [s.n.], 2007.

Habib, A; Morgan, M; Kim, E.M; Cheng, R Linear Features in Photogrammetric Activities [Conference] // Geo-Imagery Bridging Continents. - Istanbul, Turkey : XXth ISPRS Congress, PS ICWG II/IV: Automated Geo-Spatial Data Production and Updating, 2004. - Vol. 20. - p. 610.

Kim Changjae, Habib Ayman and Mrstikb Paul New Approach for Planar Patch Segmentation using Airborne Laser Data [Conference] // ASPRS Annual Conference. - Tampa, Florida : [s.n.], 2007.

Kornus W and Ruiz A Strip Adjustment of LiDAR Data [Conference] // ISPRS "3-D Reconstruction from Airborne Laser Scanner and InSAR data". - 2003.

Lee, Jae-Bin; Yu, Ki-Yun; Kim, Yong-Il; Habib, Ayman Segmentation and Extraction of Linear Features for Detecting Discrepancies Between LIDAR Data Strips

[Conference] // IEEE. - 2005. - pp. 4954-4957.

Leica Geosystems Leica Geosystems [Online]. - Leica. - September 19, 2007. -

http://www.topobird.com/images/ALS40_Brochure.pdf.

Maas Hans-Gerd Least-Squares Matching with Airborne Laserscanning Data in a TIN Structure [Conference]. - [s.l.] : International Archives of Photogrammetry and Remote Sensing, 2000.

Morin Kristian Walker Department of Geomatics Engineering Publications [Online] =

Calibration of Airborne Laser Scanners // Department of Geomatics Engineering. -

University of Calgary, November 2003. - September 2007. -

<http://www.geomatics.ucalgary.ca/research/publications/GradTheses.html>.

Optech Inc Optech Website [Online]. - September 19, 2007. -

<http://www.optech.ca/prodaltm.htm>.

Pfeifer Norbert, Sander Elberink Oude and Filin Sagi Automatic Tie Elements

Detection for Laser Scanner Strip Adjustment [Conference]. - [s.l.] : International

Archives of Photogrammetry and Remote Sensing, 2005.

Rönholm Petri The Evaluation of the Internal Quality of Laser Scanning Strips Using

the Interactive Orientation Method and Point Clouds [Journal]. - [s.l.] : International

Archives of Photogrammetry and Remote Sensing, 2004. - Vol. 35.

Vosselman George and Mass Hans-Gerd Adjustment and Filtering Of Raw Laser

Altimetry Data [Conference] // OEEPE Airborne laser scanning and interferometric SAR

for detailed digital elevation model. - Stockholm, Sweden : [s.n.], 2001.

Zhang Zhengyou Iterative point matching for registration of free-form curves and surfaces [Journal]. - [s.l.] : Int. J. Computer Vision, 1994. - Vol. 13.

APPENDIX A: PARTIAL DERIVATIVES OF THE 3D CONFORMAL

EQUATION

The following are the partial derivatives of the unknowns with respect to the parameters for the 3D conformal equation shown below.

$$X_{3 \times 1} = \begin{bmatrix} X_T \\ Y_T \\ Z_T \end{bmatrix} + S \times R_{\Omega_t, \Phi_t, K_t} \times X_{1 \times 1}$$

The partial derivatives:

$$\frac{\partial X}{\partial X_T} = 1.0$$

$$\frac{\partial X}{\partial Y_T} = 0.0$$

$$\frac{\partial X}{\partial Z_T} = 0.0$$

$$\frac{\partial X}{\partial S} = R_{1,1} \times XYZ_{1i,1} + R_{1,2} \times XYZ_{1i,2} + R_{1,3} \times XYZ_{1i,3}$$

$$\frac{\partial X}{\partial \Omega} = 0.0$$

$$\frac{\partial X}{\partial \Phi} = -S \times \left[\sin \Omega \times \left[R_{2,1} \times XYZ_{1i,1} + R_{2,2} \times XYZ_{1i,2} + R_{2,3} \times XYZ_{1i,3} \right] \right.$$

$$\left. - \cos \Omega \times \left[R_{3,1} \times XYZ_{1i,1} + R_{3,2} \times XYZ_{1i,2} + R_{3,3} \times XYZ_{1i,3} \right] \right]$$

$$\frac{\partial X}{\partial K} = S \times \left[R_{1,2} \times XYZ_{1i,1} - R_{1,1} \times XYZ_{1i,2} \right]$$

$$\frac{\partial Y}{\partial X_T} = 0.0$$

$$\frac{\partial Y}{\partial Y_T} = 1.0$$

$$\frac{\partial Y}{\partial Z_T} = 0.0$$

$$\frac{\partial Y}{\partial S} = R_{2,1} \times XYZ_{1i,1} + R_{2,2} \times XYZ_{1i,2} + R_{2,3} \times XYZ_{1i,3}$$

$$\frac{\partial Y}{\partial \Omega} = -S \times [R_{3,1} \times XYZ_{1i,1} + R_{3,2} \times XYZ_{1i,2} + R_{3,3} \times XYZ_{1i,3}]$$

$$\frac{\partial Y}{\partial \Phi} = S \times \sin \Omega \times [R_{1,1} \times XYZ_{1i,1} + R_{1,2} \times XYZ_{1i,2} + R_{1,3} \times XYZ_{1i,3}]$$

$$\frac{\partial Y}{\partial K} = S \times [R_{2,2} \times XYZ_{1i,1} - R_{2,1} \times XYZ_{1i,2}]$$

$$\frac{\partial Z}{\partial X_T} = 0.0$$

$$\frac{\partial Z}{\partial Y_T} = 0.0$$

$$\frac{\partial Z}{\partial Z_T} = 1.0$$

$$\frac{\partial Z}{\partial S} = R_{3,1} \times XYZ_{1i,1} + R_{3,2} \times XYZ_{1i,2} + R_{3,3} \times XYZ_{1i,3}$$

$$\frac{\partial Z}{\partial \Omega} = S \times [R_{2,1} \times XYZ_{1i,1} + R_{2,2} \times XYZ_{1i,2} + R_{2,3} \times XYZ_{1i,3}]$$

$$\frac{\partial Z}{\partial \Phi} = -S \times \cos \Omega \times [R_{1,1} \times XYZ_{1i,1} + R_{1,2} \times XYZ_{1i,2} + R_{1,3} \times XYZ_{1i,3}]$$

$$\frac{\partial Z}{\partial K} = S \times [R_{3,2} \times XYZ_{1i,1} - R_{3,1} \times XYZ_{1i,2}]$$

APPENDIX B: DATA FOR INTENSITY AND RANGE IMAGE METHOD

B.1. A Sample of The Measured Points

A few samples of the points used for the intensity and range image method are shown below, with tables indicating the extracted points coordinates and the differences between these coordinates between strips.

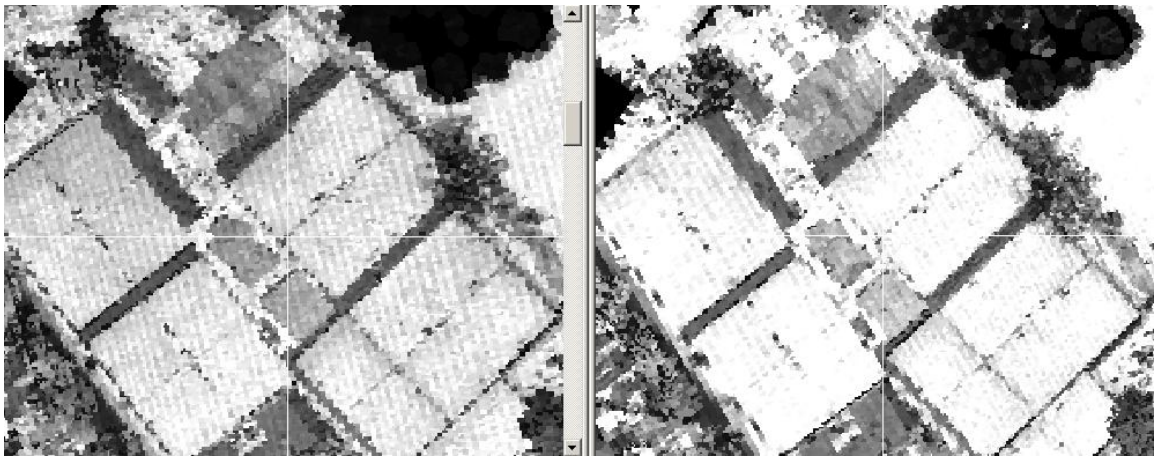


Figure 6.2: Measuring point number 9

	Strip 3			Strip 4			Difference		
	X	Y	Z	X	Y	Z	DX	DY	DZ
9	22676315.79	7188693.49	911.98	22676316.76	7188693.49	910.06	-0.97	0.00	1.92

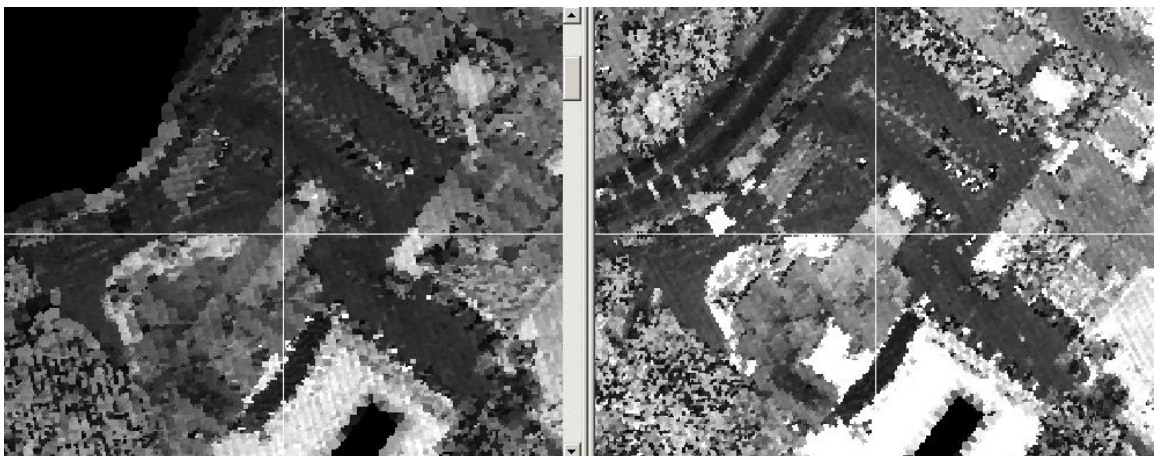


Figure 6.3: Measuring point number 18

	Strip 3			Strip 4			Difference		
	X	Y	Z	X	Y	Z	DX	DY	DZ
18	22676235.97	7188812.57	926.93	22676236.75	7188812.36	926.88	-0.79	0.22	0.05

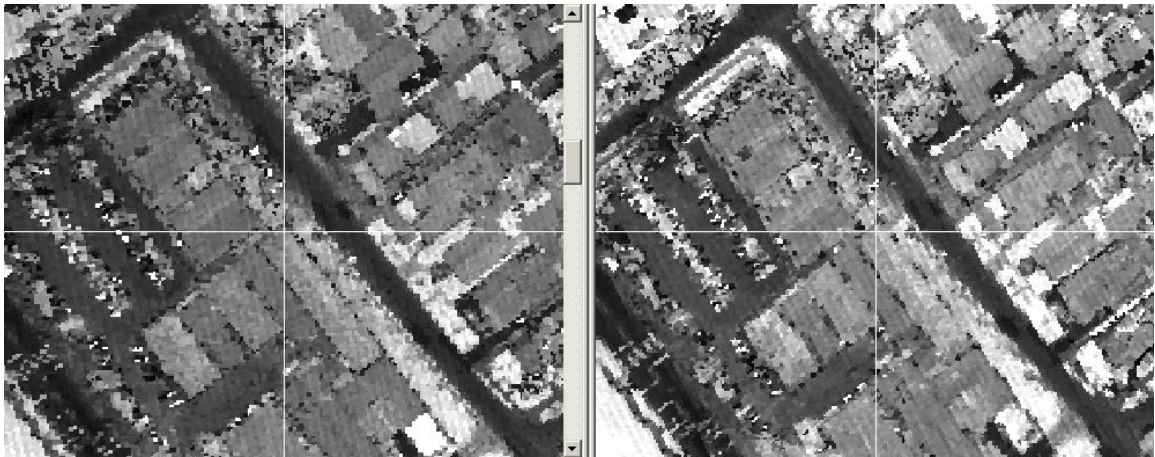


Figure 6.4: Measuring point number 27

	Strip 3			Strip 4			Difference		
	X	Y	Z	X	Y	Z	DX	DY	DZ
27	22676154.85	7188600.29	916.61	22676154.46	7188599.38	916.76	0.39	0.90	-0.15

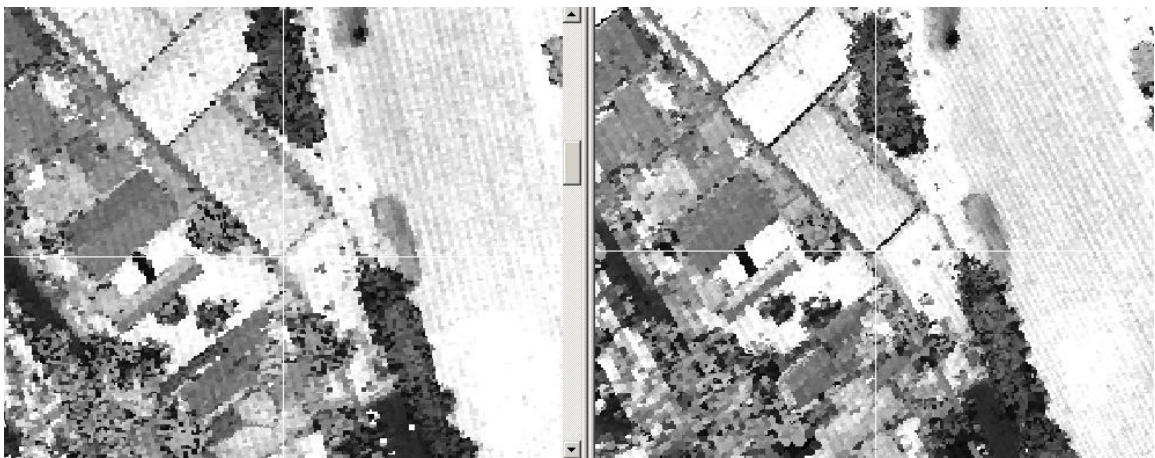


Figure 6.5: Measuring point number 79

	Strip 3			Strip 4			Difference		
	X	Y	Z	X	Y	Z	DX	DY	DZ
79	22676381.56	7188594.41	912.78	22676381.48	7188594.60	914.13	0.08	-0.20	-1.35

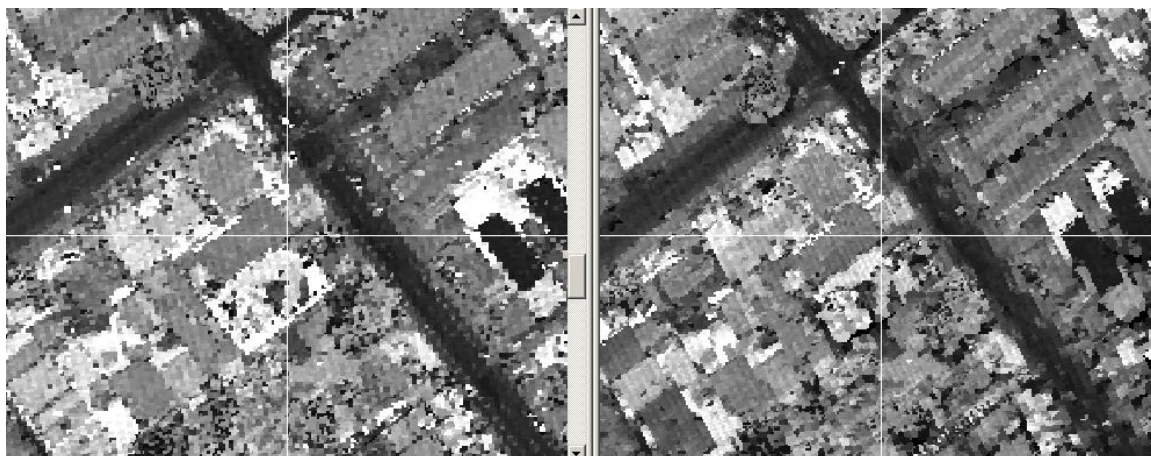


Figure 6.6: Measuring point number 87

	Strip 3			Strip 4			Difference		
	X	Y	Z	X	Y	Z	DX	DY	DZ
87	22675767.42	7188329.09	925.15	22675769.07	7188330.20	924.52	-1.65	-1.11	0.63

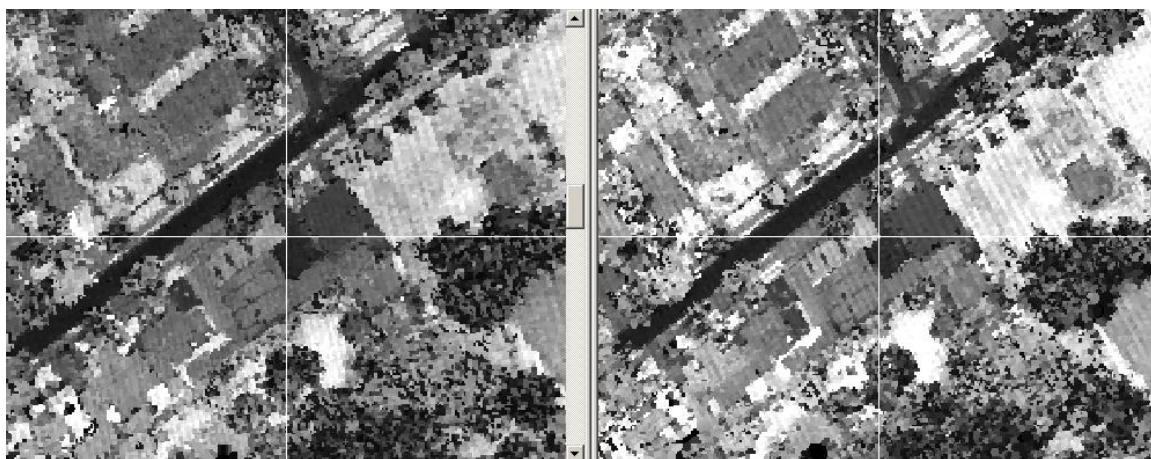


Figure 6.7: Measuring point number 93

	Strip 3			Strip 4			Difference		
	X	Y	Z	X	Y	Z	DX	DY	DZ
93	22675954.58	7188503.34	917.65	22675955.36	7188503.26	917.68	-0.78	0.08	-0.03

B.2. Points Used for the Range and Intensity Image Method (manually collected)

In this subsection, the table below shows all the extracted points and the squared differences in their coordinates between strips. The red color flags points with huge biases caused by the interpolation effect occurring at the break lines.

	Strip 3			Strip 4			Delta Squared		
	X	Y	Z	X	Y	Z	DX2	DY2	DZ2
1	22675553.35	7188404.80	927.46	22675554.14	7188403.17	927.55	0.63	2.63	0.01
2	22675590.92	7188365.13	926.02	22675591.37	7188364.70	926.13	0.20	0.19	0.01
3	22675668.15	7188353.92	928.80	22675669.85	7188353.27	928.96	2.89	0.42	0.03
4	22675813.99	7188331.05	946.00	22675815.77	7188330.79	946.07	3.17	0.07	0.00
5	22676064.24	7188460.49	910.91	22676064.55	7188459.56	911.00	0.09	0.86	0.01
6	22676194.98	7188677.95	909.53	22676195.23	7188676.34	909.51	0.06	2.59	0.00
7	22676240.71	7188702.98	909.85	22676240.56	7188701.87	909.86	0.02	1.23	0.00
8	22676277.82	7188682.27	909.81	22676277.52	7188681.30	909.92	0.09	0.94	0.01
9	22676315.79	7188693.49	911.98	22676316.76	7188693.49	910.06	0.94	0.00	3.69
10	22676342.11	7188661.56	912.32	22676343.05	7188661.10	912.39	0.88	0.20	0.00
11	22676367.57	7188658.54	912.42	22676367.81	7188658.82	912.53	0.06	0.08	0.01
12	22676292.49	7188663.28	909.77	22676292.38	7188662.25	909.72	0.01	1.07	0.00
13	22676325.28	7188737.50	913.91	22676325.90	7188737.68	914.34	0.39	0.03	0.18
14	22676315.36	7188736.63	920.58	22676315.24	7188736.54	920.97	0.01	0.01	0.15
15	22676380.51	7188674.07	912.32	22676381.15	7188672.91	912.45	0.41	1.33	0.02
16	22676319.67	7188733.18	916.83	22676319.05	7188732.73	917.35	0.39	0.20	0.27
17	22676352.90	7188622.29	912.37	22676353.34	7188622.24	912.44	0.19	0.00	0.00
18	22676235.97	7188812.57	926.93	22676236.75	7188812.36	926.88	0.62	0.05	0.00
19	22676295.51	7188813.00	925.15	22676295.43	7188813.50	924.50	0.01	0.24	0.42
20	22676210.51	7188820.34	916.51	22676211.23	7188819.59	916.51	0.52	0.55	0.00
21	22676483.63	7188893.26	923.72	22676484.01	7188892.36	923.55	0.14	0.80	0.03
22	22676553.10	7188924.32	928.93	22676552.97	7188923.98	928.83	0.02	0.12	0.01
23	22676055.61	7188652.93	917.11	22676056.55	7188651.96	917.01	0.88	0.93	0.01
24	22676149.24	7188768.99	934.65	22676149.89	7188768.54	934.43	0.42	0.20	0.05
25	22676174.27	7188644.73	913.77	22676175.03	7188644.34	913.88	0.59	0.15	0.01
26	22676132.41	7188608.05	923.20	22676132.75	7188608.15	923.15	0.11	0.01	0.00
27	22676154.85	7188600.29	916.61	22676154.46	7188599.38	916.76	0.15	0.81	0.02
28	22675952.49	7188499.32	913.68	22675952.16	7188499.19	913.70	0.11	0.02	0.00
29	22675930.92	7188395.77	921.03	22675930.82	7188395.18	921.51	0.01	0.35	0.23
30	22675969.32	7188391.89	921.33	22675970.45	7188391.37	921.23	1.27	0.27	0.01
31	22676073.30	7188424.25	922.84	22676073.31	7188424.51	922.67	0.00	0.07	0.03
32	22675912.79	7188437.19	919.84	22675912.16	7188437.47	920.40	0.41	0.08	0.31
33	22675966.30	7188418.21	917.66	22675966.26	7188418.42	917.89	0.00	0.04	0.05
34	22675970.18	7188404.40	921.09	22675971.21	7188403.94	921.33	1.06	0.21	0.06
35	22675976.65	7188397.49	924.39	22675976.54	7188397.84	924.33	0.01	0.12	0.00
36	22675932.64	7188431.15	935.77	22675932.35	7188430.23	935.85	0.09	0.85	0.01
37	22675925.31	7188467.39	917.30	22675925.11	7188467.56	917.88	0.04	0.03	0.34
38	22675951.63	7188428.13	914.61	22675951.78	7188428.70	914.67	0.02	0.33	0.00
39	22675980.97	7188409.14	914.72	22675981.11	7188408.89	914.86	0.02	0.06	0.02

40	22675974.06	7188401.38	922.33	22675974.64	7188400.89	922.43	0.33	0.24	0.01
41	22675913.23	7188400.95	917.20	22675913.30	7188401.65	917.29	0.01	0.50	0.01
42	22675861.45	7188417.77	920.75	22675861.87	7188417.27	920.88	0.17	0.25	0.02
43	22675824.34	7188451.86	920.46	22675824.53	7188451.56	920.10	0.03	0.09	0.13
44	22675806.22	7188435.03	920.79	22675807.00	7188434.80	920.94	0.61	0.05	0.02
45	22675722.51	7188454.88	928.44	22675723.19	7188454.23	928.23	0.45	0.42	0.04
46	22675612.49	7188399.22	929.52	22675611.94	7188400.13	928.94	0.30	0.83	0.34
47	22675675.48	7188378.51	924.86	22675675.18	7188378.41	924.70	0.09	0.01	0.03
48	22675669.44	7188352.19	922.86	22675669.09	7188352.13	923.49	0.13	0.00	0.40
49	22675630.18	7188384.98	923.72	22675630.99	7188384.89	923.81	0.66	0.01	0.01
50	22675769.11	7188330.18	926.40	22675768.52	7188330.03	926.60	0.35	0.02	0.04
51	22675744.52	7188345.29	925.30	22675744.90	7188345.65	925.31	0.15	0.13	0.00
52	22675737.62	7188296.96	927.17	22675737.66	7188296.50	927.42	0.00	0.21	0.06
53	22675582.72	7188261.58	939.31	22675582.22	7188261.07	938.81	0.24	0.26	0.25
54	22675555.10	7188403.54	927.24	22675555.17	7188402.80	927.34	0.00	0.55	0.01
55	22675566.75	7188430.29	926.43	22675566.98	7188429.85	926.83	0.05	0.19	0.16
56	22675543.88	7188384.98	928.15	22675544.89	7188384.51	928.32	1.00	0.22	0.03
57	22675592.21	7188365.57	929.79	22675592.13	7188364.70	929.81	0.01	0.75	0.00
58	22675625.86	7188361.68	939.08	22675626.80	7188359.75	939.12	0.87	3.75	0.00
59	22675687.57	7188334.50	922.72	22675687.76	7188334.60	922.85	0.04	0.01	0.02
60	22675704.39	7188261.15	930.49	22675704.14	7188261.07	930.67	0.06	0.01	0.03
61	22675647.44	7188252.95	928.15	22675647.75	7188252.69	928.32	0.10	0.07	0.03
62	22675639.67	7188243.46	940.27	22675639.37	7188244.69	940.40	0.09	1.51	0.02
63	22675669.44	7188278.84	926.76	22675669.47	7188278.60	926.89	0.00	0.06	0.02
64	22675542.37	7188445.38	935.73	22675542.39	7188444.83	935.62	0.00	0.30	0.01
65	22675507.57	7188473.10	935.86	22675507.70	7188472.59	936.03	0.02	0.27	0.03
66	22675499.31	7188460.72	935.82	22675499.02	7188461.02	935.84	0.08	0.09	0.00
67	22675554.76	7188454.82	935.78	22675555.12	7188454.66	936.08	0.13	0.02	0.09
68	22675518.78	7188485.49	936.05	22675518.68	7188484.73	936.33	0.01	0.58	0.08
69	22675495.77	7188519.70	937.49	22675494.98	7188520.01	937.73	0.64	0.09	0.06
70	22675576.00	7188529.73	937.99	22675576.51	7188529.26	938.06	0.27	0.22	0.00
71	22675607.85	7188479.00	930.15	22675608.32	7188478.95	930.18	0.22	0.00	0.00
72	22675655.63	7188424.73	926.90	22675655.16	7188424.59	927.85	0.22	0.02	0.90
73	22675660.94	7188553.33	928.40	22675660.36	7188553.55	928.22	0.33	0.05	0.03
74	22676175.25	7188636.16	913.06	22676175.61	7188635.66	913.25	0.13	0.25	0.04
75	22676217.01	7188684.66	928.60	22676217.25	7188684.24	929.20	0.06	0.18	0.36
76	22676135.96	7188585.20	918.19	22676136.29	7188585.93	918.11	0.11	0.54	0.01
77	22676280.86	7188576.60	912.04	22676280.86	7188576.10	912.58	0.00	0.25	0.29
78	22676345.95	7188594.41	913.58	22676346.78	7188594.03	913.04	0.70	0.15	0.29
79	22676381.56	7188594.41	912.78	22676381.48	7188594.60	914.13	0.01	0.04	1.82
80	22676409.19	7188607.30	912.86	22676409.24	7188607.90	912.98	0.00	0.36	0.01
81	22676207.18	7188823.43	916.37	22676206.84	7188823.60	916.45	0.12	0.03	0.01
82	22676315.25	7188737.47	920.77	22676314.98	7188736.86	921.09	0.07	0.37	0.10

83	22676345.95	7188755.89	910.43	22676345.63	7188754.79	910.40	0.10	1.21	0.00	
84	22676296.83	7188805.62	922.70	22676297.63	7188805.10	922.93	0.64	0.27	0.05	
85	22676476.73	7188729.49	918.53	22676476.90	7188729.92	918.63	0.03	0.19	0.01	
86	22676609.97	7188739.92	920.88	22676609.90	7188739.75	921.00	0.00	0.03	0.01	
87	22675767.42	7188329.09	925.15	22675769.07	7188330.20	924.52	2.71	1.22	0.40	
88	22675791.83	7188403.13	918.13	22675792.20	7188404.16	918.10	0.14	1.06	0.00	
89	22675872.03	7188456.67	915.74	22675872.67	7188456.83	915.60	0.40	0.03	0.02	
90	22675951.12	7188499.89	913.77	22675951.82	7188499.28	913.70	0.49	0.36	0.00	
91	22675956.31	7188494.27	913.69	22675957.13	7188493.54	913.83	0.68	0.54	0.02	
92	22675946.37	7188498.59	917.53	22675946.96	7188497.96	917.45	0.35	0.40	0.01	
93	22675954.58	7188503.34	917.65	22675955.36	7188503.26	917.68	0.61	0.01	0.00	
94	22675794.24	7188481.30	918.38	22675794.39	7188481.15	918.31	0.02	0.02	0.00	
95	22675805.91	7188434.63	920.87	22675806.33	7188434.28	920.95	0.18	0.12	0.01	
96	22675798.99	7188428.58	920.86	22675798.82	7188428.53	920.91	0.03	0.00	0.00	
97	22675921.73	7188464.88	915.39	22675922.19	7188464.35	915.52	0.21	0.28	0.02	
98	22675920.00	7188433.33	936.06	22675920.87	7188433.84	936.17	0.75	0.26	0.01	
99	22675930.81	7188396.59	920.55	22675930.60	7188396.25	920.71	0.05	0.12	0.03	
100	22675889.32	7188390.11	922.29	22675889.03	7188390.50	922.20	0.08	0.15	0.01	
							Avg	0.33	0.38	0.12
							STD	0.54	0.59	0.42